NUMERICAL SIMULATION OF ROTATING STALL AND SURGE ALLEVIATION IN AXIAL COMPRESSORS

A Thesis
Presented to
The Academic Faculty

by

Saeid Niazi

In Partial Fulfillment
of the Requirements for the Degree
Doctor of Philosophy in Aerospace Engineering

Georgia Institute of Technology

July 2000

NUMERICAL SIMULATION OF ROTATING STALL AND SURGE ALLEVIATION IN AXIAL COMPRESSORS

Approved:

_____
Lakshmi N. Sankar, Chairman

_____
J.V.R. Prasad

_____
Suresh Menon

_____
Stephen M. Ruffin

_____
Prasanna V. Kadaba

Date Approved _____

IN THE NAME OF GOD

Dedicated to my parents

Behjat Golbahar Haghighi and Sadrollah Niazi

for their most precious gift of selfless love

ACKNOWLEDGEMENTS

Many people have touched my life not only from an academic point of view, but both their friendship and spiritual support have been a source of encouragement and strength to complete this work.

I would like to thank Dr. Lakshmi N. Sankar, my teacher and dissertation advisor, for his support throughout the research period. His patience and kindness with his detailed knowledge about this research topic played a key role in the development of this work. I am really honored and grateful to have had the opportunity to work under him.

I would also like to thank Dr. J. V. R. Prasad for his helpful suggestions and technical expertise in the area of flow control. Many thanks to Dr. S. Menon, Dr. S. M. Ruffin, and Dr. P. V. Kadaba for their services as members of my reading committee and their valuable comments.

The financial assistance given by Army Research Office under the Multidisciplinary University Research Initiative (MURI) on Intelligent Turbine Engine is gratefully acknowledged.

Thanks to my co-worker and my friend Alex Stein for his great efforts during code development and his steadfast support throughout the research.

I would also like to thank the past and present members of CFD lab for their warm friendship and support during my administrative responsibility in the lab. To: Justin Russell, Mert Berkman, Ebru Usta, Mehmet Sahin, Guanpeng Xu, Zhong Yang, Yi Liu,

Zhijian Liu, Masayoshi Senga, and Gang Wang. Thanks also to my friend and roommate Konstantin Ignatiev in the School of Materials and Science Engineering for providing me assistance with computer services. I would like to thank Catherine Moseley Matos for taking the time to read this dissertation and for her helpful suggestions. Thanks also to all my friends whose advice and support made this achievement possible.

I would like to thank Dr. J. Jagoda, the graduate coordinator, and the staff of the Aerospace Engineering Office: Revonda B. Mullis, Loretta Carroll, Terry M. Parrott, Margaret A. Ojala, Carole W. Gaines, and Howard L. Simpson for being always ready to help me.

I would like to thank all my sisters and brothers and their families for their great support during my study. A special note of thanks to my brother and friend, Hamid and his family, Hilda and sweet Sara, for their generous support during the pursuit of my degree in Atlanta.

Finally, I owe my greatest gratitude to my parents, Behjat Golbahar Haghighi and Sadrollah Niazi, to whom this work is dedicated. Their constant encouragement and great unconditional love for myself and each of my sisters and brothers have been a source of inspiration in my life.

TABLE OF CONTENTS

LIST OF TABLES

LIST OF FIGURES

NOMENCLATURE

A	Jacobian matrix
A_b	bleed area
A_t	throttle area
a	speed of sound
C_V	specific heat at constant volume
c_{b1}, c_{b2}	constants in Spalart-Allmaras turbulence model
c_{t1}, c_{t2}, c_{t3}, c_{t4}	constants in Spalart-Allmaras turbulence model
c_{v1}	constants in Spalart-Allmaras turbulence model
c_{w1}, c_{w2}, c_{w3}	constants in Spalart-Allmaras turbulence model
d	distance to closest wall, used in Spalart-Allmaras turbulence model
E, F, G	inviscid flux vectors
e	internal energy per unit volume
f_{t1}, f_{t2}	functions in Spalart-Allmaras turbulence model
f_{v1}, f_{v2}, f_w	functions in Spalart-Allmaras turbulence model
g, g_t	functions in Spalart-Allmaras turbulence model
I	identity matrix
K_b	bleed valve constant
K_t	throttle valve constant
L_{ref}	characteristic length of the compressor, usually the rotor diameter

$\dot{m}_c$	mass flow rate through the compressor
$\dot{m}_t$	throttle mass flow rate
$\dot{m}_b$	bleed mass flow rate
p	pressure
q	conserved flow variables
R, S, T	viscous stresses and heat fluxes at a cell face
S	vorticity magnitude in Spalart-Allmaras turbulence model
$\tilde{S}$	modified vorticity magnitude
T	temperature
T	also refers to matrix containing eigenvectors of the Jacobian matrix
t	time
U	relative velocity normal to a cell face
u, v, w	Cartesian velocity components
V_p	plenum volume
x, y, z	Cartesian coordinates
Δq	change in conserved flow variables from one time step to next
ΔU	trip point velocity in Spalart-Allmaras turbulence model
Δt	time step
γ	specific heat ratio

κ	von Karman constant
Λ	matrix containing eigenvalues of the Jacobian matrix
μ	molecular viscosity
ν	eddy viscosity
ν_t	turbulent viscosity
$\tilde{n}$	working variable in Spalart-Allmaras turbulence model
ρ	density
σ	constant in Spalart-Allmaras model
τ_{ij}	viscous stress tensor
ω_t	trip point wall vorticity

Subscripts

0	stagnation quantity
b	bleed
p	plenum
t	turbulence quantity
x, y, z, t	Cartesian and time derivatives
∞	free stream quantity, upstream of the inlet

Superscripts

n, n+1	two adjacent time level

Overbars

~	used to indicate Roe averages
$\rightarrow$	used to indicate vectors
—	time or spatial averages

SUMMARY

Axial compression systems are widely used in many aerodynamic applications. However, the operability of such systems is limited at low-mass flow rates by fluid dynamic instabilities. These instabilities lead the compressor to rotating stall or surge. In some instances, a combination of rotating stall and surge, called modified surge, has also been observed. Experimental and computational methods are two approaches for investigating these adverse aerodynamic phenomena. In this study, numerical investigations have been performed to study these phenomena, and to develop control strategies for alleviation of rotating stall and surge.

A three-dimensional unsteady Navier-Stokes analysis capable of modeling multistage turbomachinery components has been developed. This method uses a finite volume approach that is third order accurate in space, and first or second order in time. The scheme is implicit in time, permitting the use of large time steps. A one-equation Spalart-Allmaras model is used to model the effects of turbulence. The analysis is cast in a very general form so that a variety of configurations -centrifugal compressors and multistage compressors- may be analyzed with minor modifications to the analysis.

Calculations have been done both at design and off-design conditions for an axial compressor tested at NASA Glenn Research Center. At off-design conditions the calculations show that the tip leakage flow becomes strong, and its interaction with the tip shock leads to compressor rotating stall and modified surge. Both global variations to

the mass flow rate, associated with surge, and azimuthal variations in flow conditions indicative of rotating stall, were observed.

It is demonstrated that these adverse phenomena may be eliminated, and stable operation restored, by the use of bleed valves located on the diffuser walls. Two types of controls were examined: open-loop and closed-loop. In the open-loop case mass is removed at a fixed, preset rate from the diffuser. In the closed-loop case, the rate of bleed is linked to pressure fluctuations upstream of the compressor face. The bleed valve is activated when the amplitude of pressure fluctuations sensed by the probes exceeds a certain range. Calculations show that both types of bleeding eliminate both rotating stall and modified surge, and suppress the precursor disturbances upstream of the compressor face. It is observed that smaller amounts of compressed air need to be removed with the closed-loop control, as compared to open-loop control.

CHAPTER I

INTRODUCTION

> "*My invention consists in a compressor or pump of the turbine type operating by the motion of sets of movable blades or vanes between sets of fixed blades, the movable blades being more widely spaced than in my steam turbine, and constructed with curved surfaces on the delivery side, and set at a suitable angle to the axis of rotation. The fixed blades may have a similar configuration and be similarly arranged on the containing casing at any suitable angle. Parsons 1901,"* taken from Reference [1]"

In 1853 the basic fundamentals of the operations of a multistage axial compressor were first presented to the French Academie des Sciences[2-3]. Parsons built and patented an axial flow compressor in 1901[1]. Since that time, compressors have significantly evolved. There have been continuous improvements leading to increases in efficiency, the pressure ratio per stage, and a decrease in weight.

Compressors have a wide variety of applications. They are a primary component in turbojet engines used in aerospace propulsion, industrial gas turbines that generate power, and processors in chemical industry to pressurize gas or fluids. Compressors can vary in size from a few feet to tens of feet in diameter. In turbomachinery applications, safe and efficient operation of the compression system is imperative. To run a compressor as efficiently as possible, and to prevent damage, flow instabilities such as rotating stall and surge must be avoided, or dealt with soon after their inception.

Considerable interest exists in the jet propulsion community in understanding and controlling flow instabilities.

1.1 AN OVERVIEW OF COMPRESSOR OPERATIONS

The basic purpose of a compressor is to increase the total pressure of the working fluid using shaft work. Depending on their type, compressors increase the pressure in different ways. They can be divided into four general groups: rotary, reciprocating, centrifugal and axial. In rotary and reciprocating compressors, shaft work is used to reduce the volume of gas and increase the gas pressure. In axial and centrifugal compressors, also known as turbo-compressors, the fluid is first accelerated through moving blades. In the next step, the high kinetic energy of the fluid is converted into pressure by decelerating the gas in stator blade passages or in a diffuser.

In centrifugal compressors, the flow leaves the compressor in a direction perpendicular to the rotation axis. In axial compressors, flow enters and leaves the compressor in the axial direction. Because an axial compressor does not benefit from the increase in radius that occurs in a centrifugal compressor, the pressure rise obtained from a single axial stage is lower. However, compared to centrifugal compressors, axial compressors can handle a higher mass flow rate for the same frontal area. This is one of the reasons axial compressors have been used more in aircraft jet engines, where frontal area plays an important role. Another advantage of axial compressors is that multi-staging is much easier, and does not need the complex return channels required in multiple centrifugal stages. As Ferguson[4] points out, a turbo-compressor may also be

called as blower, fan, booster, turbo-charger or exhauster, and the distinctions between these are vague. Generally speaking, fans are the first stage of the compression system in jet engines, and are low- pressure compressors. Blowers may be thought of medium pressure compressors.

A variety of turbo-machines and their ranges of utilization in terms of basic non-dimensional parameters are shown in Figure 1.1, taken from Reference [5]. The horizontal axis represents the flow coefficient, which is a non-dimensional volume flow rate. The vertical axis shows the head coefficient, which is a dimensionless measure of the total enthalpy change through the stage, and roughly equals the work input per unit mass flow. The literature on compressors is vast. References [5]-[9] give a basic introduction to turbomachinery, and more advanced topics on compressors may be found in References [10]-[12].

The compressors considered in this study are from the family of axial compressors. An axial compressor, shown in Figure 1.2, consists of a row of rotor blades followed by a row of stator blades. The working fluid passes through these blades without significant change in radius. Energy is transferred to the fluid by changing its swirl, or tangential velocity, through the stage. A schematic diagram of the changes in velocity and fluid properties through an axial compressor stage is shown in Figure 1.2. It shows how pressure rises through the rotor and stator passages.

Early axial compressors had entirely subsonic flow. Since modern applications require compression systems with higher-pressure ratios and mass flow rates, designers

have permitted supersonic flow, particularly near the leading edge tip where the highest total velocity occurs. Today, most high performance compression stages are transonic, where regions of subsonic and supersonic flow both exist in the blade passages. A transonic compression system is now one of the main components of high-bypass ratio engines. Large fans with inlet relative Mach numbers of 1.4 to 1.6 have been recently used in engines of this kind. These systems have been achieved by advanced design, using sophisticated computational design tools and extensive experimentation.

The steady state performance of a compressor is usually described by a plot of the averaged mass flow rate versus the total pressure ratio. This plot is called the characteristic or performance map of the compressor. Figure 1.3 shows a typical compressor performance map for axial and centrifugal compressors. Axial compressors tend to have a steeper drop aft of the peak of the compressor performance map compared to centrifugal compressors.

1.2 COMPRESSOR STABILITY

Stability in a compressor is the ability of a compressor to recover from disturbances that alter the compressor operation about an operational equilibrium point. Disturbances may be considered as transient or deliberate changes to the operating point. In the case of transient disturbances, the system is stable if it returns to its original operating point. If the disturbances drive the compressor away from the original point, the system is unstable. The steady state match between a compressor and its drive turbine or jet nozzle, which is perturbed by a transient change of mass-flow, is a good example of this

case. When there are deliberate changes to the operating point, the performance is considered stable if a new operational equilibrium point can be achieved, e.g., shifting the operating point by changing the compressor shaft speed. If steady state operation at a new operating point is not possible, the system is unstable.

Stability in compressors may be studied from two different perspectives. The first is called operational stability, which deals with the matching of compressor performance with a downstream flow device such as a turbine or throttle. The second is aerodynamic stability, which deals with deteriorations in the operation due to flow separation, stall or surge.

The operational stability of a compression system depends on the characteristic of both the compressor and the downstream flow device. Mathematically, if the slope of compressor performance map is less than the slope of characteristic map of the throttle (points P_1 and P_2 shown in Figure 1.4a) the system is stable. Otherwise, as shown in Figure 1.4b for point P_3, the system is not stable. Compressors, by design, usually operate near point P_1 on the performance map shown in Figure 1.4. Operations at lower mass flow ratios (near point P_2) can trigger instabilities as discussed later.

The stable range of operation of axial and centrifugal compressors is limited at both very high and very low mass flow rates, as shown in Figure 1.5. If the mass flow rate is too high, shocks will form and the flow through the compressor will be choked (sonic condition). On the other hand, as the mass flow rate through the compressor decreases, flow instabilities will occur. These instabilities include rotating stall and surge. If they

are allowed to persist or grow, catastrophic damage to the compressor and the engine will occur. Surge, in particular, is to be avoided at all costs.

In looking at a map of the characteristic performance of a compressor, Figure 1.5, a dashed line known as the surge or stall line, can be seen. Rotating stall and surge usually occur at low flow rates, but may still occur on the right side of the surge line if the flow becomes unstable as a result of the instability. Therefore, a second line parallel to the surge line is usually introduced as a surge avoidance line. Another reason for introducing the surge avoidance line is that the compressor characteristic, and consequently the surge line, may be poorly known. Operating at the surge avoidance line provides a safety margin for the compressor operation and prevents the compressor from operating in a region where stall or surge may occur. The closer the operating point is to the surge line, the greater the pressure ratio achieved by the compressor, but the greater the risk of stall or surge.

1.3 OBJECTIVES AND ORGANIZATION OF THE PRESENT WORK

The main objectives of the current study are to understand the physics of compressor stall and surge, and to develop an appropriate control methodology for the prevention of these instabilities.

Although considerable progress in understanding and modeling of stall and surge in axial compressors has been achieved during the past two decades, none of the models are able to describe accurately the flow phenomena that occur in the compressor and give rise

to stall and surge. Detailed flow visualizations, both computational and experimental, are necessary for understanding the nature of these instabilities.

CFD modeling of axial compressors is a well-developed field. Most compression systems are now being designed using CFD tools. However, most numerical studies of air breathing compression systems are done in the stable part of compressor characteristic performance map, where the flow is "steady" in a rotating frame. The current research attempts to provide computational tools to study unsteady aerodynamic phenomena, such as rotating stall and surge, in axial compressors. Work has also been done in simulating stall and designing stall control methods that extend the stable operating range of the compressor.

This thesis is organized as follows: A review of surge and rotating stall phenomena, both from a historical and a technical perspective, is presented in Chapter II. Chapter III introduces the mathematical and numerical tools required for carrying out the numerical simulations. Validation results for an axial compressor at peak efficiency conditions are presented in Chapter IV. Simulations of the onset and growth of stall are given in Chapter V. Results for active bleed control techniques are presented in Chapter VI. Finally, the conclusions and recommendations for further improvements of compressor control technology are given in Chapter VII.

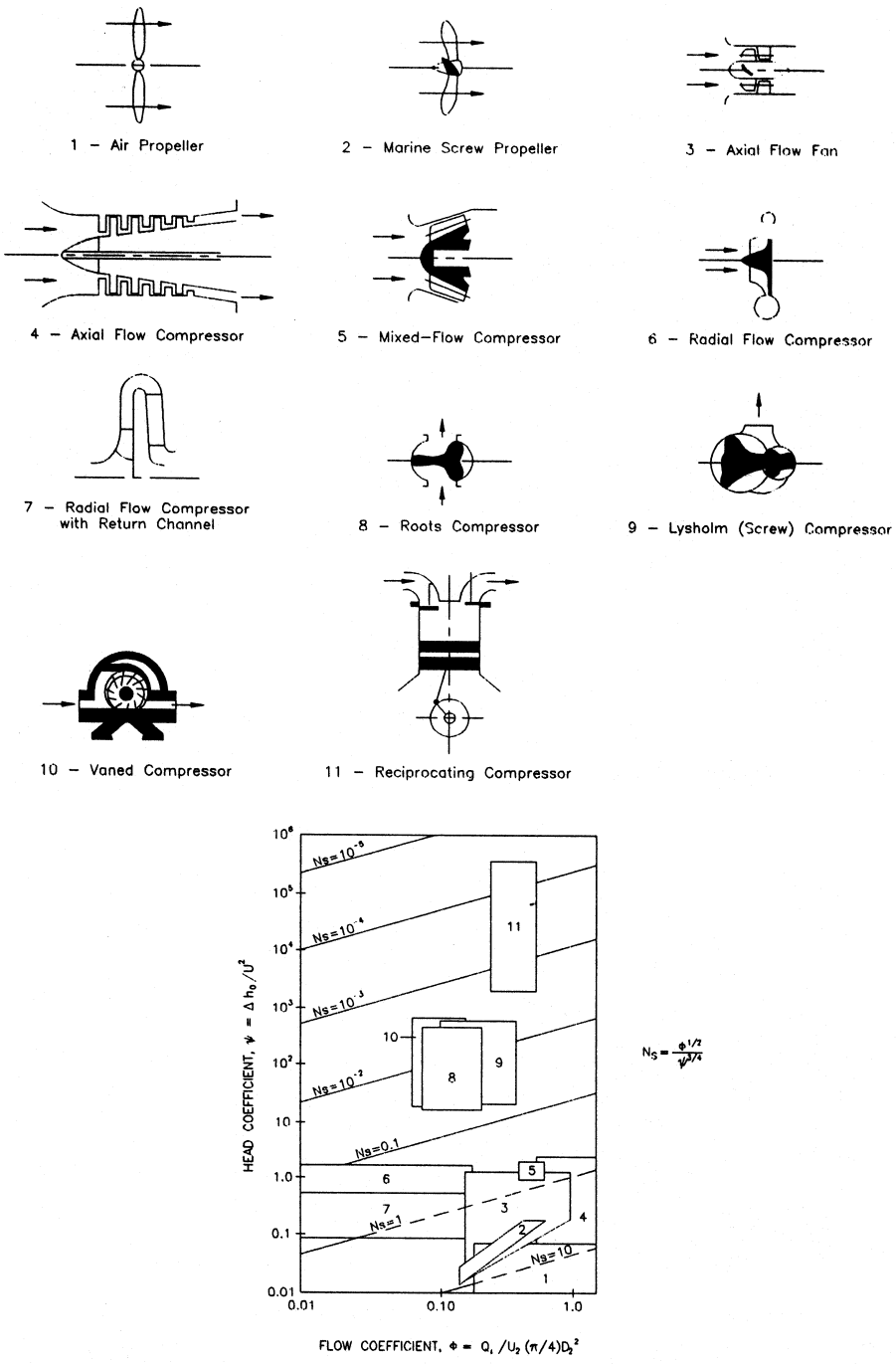

Figure 1.1 Work input machinery classification, Reference [5].

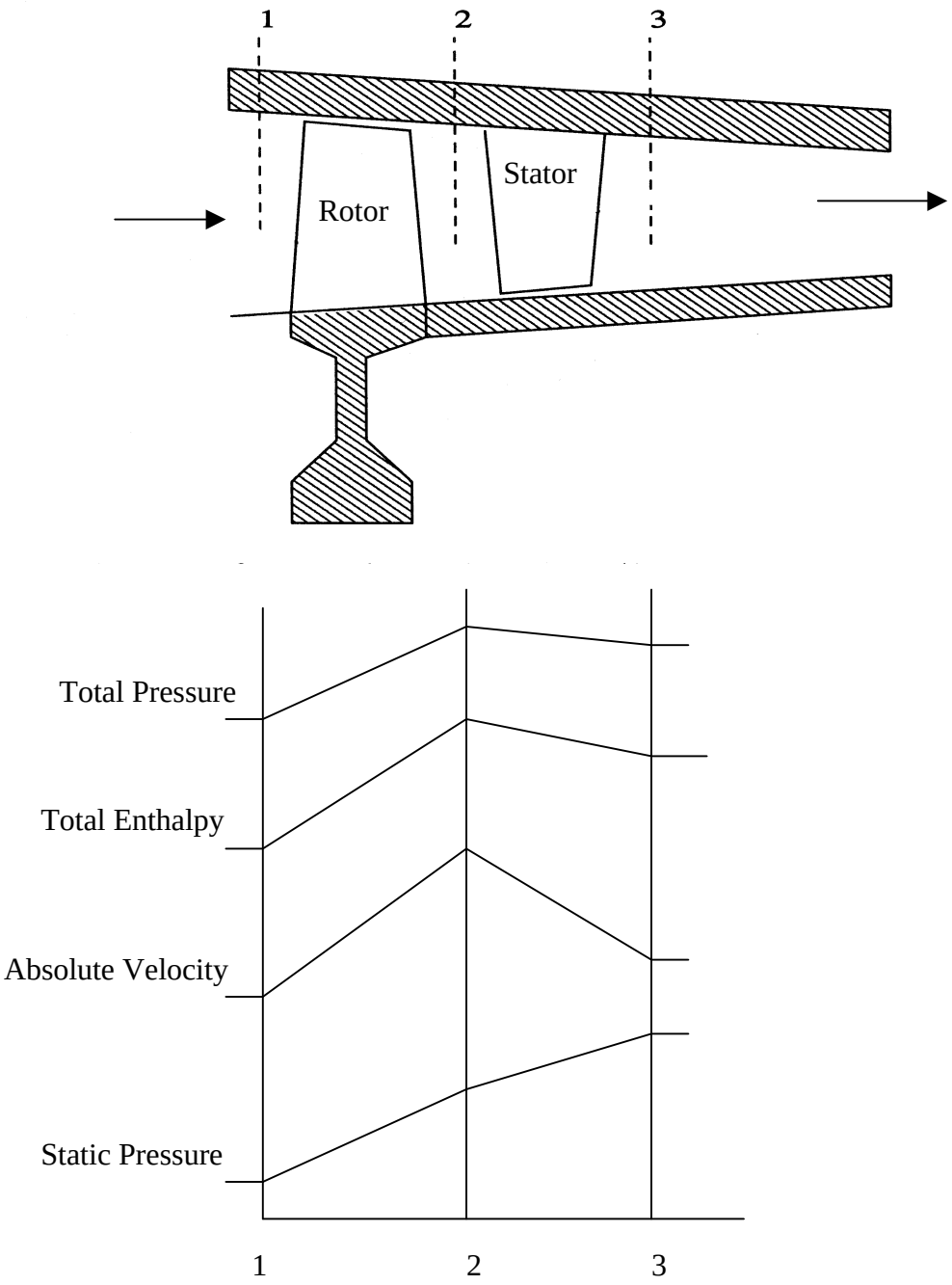

Figure 1.2 Schematic diagram of changes in fluid properties and velocity through an axial compressor stage, References [5], [11].

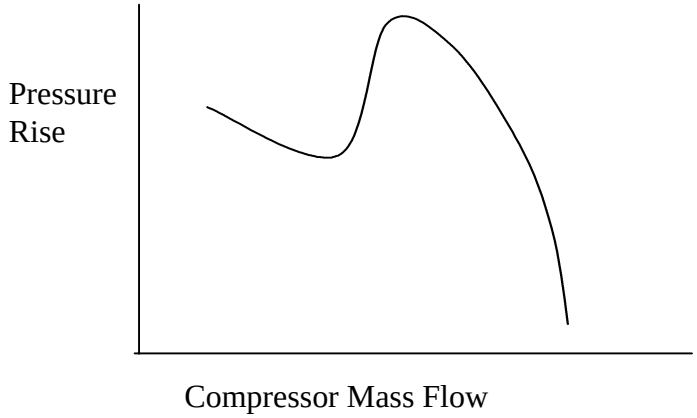

Figure 1.3 Typical compressor characteristic map for axial and centrifugal compressors.

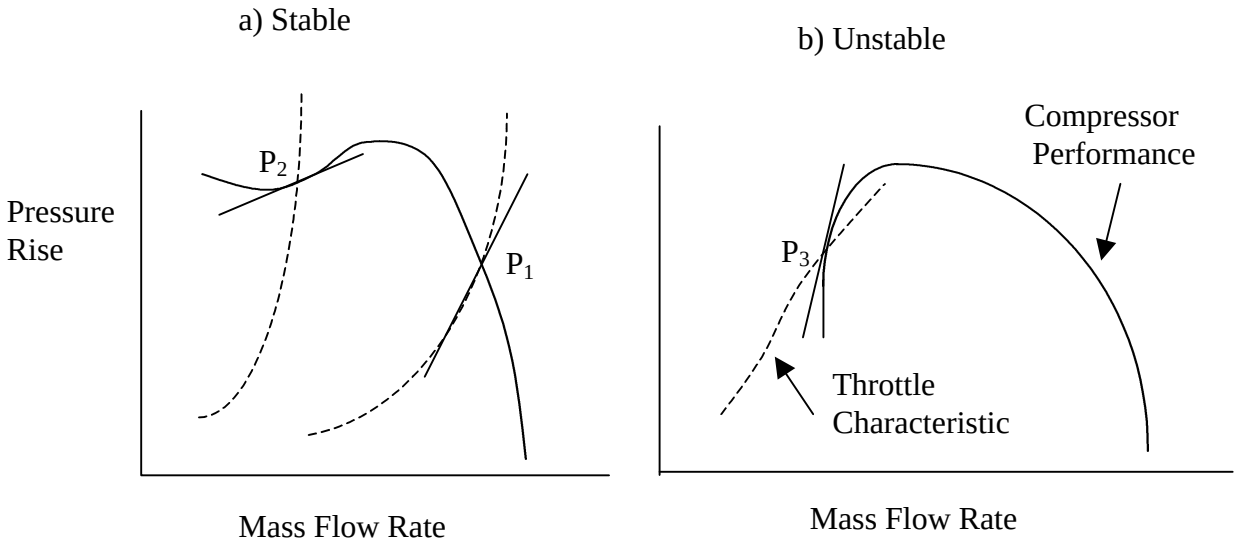

Figure 1.4 Operational stability, matching the compressor and throttle characteristics.

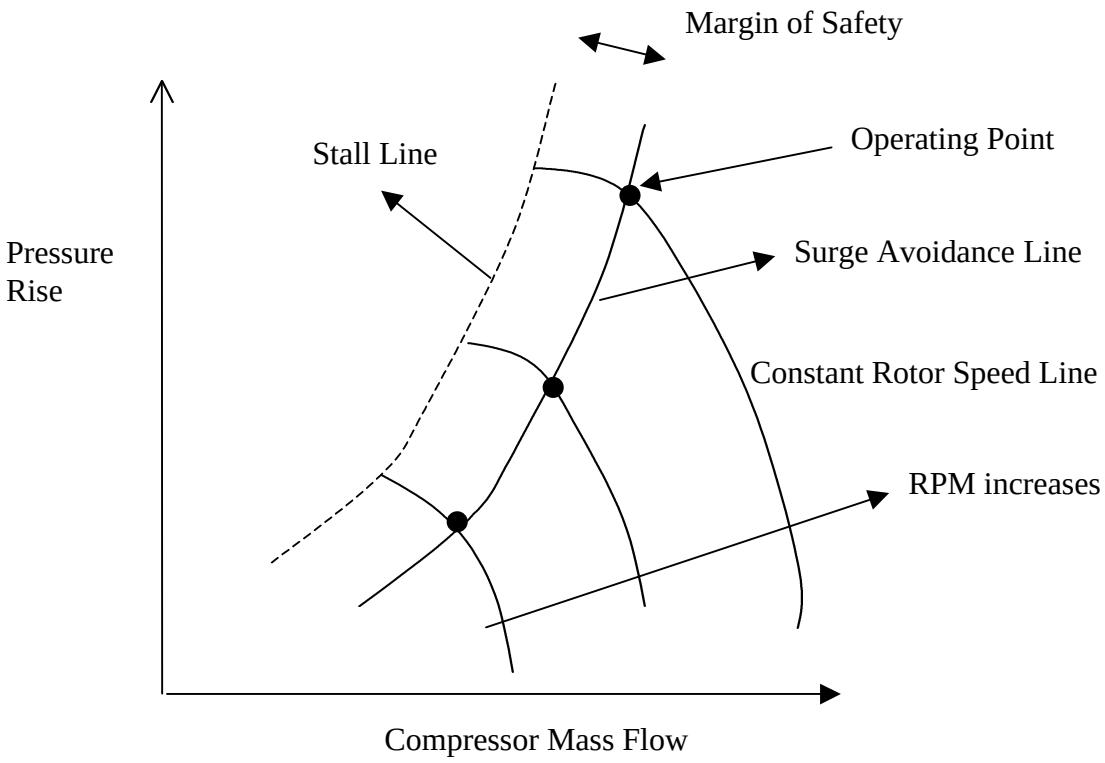

Figure 1.5 Effects of rotor RPM on compressor performance and stability.

CHAPTER II

AN OVERVIEW OF COMPRESSOR INSTABILITY PHENOMENA

In the pervious chapter, it was pointed out that the stable part of compressor performance map is limited due to aerodynamic instabilities. These instabilities manifest themselves as rotating stall or surge. This chapter is devoted to reviewing these unsteady phenomena from both a historical and a technical perspective. Section 2.1 describes the physical mechanisms behind rotating stall. A discussion of surge phenomenon is given in Section 2.2. In Section 2.3, the historical developments that led to the discovery of rotating stall and surge phenomena are presented. A brief review of methods currently employed in compressor control, and a review of prior computational study of compressors and compressor control are also given in Section 2.3.

2.1 FUNDAMENTALS OF ROTATING STALL

During the normal operation of a compressor, the airflow through the compressor is essentially steady and axisymmetric in a rotating coordinate system. If a flow instability is somehow introduced into the system (say, due to a change in the rotor speed, flow separation at the inlet, or other type of flow distortion), instabilities may develop and the compressor performance may deteriorate. The instability manifests itself as either a rotating stall or surge. Rotating stall is inherently a 2-D unsteady local

phenomenon in which the flow is no longer uniform in the azimuthal direction. It often takes only a few seconds for rotating stall to build up, and the compressor can operate under rotating stall for several minutes before damage develops. Rotating stall can occur in both compressible and incompressible flow.

The inception of rotating stall is shown in Figure 2.1. This figure illustrates the blade row viewed from the top of the annulus. Stall is present on some of the blades. It is not known for certain why all blades do not stall at the same time. Dimensional tolerances could be one possible case, Reference [12]. In manufacturing and assembly, a few blades could be produced with slightly different profiles or with higher stagger angles. These imperfections would cause the inlet air to see these blades at slightly different angles of attack as compared to the other blades. When one of the blades stalls, as a consequence of some instability, the angle of the flow relative to the shaft increases. This increase in flow angle, in addition to blockage attributed to stall, cause part of the oncoming flow to be diverted towards the neighboring blades, thus causing an increase in their angles of attack and leading them to stall. As the blade rotates away from the disturbances, the angle of attack decreases, restoring normal flow over that blade. The region of the stalled flow, known as a stall cell, continues moving from blade to blade and propagates around the annulus.

In a coordinate system attached to the blades, rotating stall moves in a direction opposite to the blade motion at a fraction of the rotor speed. However, in the inertial coordinate system, the stall region propagates in the same direction as the wheel motion.

The reported rotational speed of rotating stall around the annulus of compressor varies from 20 to 75 percent of the rotor speed in the direction of the rotor motion[13]. It has also been reported that the incipient rotating stall cells move faster. Typical frequencies for rotating stall are 10 to 50 times larger than those for surge.

The number of stall cells depends on the compressor at hand; one to nine stalled cells has been reported. Two types of stall associated with the number of stalled cells exist, progressive and abrupt. In progressive stall, a phenomenon involving multiple stalled cells, the pressure ratio after stall reduces gradually. Abrupt stall results in a sudden drop in total-to-total pressure rise, and appears to always involve a single stalled cell.

One of the characteristics of pure rotating stall is that the average flow is steady with respect to time, but the flow has a circumferentially non-uniform mass deficit. During rotating stall, the cyclical variation of the pressures on the blades can cause them to fatigue and eventually break. The flow temperature may also increase due to uneven distribution of shaft work, reducing blade life. A typical plot of the static pressure history measurements taken at a fixed circumferential location at the inlet of an axial compressor under rotating stall conditions is depicted in Figure 2.2[14].

Several types of rotating stall exist[13]:

- **Part-Span**: As illustrated in Figure 2.3[12], only a restricted region of the blade passage, usually the tip, is stalled. Stall near the root has also been reported.
- **Full-Span**: The entire height of the annulus is stalled. Figure 2.4[12] shows the full-span rotating stall with various stalled cells.

- **Small/Large scale**: In this case, a small/large part of annular flow path is blocked.

Figure 2.5 shows a typical rotating stall pattern. When rotating stall occurs at point A on the unstalled branch, the operating point then proceeds to the so-called stalled characteristic at point B, along a straight line AB. If point B is stable, the compressor will remain and operate there, until measures are taken to bring it back to the unstalled branch. Sometimes the deterioration in the performance of an axial compressor with rotating stall is small, and may not be easily detected except as an increase in the compressor noise or by some high-frequency sensors. Recovery from rotating stall is often more difficult than surge[13]. Rotating stall can also serve as the precursor to the more severe and dangerous flow stability, called surge.

2.2 FUNDAMENTALS OF SURGE

Surge is a global 1-D instability that can affect the whole compression system. Surge is characterized by large amplitude limit cycle oscillations in mass flow rate, and pressure rise. Even a complete reversal of the flow is possible. The behavior of surge depends on both the compressor characteristic and the characteristics of the diffuser[13]. Figure 2.6 shows a typical plot of the plenum pressure transient response when an axial compressor experiences surge[14].

In contrast to rotating stall, the average flow through the compressor is unsteady but the flow is circumferentially uniform. Many of the conditions that a compression system experiences during rotating stall are also present in surge. The rotor blades are stressed

by the oscillating flow and the uneven distribution of shaft work; backpressure decreases while the inlet pressure increases. The compressor's noise characteristic changes and pressure fluctuations occur through out the compressor.

In high-speed compressors, the reversal flow can be triggered by a shock wave[3]. The high pressures behind the shock may deform the casing and inlet, and resulting pitching moments can also change the twist of the rotor/stator blades. In low-speed compressors, the surge appears as a moderate pulsing of the flow.

Based on flow and pressure fluctuations, surge can be categorized into four different classes[13]:

- **Mild Surge**: No flow reversal; small periodic pressure fluctuations governed by the Helmholtz resonance frequency.
- **Classic Surge**: No flow reversal; larger oscillations at a lower frequency.
- **Modified Surge**: Combination of classic surge and rotating stall; entire annulus flow fluctuates in axial direction; non-axisymmetric flow.
- **Deep Surge**: Strong version of classic surge; possibility of flow reversal; axisymmetric flow.

In both axial and centrifugal compressors, while increasing the plenum pressure at the compressor exit at a constant rotor speed, a mild surge can occur. The mild surge may be followed by rotating stall or modified surge. A classic or a deep surge may then follow.

2.3 LITERATURE SURVEY OF STUDIES ON ROTATING STALL AND SURGE

The occurrence of the fluid dynamic instabilities was first considered one of the normal operating features of axial compressors. Qualitative explanations of surge have long been known. Stodola[15] and Kearton[16] described the surge phenomenon in 1927 and 1931, respectively. To this author's knowledge, rotating stall was first detected in 1932 in a centrifugal pump impeller[17]. In 1946, it was found that the ducts linked to the compressors could be primary contributors to surge, Reference [12].

Up to this time, researchers assumed that the surge phenomenon was sinusoidal with respect to time, and was associated with Helmholtz resonances. In 1955, an extensive study of rotating stall and surge was presented by Emmons, Pearson and Grant[18]. They predicted the rotational velocity of the stall cell using linear flow theory. Rotating stall and surge are nonlinear phenomena, and this linearized theory limited them to analyzing weak disturbances to the flow. In 1958, Horlock[1] published a book about these two types of flow instabilities, and detailed the state of the art about these phenomena in axial compressors. One of the early attempts to model the one-dimensional flow through the axial compressors in a nonlinear form was by Greitzer[19] in 1976. The first nonlinear analysis of incipient and fully-developed rotating stall was presented by Moore[20]. The extensions to the inlet distortion effects may be found in References [21] and [22]. In 1986, Moore and Greitzer[23-24] presented the theory of post-stall transients in axial compressor.

Much of the work on rotating stall and surge control in the literature was based on the assumption of incompressible flow. Since the beginning of 1990's, the importance of compressibility effects has been recognized and studied. The effects of compressibility on surge can be found in References [25] and [26]. They are based on one-dimensional fluid dynamic equations, and therefore are limited to the surge phenomenon. Incorporation of compressibility effects in two-dimensional fluid dynamic models was presented in Reference [27]. Further details on nonlinear control methods may be found in References [28] through [30]. An exhaustive survey of rotating stall and surge control can be found in Reference [13].

2.3.1 EXPERIMENTAL STUDIES ON COMPRESSOR CONTROL

Surge and rotating stall are highly undesirable phenomena. They can introduce mechanical and thermal loads, and can even cause structural damage. These aerodynamic instabilities reduce the total to total pressure rise and efficiency of the compression system. Unrecoverable stall in gas turbines requires restarting the engine and may also have catastrophic consequences in aircraft jet engines. These instabilities may be avoided by operating away from the surge line. On the other hand, due to the high performance and efficiency obtained near the surge line, it is desirable to operate the compressor close to the surge line. To overcome this dilemma, three different approaches exist: surge/stall avoidance, surge detection and avoidance, and increasing the stall margin approach.

Surge avoidance techniques are known and have been used for a long time in industry and commercial systems. In this approach, the control systems do not allow the compressor to operate on the left side of the surge avoidance line. To locate the surge avoidance line on the compressor map, a safety margin should be specified. This safety margin may be defined based on pressure ratio, corrected mass flow, or a combination of pressure ratio and corrected mass flow. A common safety margin, SM, is based on total pressure ratio and is defined as:

$$SM = \frac{\left(\frac{P_{o2}}{P_{01}}\right)_{Surge} - \left(\frac{P_{o2}}{P_{01}}\right)_{Surge\ Avoidance}}{\left(\frac{P_{o2}}{P_{01}}\right)_{Surge\ Avoidance}} \qquad \textbf{(2.1)}$$

Here $P_{02,}$ and $P_{01,}$ are total pressure at the compressor exit and inlet, respectively. In a multistage axial compressor in a turbojet, it is typical to have a safety margin as high as 25 percent[9], while for a centrifugal pipeline compressor the safety margin is 10 percent[31].

In surge detection and avoidance methods, the onset of instabilities is first detected. The most successful techniques to detect the onset of stall are based on monitoring the pressure and temperature variations or other parameters (e.g. their time derivatives and oscillation frequency) at the compressor inlet or exit. These measurements are compared to the expected values at the surge condition, stored in the control computer. When surge or stall is detected, corrective measures (e.g. bleed) are applied. The advantage of this

technique is that it is not necessary to define a large safety margin, and the compressor can operate close to the surge line. The disadvantages of this technique are the need for large control forces and a very fast-acting control system that will prevent the growth of instabilities into surge. Another weakness of this technique is that it is highly dependent on the compressor being controlled, since different compressors exhibit different behaviors during the onset of surge.

The third control methodology involves increasing the stall margin. This approach may be divided into two different classes: passive surge/stall control and active surge/stall control.

In both active and passive control the characteristic performance map of the compressor is modified and the surge line is shifted to a lower mass flow. By shifting the surge line, the surge avoidance line is also shifted. In other words, some part of the unstable area in the performance map is being stabilized by this approach. An advantage of this methodology is that the compressor now can operate near peak efficiency and high-pressure ratios at lower mass flow rates.

In passive surge/stall, the geometry of the compressor is altered to modify the stall margin. Casing treatments[32-35] and variable guide vanes[36-39] are some the different ways of achieving passive surge/stall control.

Casing treatments, which have been investigated more in axial compressors, the rotor casing is designed so that the amount of blockage in a flow passage is decreased. Thus, rotating stall is suppressed. In this method, the casing is designed with various shaped

grooves: perforated, honeycomb, circumferentially grooved, axial slotted, or blade angle slotted. The effects of a porous casing on stall margin for both uniform and distorted inlet conditions may be found in Reference [32].

The use of variable inlet guide vanes is another way of increasing the stall margin and has been used in both axial and centrifugal compressors. In this method, the incident angle in compressors at lower mass flow rates is reduced and the leading edge separation is prevented. With inlet guide vanes, the direction of the flow at the leading edge is turned such that the angle of attack decreases. Variable inlet guide vanes are also commonly used when starting and accelerating engines to avoid crossing the surge line.

In active stall or surge control, the compressor is equipped with devices such as a bleed valve that can be switched on or off. Generally, active surge/stall control may be divided into two classes: open-loop and closed-loop. In closed-loop control, a feedback law is used to activate the controller, while in the open-loop control no feedback signals are used. Air injection[40], bleeding[40-42], and recirculation (a combination of injection and bleeding) are examples of active surge/stall control.

Air injection is another way of increasing the stall margin and has been used in both axial and centrifugal compressors. In this method, a small amount of high pressure and high velocity air is injected into the compressor upstream of the compressor face. As a result, the flow is energized and the axial velocity component is increased. This reduces the local angles of attack, and the leading edge separation is prevented. The injected air

may be supplied from the diffuser downstream of the compressor or from a separate device.

One of the oldest, and the most investigated approach for increasing the stall margin in axial compressors is bleeding. This technique has been used in both axial and centrifugal compressors. Since the early days of jet engines, bleeding has been the most common approach for avoiding surge during engine acceleration and start-up. Beside the start-up applications, bleeding has also been used to achieve a wide range of operating conditions. The bleed valve is typically located either in the plenum exit or downstream of rotor on the shroud. The concept of bleeding is that at lower mass flow the working fluid does not have enough momentum to overcome the viscous and adverse pressure gradient forces in the plenum. By removing some of the highly pressurized flow downstream of the compressor, flow acceleration can increase and surge-free operation is achieved.

Closed-loop active control was first reported by Epstein et al.[43] in 1989, and the literature on this approach has become extensive over the last decade. This method promises to be an integral part of future engines, the so-called smart or intelligent engines. The closed-loop control devices use a sensor for detecting the growth of instabilities (precursor waves) when a compressor experiences stall conditions. In this method, a control unit processes measured flowfield data, such as temperature, pressure or axial velocity, from a stall-detection device. The stall-detection devices are usually located on the circumference of the compressor casing, either upstream or downstream of

compressor. A feedback law connecting the sensed fluctuations to the rate of bleed is used to stabilize the compressor. The control unit activates a set of actuator devices. There are several types of actuators in use for stabilizing the compression system. Among these, bleed valve actuators have been the most commonly used. Pinsely et al.[42], studied the use of the throttle valve as actuator in a centrifugal compressor surge control, and achieved a 25% reduction in the mass flow rate. Bleed valve control is discussed in References [40]-[42].

Other types of actuators include variable inlet guide vanes, re-circulation, loudspeakers, movable plenum walls, and air injections. Figure 2.7 shows a schematic of these passive and active control methods.

2.3.2 COMPUTATIONAL STUDIES OF COMPRESSOR PERFORMANCE AND CONTROL

As stated in Section 2.1, many attempts have been made to increase the operating range of the compression system using appropriate detection and control devices. Over the past five decades, considerable research has been done on both axial (References [21]-[24] & [44]-[46]), and centrifugal compressors (References [47]-[49]). One goal of these studies is the prediction of component performance, e.g. pressure ratio and efficiency. It is obvious that even a small improvement in the efficiency of a commercial aircraft engine can result in huge saving in yearly fuel costs. Therefore, turbomachinery designers are extremely interested in tools that give good qualitative and quantitative predictions of turbomachinery performance, and may be used in aerodynamic design.

One efficient method for investigating complex flow phenomena in rotating machinery is computational fluid dynamics. The earliest numerical study of compressor instabilities, to this author's knowledge, is the work by Takata and Nagano[50] in 1972. They used a finite difference method to solve the nonlinear flow equations. The flow was treated as incompressible, and Laplace and Poisson equations were used to model the flow within the inlet and exit ducts, respectively.

During the past decade computational fluid dynamics has undergone an impressive evolution, providing engineers and designers with the capability to model and study 3-D unsteady flows. There are several reasons for the scarcity of CFD-based turbomachinery performance calculations in the early literature. One reason is that pressure field calculations are relatively independent of viscous effects and can be obtained with simple models. On the other hand, system losses and efficiency are strongly dependent on viscous effects and require careful attention to the viscous terms, artificial viscosity, turbulence modeling, and grid resolution to obtain satisfactory results. A second reason for the scarcity of CFD studies is the inability of early computers to perform large viscous flow calculations. A third reason is that validation data, such as detailed pressure and velocity measurements, are difficult to obtain in turbomachines, due to the small size and the high speeds of the components involved[62].

In recent literature, several researchers have presented detailed investigations of turbomachinery performance using CFD. However, most of their calculations were extracted from 2-D codes. For example, Davis et al.[51] predicted loss buckets for

transonic compressor cascades in 1986; loss and exit flow angle were calculated for turbine and fan cascades by Chevrin and Vuillez[52] using the 2-D code of Cambier et al.[53]; and the effects of turbulence modeling on turbine blades were studied by Boyle[54].

Thanks to the massive increase in computing power and the development of sophisticated post-processing and visualization tools, time-accurate 3-D simulations of rotary machines are now possible. Furthermore, with the availability of an AGARD Advisory Report for computational test cases of internal flow, researchers now have access to excellent data for validation of the turbomachinery codes. A number of 3-D CFD codes for detailed modeling of turbomachinery flow fields exist. Srivastava and Sankar[55], Dawes[56], Hah et al.[57], Adamczyk et al.[58], Hall[59], Hathaway et al.[60], Wood at al.[61], and Chima et al.[62], among others, have developed 3-D codes that have the capability to analyze unsteady turbomachinery flow with multiple blade passages and/or rotor-stator interactions. However, most of these applications have been applied only to steady-state phenomena in axial and radial compressors. There has been little or no effort in numerically modeling and studying off-design conditions by CFD methods using the full Navier-Stokes equations. Many researchers have also simulated rotating stall and surge in axial compressors using simple 1-D and 2-D codes, e.g. References [63]-[65].

In an effort to model unsteady flow within a compression system, a 3-D compressible unsteady flow solver for turbomachinery has been developed at Georgia Institute of Technology by Niazi, Stein and Sankar, References [66]-[70]. This solver is capable of solving multiple flow passages in an inertial reference frame, and can be

extended to multistage compression systems that are currently used in gas turbines. In a previous study, this code has been applied to a NASA low speed centrifugal compressor (LSCC) configuration at both design and off-design conditions[66-67]. The CFD simulations captured the onset of surge within the compression system. Two different active control schemes, a diffuser bleed valve and air injection, were implemented. It was shown that these control schemes could suppress the stall and significantly extend the useful operating range of the compressor[66-67]. Stein[70] simulated surge with both steady and pulsed air injection control in centrifugal compressors using this three-dimensional time accurate compressible flow solver, while considering one single flow passage. To the knowledge of this author, this is the first time such flow control simulations based on the full set of 3-D Navier-Stokes equations have been done.

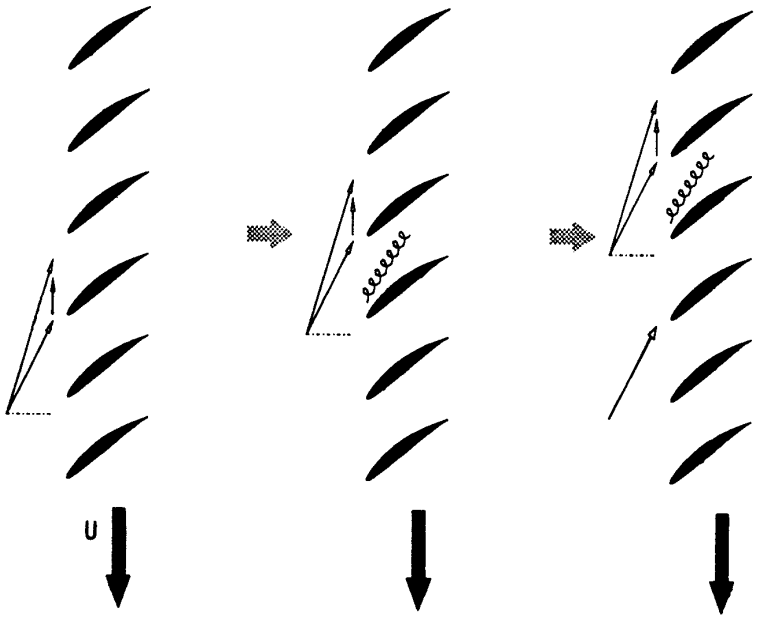

Figure 2.1 Rotating stall inception.

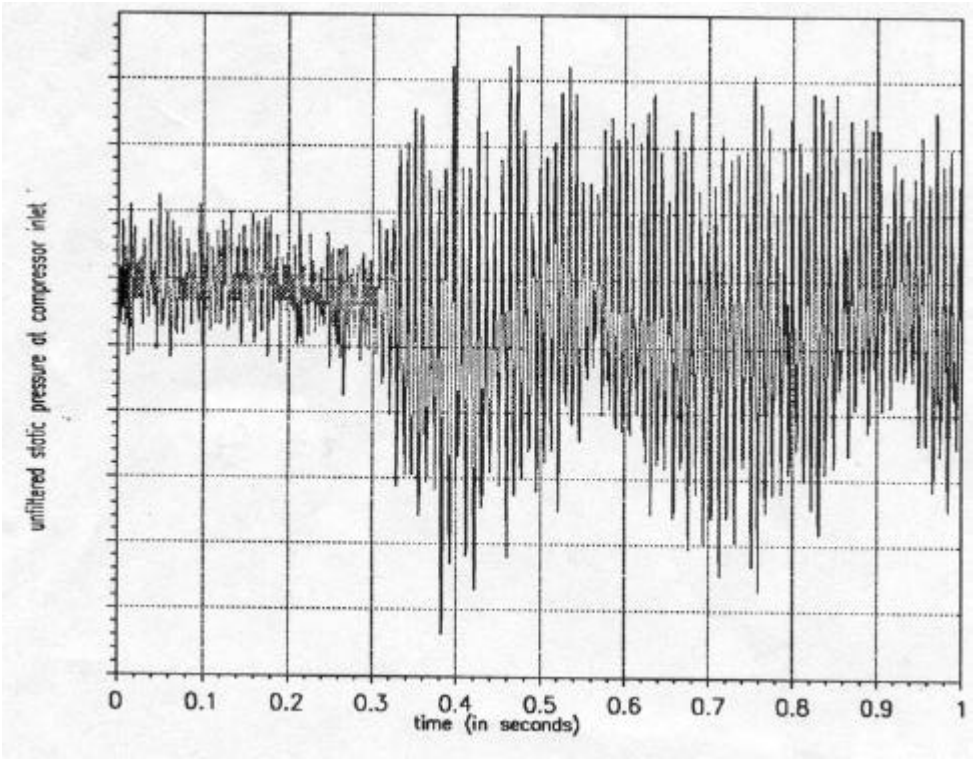

Figure 2.2 Transient response of system in rotating stall, Reference [14].

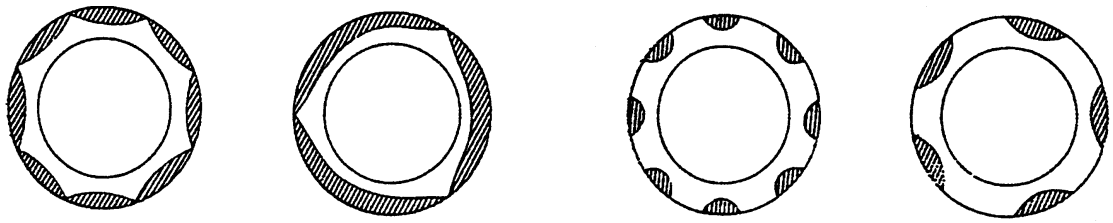

Figure 2.3 Part-Span rotating stall with different stalled cells, Reference [12].

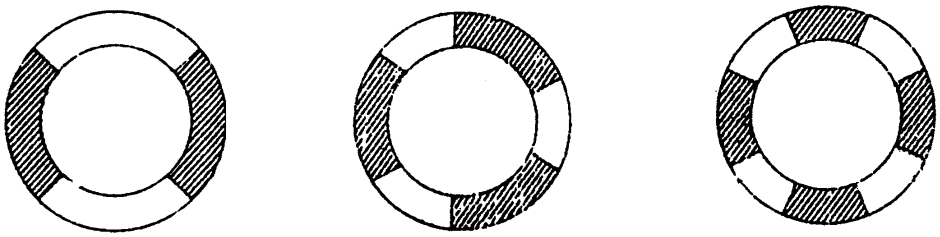

Figure 2.4 Full-Span rotating stall with different stalled cells, Reference [12].

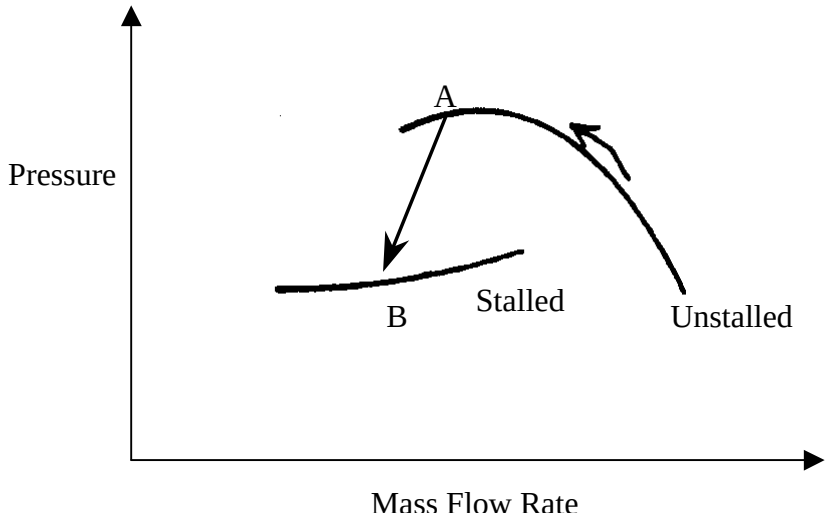

Figure 2.5 Compressor map with the stalled flow characteristic, Reference [13].

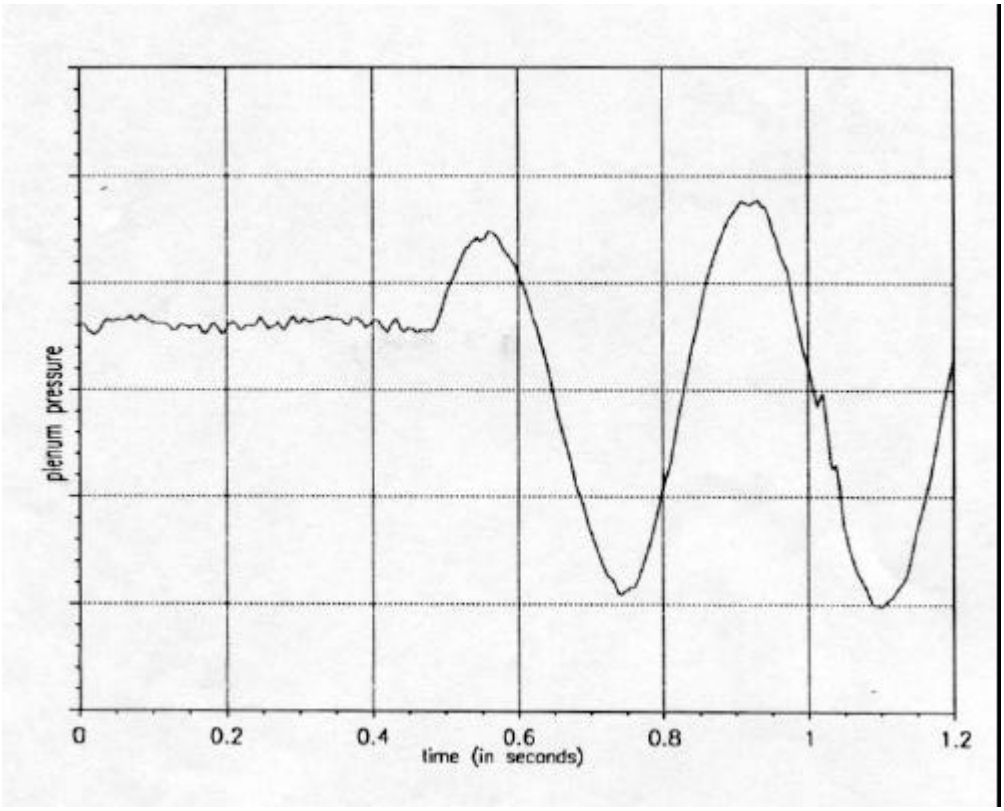

Figure 2.6 Transient response of system in surge, Reference [14].

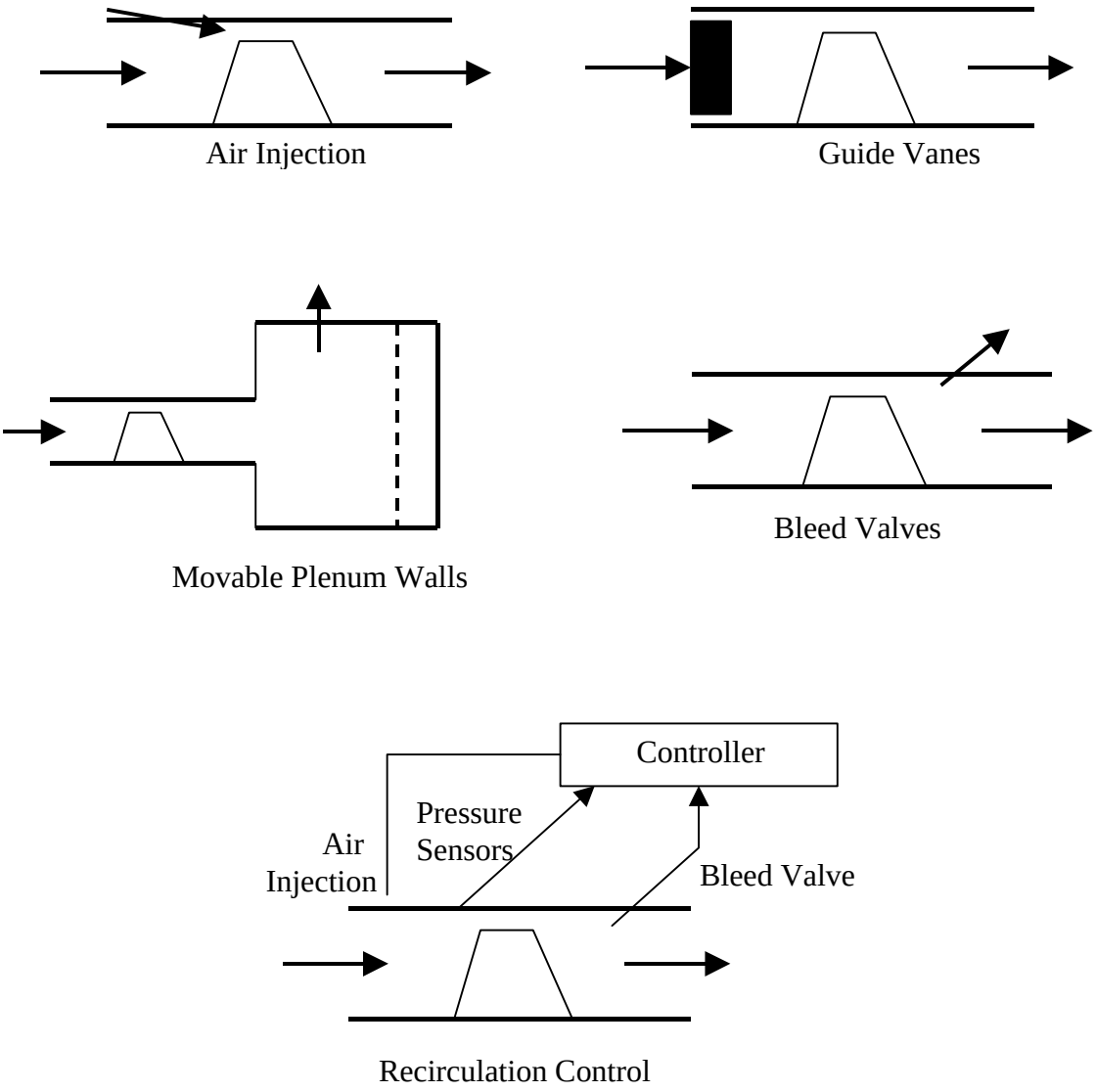

Figure 2.7 Types of active and passive compressor control schemes.

CHAPTER III

MATHEMATICAL AND NUMERICAL FORMULATION

In order to analyze flow details in compressors, solution of the 3-D Navier-Stokes equations is required. The complex nature of the governing equations limits the analytical solutions to simple flows and configurations. Therefore, numerical techniques are required for more complex problems. In this chapter the mathematical formulation and numerical tools employed in this study are documented. A comprehensive overview of CFD methods may be found in References [71] and [72].

In Section 3.1 unsteady compressible flow equations are presented. The numerical discretization process and an approximate factorization solution algorithm used in the flow solver are given in Sections 3.2 and 3.3, respectively. The turbulence modeling method implemented in this work is discussed in Section 3.4. In Section 3.5 the initial and boundary conditions are described.

3.1 GOVERNING EQUATIONS

The system of partial differential equations for the conservation of mass, momentum and energy in fluid flow are known as the Navier-Stokes equations. These equations are derived from first-principles and from thermodynamic considerations. The Navier-Stokes equations describe the physics of 3-D, unsteady compressible viscous flow,

subject to some stress-strain rate relationships. In this study, calorically perfect Newtonian fluids, obeying the Stokes linear stress-strain rate law, have been considered. In three-dimensional Cartesian coordinates, the conservative form of the equations in vector form is given below:

$$\frac{\partial q}{\partial t}+\frac{\partial E}{\partial x}+\frac{\partial F}{\partial y}+\frac{\partial G}{\partial z}=\frac{\partial R}{\partial x}+\frac{\partial S}{\partial y}+\frac{\partial T}{\partial z} \qquad \textbf{(3-1)}$$

Here, q is the state vector with unknown flow variables: density ρ, velocity components in x, y, z direction (u, v, w, respectively) and total energy, E_t. The quantities E, F, G are inviscid flux terms, and R, S, T represent viscous terms. The state vector and inviscid flux terms are:

$$q=\begin{Bmatrix} r \\ ru \\ rv \\ rw \\ E_t \end{Bmatrix}, \quad E=\begin{Bmatrix} ru \\ ru^2+p \\ ruv \\ ruw \\ (E_t+p)u \end{Bmatrix}, \quad F=\begin{Bmatrix} rv \\ ruv \\ rv^2+p \\ rvw \\ (E_t+p)v \end{Bmatrix}, \quad G=\begin{Bmatrix} rw \\ ruw \\ ruw \\ rw^2+p \\ (E_t+p)w \end{Bmatrix} \qquad \textbf{(3-2)}$$

Furthermore, $E_t = r\left[C_V T+\frac{1}{2}(u^2+v^2+w^2)\right]$ **(3-3)**

Here, C_V is the specific heat at constant volume and T is the temperature. Also, p is pressure, and is related to total energy and velocity as follows:

$$p = rRT \tag{3-4}$$

$$p = (g - 1)\left[E_t - \frac{1}{2} r(u^2 + v^2 + w^2)\right] \tag{3-5}$$

In Equation (3-5), γ is the specific heat ratio, and since the working fluid is air, a value of 1.4 is used. The viscous terms are:

$$R = \begin{Bmatrix} 0 \\ t_{xx} \\ t_{xy} \\ t_{xz} \\ ut_{xx} + vt_{xy} + wt_{xz} + q_x \end{Bmatrix}, \quad S = \begin{Bmatrix} 0 \\ t_{yx} \\ t_{yy} \\ t_{yz} \\ ut_{y}x + vt_{yy} + wt_{yz} + q_y \end{Bmatrix},$$

$$T = \begin{Bmatrix} 0 \\ t_{zx} \\ t_{zy} \\ t_{zz} \\ ut_{zx} + vt_{zy} + wt_{zz} + q_z \end{Bmatrix} \tag{3-6}$$

where

$$
\begin{aligned}
t_{xx} &= l\,(u_x + v_y + w_z) + 2mu_x \\
t_{xy} &= t_{yx} = m(u_y + v_x) \\
t_{xz} &= t_{zx} = m(u_z + w_x) \\
t_{yy} &= l\,(u_x + v_y + w_z) + 2mu_y \\
t_{yz} &= t_{zy} = m(v_z + w_y) \\
t_{zz} &= l\,(u_x + v_y + w_z) + 2mu_z
\end{aligned}
\qquad \textbf{(3-7)}
$$

and

$$
\begin{aligned}
q_x &= -k\frac{\partial T}{\partial x} \\
q_y &= -k\frac{\partial T}{\partial y} \\
q_z &= -k\frac{\partial T}{\partial z}
\end{aligned}
\qquad \textbf{(3-8)}
$$

In these equations, μ is the molecular viscosity and k is the thermal heat conduction coefficient of the fluid. In Equation (3-7), l, from the Stokes hypothesis, is $-\frac{2}{3}m$.

All quantities in the Navier-Stokes equations have been non-dimensionalized by their corresponding reference values. The following reference parameters have been used in this work:

$$
\begin{aligned}
L_{ref} &= Diameter\ of\ the\ rotor,\ at\ the\ blade\ trailing\ edge \\
V_{ref} &= a_{\text{ambient, upstream of the inlet}} = a_\infty \\
r_{ref} &= r_{\text{ambient, upstream of the inlet}} = r_\infty \\
p_{ref} &= \frac{r_{ref} V_{ref}^2}{g}
\end{aligned}
\qquad \textbf{(3-9)}
$$

3.2 DISCRETIZATION OF THE GOVERNING EQUATIONS

Analytical solution of the Navier-Stokes equations is limited to simple geometries. Therefore, for complex geometry and flows with highly non-linearity, numerical techniques must be used to find approximate solutions. In numerical methods, solutions are found for discrete points at different time levels. Several techniques, such as finite difference methods, finite volume methods, and finite element methods, exist for numerically solving the Navier-Stokes equations. The finite volume method is commonly used in fluid dynamic problems. One of the advantages of this method is that discontinuous phenomena, such as shock waves, can be handled. In the finite volume method in three-dimensional space, the flow is divided into a finite number of hexagonal cells.

In this study, the 3-D unsteady compressible Reynolds-averaged Navier-Stokes equations are recast in integral form, and solved using a finite volume scheme.

The integral form of Equation (3-1) is:

$$\iiint_V \frac{\partial q}{\partial t} dV + \iint_S (E\vec{i} + F\vec{j} + G\vec{k}) \cdot \vec{n} dS - \iint_S q\vec{V}_G \cdot \vec{n} dS = \iint_S (R\vec{i} + S\vec{j} + T\vec{k}) \cdot \vec{n} ds \quad \textbf{(3-10)}$$

Here, V and S refer to the control volume and control surface area respectively, and $\vec{n}$ represents the outward normal vector to surface S. The term $\vec{V}_G$ refers to the velocity

of the surface S. In Equation (3-10), the state vector q is evaluated at the cell vertices, as shown in Figure 3.1, and the surface integrals are computed at the six faces surrounding the control volume:

$$\iint_s (E\vec{i} + F\vec{j} + G\vec{k}) \cdot \vec{n} dS - \iint_S q\vec{V}_G \cdot \vec{n} dS = \sum_{All\ Faces} (En_x + Fn_y + Gn_z)\Delta S - \left[q\vec{V}_G \cdot \vec{n}\Delta S\right]$$

$$= \left[\widehat{E}_{i+\frac{1}{2},j,k} + \widehat{E}_{i-\frac{1}{2},j,k}\right] + \left[\widehat{F}_{i,j+\frac{1}{2},k} + \widehat{F}_{i,j-\frac{1}{2},k}\right] + \left[\widehat{G}_{i,j,k+\frac{1}{2}} + \widehat{G}_{i,j,k-\frac{1}{2}}\right]$$

(3-11)

where $\widehat{E}\Big|_{i\pm\frac{1}{2},j,k} = \left[En_x + Fn_y + Gn_z - q(\vec{V}_G \cdot \vec{n})\right]\Delta S\Big|_{i\pm\frac{1}{2},j,k}$

$$\widehat{F}\Big|_{i,j\pm\frac{1}{2},k} = \left[En_x + Fn_y + Gn_z - q(\vec{V}_G \cdot \vec{n})\right]\Delta S\Big|_{i,j\pm\frac{1}{2},k} \quad \textbf{(3-12)}$$

$$\widehat{G}\Big|_{i,j,k\pm\frac{1}{2}} = \left[En_x + Fn_y + Gn_z - q(\vec{V}_G \cdot \vec{n})\right]\Delta S\Big|_{i,j,k\pm\frac{1}{2}}$$

Viscous fluxes, R, S, and T, likewise are handled as follows:

$$\iint_s (R\vec{i} + S\vec{j} + T\vec{k}) \cdot \vec{n} dS = \sum_{All\ Faces} (Rn_x + Sn_y + Tn_z)\Delta S \quad \textbf{(3-13)}$$

The inviscid fluxes, $\hat{E}$, $\hat{F}$, and $\hat{G}$ are calculated implicitly using Roe's flux difference scheme[73-78] as described by Liu and Vinokur[79]. At a cell interface, the numerical flux f_{Num} (which is an approximation to $\hat{E}$, $\hat{F}$, or $\hat{G}$) is given by:

$$f_{Num} = \left[\overbrace{\frac{1}{2}[f(q_L) + f(q_R)]}^{\text{Physical Flux Term}} - \overbrace{\frac{1}{2}\left[\left|\tilde{A}(q_L, q_R)\right|(q_R - q_L)\right]}^{\text{Artificial Viscosity Term}} \right] \Delta S \qquad \textbf{(3-14)}$$

where

$$f(q_L) = \begin{bmatrix} r_L U_L \\ r_L U_L u_L + p_L n_x \\ r_L U_L v_L + p_L n_y \\ r_L U_L w_L + p_L n_z \\ U_L H_{0L} - p_L n_t \end{bmatrix}, \qquad f(q_R) = \begin{bmatrix} r_R U_R \\ r_R U_R u_R + p_R n_x \\ r_R U_R v_R + p_R n_y \\ r_R U_R w_R + p_R n_z \\ U_R H_{0R} - p_R n_t \end{bmatrix} \qquad \textbf{(3-15)}$$

and ΔS is the cell area of the face where f_{Num} is calculated. The quantity $\tilde{A}$ is defined as: $\tilde{A} = T\left|\Lambda\right|T^{-1}$, assuming that the original matrix is given by $A = \frac{\partial f}{\partial q} = T\Lambda T^{-1}$. The matrix T contains the eigenvectors of A, which Λ contains the eigenvalues. These quantities are in general complex number, but are real numbers for Euler equations. In Equation (3-14), q_L and q_R are the primitive variables vectors to the left and the right of the cell interfaces and are defined as:

$$q_L = \begin{bmatrix} r_L \\ u_L \\ v_L \\ w_L \\ p_L \end{bmatrix}, \qquad q_R = \begin{bmatrix} r_R \\ u_R \\ v_R \\ w_R \\ p_R \end{bmatrix} \tag{3-16}$$

The quantities, U and H_0 are the relative velocity normal to the cell face, and total enthalpy, respectively and are defined as:

$$U = (\vec{V} - \vec{V}_G) \cdot \vec{n} \tag{3-17}$$

$$H_0 = E_t + p \tag{3-18}$$

and

$$n_t = -\vec{V}_G \cdot \vec{n} \tag{3-19}$$

Again, $\vec{V}_G$ is the grid velocity at the face where f_{Num} is being calculated, and $\vec{n}$ is the unit normal vector to this face.

A four-point stencil, with Roe's Superbee limiter[78] to control the high frequency oscillations near shocks, was used to compute the left and right values of primitive variable vectors at each cell interface. For example, q_L and q_R at cell face $i+\frac{1}{2}$, as shown in Figure 3.2, can be written as:

$$q_L = q_i + \frac{1}{6}\Phi^{+}_{i-\frac{1}{2}}(q_i - q_{i-1}) + \frac{1}{3}\Phi^{-}_{i+\frac{1}{2}}(q_{i+1} - q_i)$$

$$q_R = q_{i+1} - \frac{1}{3}\Phi^{+}_{i+\frac{1}{2}}(q_{i+1} - q_i) - \frac{1}{6}\Phi^{-}_{i+\frac{3}{2}}(q_{i+2} - q_{i+1}) \qquad \textbf{(3-20)}$$

and

$$\Phi^{+}_{i-\frac{1}{2}} = \Phi(r^{+}_{i-\frac{1}{2}}), \quad \Phi^{-}_{i+\frac{1}{2}} = \Phi(r^{-}_{i+\frac{1}{2}})$$

$$r^{+}_{i-\frac{1}{2}} = \frac{q_{i+1} - q_i}{q_i - q_{i-1}} \quad , \quad r^{-}_{i+\frac{1}{2}} = \frac{q_i - q_{i-1}}{q_{i+1} - q_i} \qquad \textbf{(3-21)}$$

$$\Phi(r) = \max[0, \min(2r,1), \min(r,2)]$$

The second term in Equation (3-14), using Liu and Vinokur[79] formula, can be expanded as:

$$\left|\tilde{A}(q_L, q_R)\right|(q_R - q_L) = \left|\tilde{l}_1\right|\Delta q + d_1\tilde{q}^{*} + d_2 N_n \qquad \textbf{(3-22)}$$

where

$$d_1 = \left(-\left|\tilde{l}_1\right| + \frac{\left|\tilde{l}_2\right| + \left|\tilde{l}_3\right|}{2}\right)\frac{\Delta p}{\tilde{a}^2} + \frac{\left|\tilde{l}_2\right| - \left|\tilde{l}_3\right|}{2}\frac{\tilde{r}\Delta U}{\tilde{a}} \qquad \textbf{(3-23)}$$

$$d_2 = \left(-\left|\tilde{l}_1\right| + \frac{\left|\tilde{l}_2\right| + \left|\tilde{l}_3\right|}{2} \right) \tilde{r} \Delta U + \frac{\left|\tilde{l}_2\right| - \left|\tilde{l}_3\right|}{2} \frac{\Delta p}{\tilde{a}} \qquad \textbf{(3-24)}$$

$$\tilde{q}^* = \begin{bmatrix} 1 \\ \tilde{u} \\ \tilde{v} \\ \tilde{w} \\ \dfrac{\tilde{H}_0}{\tilde{r}} \end{bmatrix} \quad , \quad N_n = \begin{bmatrix} 0 \\ n_x \\ n_y \\ n_z \\ \tilde{U} \end{bmatrix} \Delta S \qquad \textbf{(3-25)}$$

and

$$\begin{aligned} \tilde{l}_1 &= \tilde{U} \\ \tilde{l}_2 &= \tilde{U} + \tilde{a} \\ \tilde{l}_3 &= \tilde{U} - \tilde{a} \end{aligned} \qquad \textbf{(3-26)}$$

In Equations (3-22) through (3-26), the quantities marked by "~" are calculated using Roe averaging, defined as:

$$\tilde{r} = \sqrt{r_L r_R} \qquad \textbf{(3-27)}$$

$$\tilde{u} = \frac{\sqrt{r_L} u_L + \sqrt{r_R} u_R}{\sqrt{r_L} + \sqrt{r_R}} \qquad \textbf{(3-28)}$$

$$\tilde{v} = \frac{\sqrt{r_L} v_L + \sqrt{r_R} v_R}{\sqrt{r_L} + \sqrt{r_R}} \quad \textbf{(3-29)}$$

$$\tilde{w} = \frac{\sqrt{r_L} w_L + \sqrt{r_R} w_R}{\sqrt{r_L} + \sqrt{r_R}} \quad \textbf{(3-30)}$$

$$\tilde{H} = \frac{\sqrt{r_L} H_L + \sqrt{r_R} H_R}{\sqrt{r_L} + \sqrt{r_R}} \quad \textbf{(3-31)}$$

$$\tilde{U} = (\tilde{u}\vec{i} + \tilde{v}\vec{j} + \tilde{w}\vec{k}) \cdot \vec{n} - \vec{V}_G \cdot \vec{n} \quad \textbf{(3-32)}$$

The difference, Δ, in Equations (3-22) through (3-24) represents the change in the quantities across the cell interface, for example:

$$\Delta p = p_R - p_L \quad \textbf{(3-33)}$$

3.3 NUMERICAL SOLUTION OF THE DISCRETIZED EQUATIONS

The 3-D unsteady compressible Reynolds averaged Navier-Stokes equations are solved numerically using a time marching scheme. This involves solving the governing equations at each time step by marching in time from an initial flow condition with appropriate boundary conditions, discussed later in Section 3.5.

As seen earlier, the discretized form of the governing equation is:

$$\frac{(q\Delta V)_{i,j,k}^{n+1} - (q\Delta V)_{i,j,k}^{n}}{\Delta t} = -\sum_{All\ Faces} f_{Num}\Delta S - \sum_{All\ Faces}\left(Rn_x + Sn_y + Tn_z\right)\Delta S \tag{3-34}$$

This equation set is highly nonlinear, and links the finite volume cell (i, j, k) to its neighbors (i+1, j, k), (i+2,j,k) etc. Direct numerical solution of this equation set is not feasible. A non-iterative scheme, which may be viewed as the first iteration scheme, was used.

All terms in Equation (3-34) were first expanded about known flow quantities at the time level "n":

$$\left(\sum_{All\ Faces} f_{Num}\Delta S\right)^{n+1} = \left(\sum_{All\ Faces} f_{Num}\Delta S)\right)^{n} + \sum_{All\ Faces}\frac{\partial f_{Num}}{\partial q}(q^{n+1} - q^{n})\Delta S \tag{3-35}$$

The viscous terms were logged by one time step. That is:

$$\left[\sum_{All\ Faces}\left(Rn_x + Sn_y + Tn_z\right)\Delta S\right]^{n+1} = \left[\sum_{All\ Faces}\left(Rn_x + Sn_y + Tn_z\right)\Delta S\right]^{n} \tag{3-36}$$

Bringing the unknown quantities to the left side, we get:

$$\frac{(\Delta q)^n}{\Delta t}V + \sum \widehat{A}(\Delta q)^n = -\left(\sum f_{Num}\Delta S\right)^n - \left(\sum (Rn_x + Sn_y + Tn_z)\right)^n \quad \textbf{(3-37)}$$

where $(\Delta q)^n = q^{n+1} - q^n$.

Computing $\widehat{A} = \frac{\partial f_{Num}}{\partial q}$ is costly. Instead, the following approximate form was used:

$$\widehat{A} = \left[\left(\frac{\partial E}{\partial q}n_x + \frac{\partial F}{\partial q}n_y + \frac{\partial G}{\partial q}n_z\right) - \vec{V}_G \cdot \vec{n}\right]\Delta S - \left|l\right|_{\max} \mathrm{I}\,\Delta S \quad \textbf{(3-38)}$$

where $\left|l\right|_{\max}$ is given by:

$$\left|l\right|_{\max} = \left|\left(\vec{V} - \vec{V}_G\right)\cdot \vec{n}\right| + a \quad \textbf{(3-39)}$$

Finally, $(\Delta q)_{\text{cell face}}$ is defined as the average of (Δq) at all centers. This leads to a seven-diagonal system linking the (Δq) value at node (i, j, k) with its five neighbors (i±1, j, k), (i, j±1, k), and (i, j, k±1).

This seven diagonal system of linear equations was solved by a three-factor scheme. The factorization algorithm has been described in detail by Pulliam et al.[80]. Details of the equations, the algorithm, and sample numerical calculations can be found in that report, and many classical text books.

The solution of the matrix equations is obtained through a block lower-upper decomposition (LU) and the application of the Thomas algorithm[71]. The advantage of this algorithm is that direct inversions of the entire block matrices are not required.

3.4 TURBULENCE MODELING

In the most practical flows within turbomachines, the Reynolds number is high and the flow is turbulent. Time and length scales of the turbulent flows are extremely small. To capture the turbulence effects directly from the Navier-Stokes equations, the grid resolution would need to be extremely high. To reduce the computational time, the RANS (Reynolds Average Navier-Stokes System of equations) are solved in this work, which simply requires replace of m and k with $(\mu + \mu_t)$ and $(k + k_t)$ respectively, where μ_t and k_t are "eddy" viscosity and "eddy" conductivity, respectively.

In this work, a one-equation turbulence model, the Spalart-Allmaras[81] model, has been used for computing $\mu_t=\rho\nu_t$. Also, $k_t = \frac{m_t c_p}{\mathrm{Pr}_t}$.

This model involves a number of constants:

$c_{b1} = 0.1335, \quad c_{b2} = 0.622, \quad s = 2/3, \quad k = 0.41, \quad c_{w1} = \frac{c_{b1}}{k^2} + \frac{(1+c_{b2})}{s}$

c_{w2} = 0.3, c_{w3} = 2, c_{v1} = 7.1, c_{t1} = 1, c_{t2} = 2, c_{t3} = 1.1 , c_{t4} = 2

The eddy viscosity, n_t , is given by:

$$n_t = \tilde{n} f_{v1} \ , \qquad f_{v1} = \frac{c^3}{c^3 + c_{v1}^3} \ , \qquad c = \frac{\tilde{n}}{n} \tag{3-40}$$

Here, n is the molecular viscosity. The quantity $\tilde{n}$ is the working variable and can be calculated by solving the following partial differential equation

$$\frac{D\tilde{n}}{Dt} = c_{b1}(1 - f_{t2})\tilde{S}\tilde{n} + \frac{1}{s}\left[\nabla.((n + \tilde{n})\nabla\tilde{n} + c_{b2}(\nabla\tilde{n})^2\right] + \left[c_{w1} f_w - \frac{c_{b1}}{k^2} f_{12}\right]\left[\frac{\tilde{n}}{d}\right]^2 + f_{t1}\Delta U^2 \tag{3-41}$$

Where S is the magnitude of the vorticity,

$$\tilde{S} = S + \frac{\tilde{n}}{k^2 d^2} f_{v2} \quad , \qquad f_{v2} = 1 - \frac{c}{1 + c f_{v1}} \tag{3-42}$$

Here, d is the distance to the closest wall.

The function f_w is:

$$f_w = g\left[\frac{1+c_{w3}^6}{g^6+c_{w3}^6}\right]^{1/6} \text{, where } g = r + c_{w2}(r^6 - r) \quad , \quad r = \frac{\tilde{n}}{\tilde{S}k^2d^2} \qquad \textbf{(3-43)}$$

The wall boundary condition is $\tilde{n} = 0$. In the free-stream, $\tilde{n} = 0$ is best, provided numerical errors don't push $\tilde{n}$ to negative values near the edge of the boundary layer. The same is applied to the initial condition. The function f_{t2} is:

$$f_{t2} = c_{13}\exp(-c_{14}l^2) \qquad \textbf{(3-44)}$$

Finally, the trip function f_{t1} is obtained from the following equation:

$$f_{t1} = c_{t1}g_t\exp(-c_{12}\frac{w_t^2}{\Delta U^2}\left[d^2 + g_t^2 d_t^2\right] \qquad \textbf{(3-45)}$$

where $g_t = \min(0.1, \frac{\Delta U}{w_t \Delta z})$ and w_t is the wall vorticity at the trip point and d_t is the distance from the field point to the trip point, a user specified transition location.

This PDE was also recast in an integral form, and solved using a three-factor approximate factorization scheme.

3.5 INITIAL AND BOUNDARY CONDITIONS

Since the Navier-Stokes equations are parabolic in time and elliptic in space, initial and boundary conditions must be supplied and play a significant role in obtaining a meaningful solution. In this section, the implementation of the initial and boundary conditions is presented.

3.5.1 INITIAL CONDITIONS

At the start of the calculations, the flow properties everywhere in the system are assumed to be uniform, what is called as a cold start. For example, the pressure values equal the downstream pressure, and the u- velocity is set to a value consistent with the specified total temperature T_0 at the inlet. As the compressor begins to draw the fluid in, the pressure at the inlet drops relative to the outflow. The mass flow rate begins to gradually change with time. It reaches either an asymptotically steady state or a limit cycle oscillation, depending on whether the compressor is operating close to design conditions, or at off-designed stalled conditions. The analysis can also use a previously stored solution file with a corresponding grid file, to restart the computations. In this manner, the time-accurate calculations for the compressor are simply a continuation or restart from the previous solution. In the present method the grid and solution are stored every few hundred time steps, based on the user input, and these files may be used to continue the calculations or visualize the flow field.

3.5.2 BOUNDARY CONDITIONS

Figure 3.3 shows the different types of boundary conditions on a compressor flow passage. The following boundary conditions have been implemented in the analysis:

Inflow Boundary: At this boundary, the stagnation temperature, T_0 , and the total pressure, p_0 , are assumed to be known. In the simulation of a compressor drawing the air from the atmosphere, these quantities may be set as ambient conditions. In a multistage compressor analysis, these quantities will be known at the downstream boundary of the previous stage. The tangential components of velocity at the inflow boundary are set to zero, assuming that there is no swirl at the inlet. It is possible within the framework of the present boundary conditions to prescribe swirl, a non-uniform total pressure distribution, and a non-uniform total temperature at the inlet. The fifth equation applied at the inlet boundary condition is the one-dimensional Riemann characteristic equation, modeling the effects of acoustic disturbances leaving the computational field through the inlet face. This equation is:

$$\frac{\partial R_5}{\partial t} + (V_n - a)\frac{\partial R_5}{\partial s} = 0 \qquad \textbf{(3-46)}$$

where $R_5 = \dfrac{2a}{g-1} - V_n$ and s is the distance in a direction normal to the inlet face.

Neglecting $\frac{\partial R_5}{\partial t}$, at every step, the speed of sound, a, and normal velocity, u_n are found at the inflow boundary from the relation:

$$\frac{\partial R_5}{\partial s} = 0 \qquad \textbf{(3-47)}$$

$$R_5\big|_{inlet} = R_5\big|_{\text{interior}} \qquad \textbf{(3-48)}$$

Or,

$$\frac{2a}{g-1} - u_n = \frac{2a}{g-1} - u_n\Big|_{Interior}$$

$$\frac{a^2}{g-1} + \frac{u_n^2}{2} = \frac{a_0^2}{g-1} \qquad \textbf{(3-49)}$$

After computing the speed of sound and temperature, T, isentropic relations are used to find the values of the density ρ and pressure p at the inflow boundary. Neglecting $\frac{\partial R_5}{\partial t}$ was considered acceptable because the flow properties varied very slowly with time at the inlet.

Outflow Boundary: It was assumed in this study that the flow from the vaneless diffuser downstream of the rotor exhausts into a plenum chamber with a constant volume, V_p. Figure 3.4 shows a schematic of the compressor outflow boundary coupled with the plenum. Conservation of mass in the plenum can be written as:

$$\left.\frac{dm}{dt}\right|_{\text{plenum}} = (\dot{m}_p - \dot{m}_t) \tag{3-50}$$

$$\left.\frac{dm}{dt}\right|_{\text{plenum}} = \left.\frac{d(rV)}{dt}\right|_{\text{plenum}} \tag{3-51}$$

Here, $\dot{m}_P$ is the mass flow rate at the diffuser exit, and $\dot{m}_t$ represents the mass flow rate at the plenum throttle, and V is the volume of the plenum and is constant, therefore:

$$\left.\frac{dm}{dt}\right|_{\text{plenum}} = V\left.\frac{dr}{dt}\right|_{\text{plenum}} \tag{3-52}$$

Inserting Equation (3-52) into Equation (3-50), we have:

$$V\left.\frac{dr}{dt}\right|_{\text{plenum}} = \dot{m}_p - \dot{m}_t \tag{3-53}$$

The relationship between density and pressure is obtained by assuming isentropic state in the plenum:

$$\left.\frac{\partial p}{\partial r}\right|_{\text{plenum}} = a^2_{\text{plenum}} \tag{3-54}$$

The combination of Equation (3-54) and (3-53) gives the plenum pressure formula:

$$\frac{dp_p}{dt} = \frac{a_p^2}{V_p}(\dot{m}_p - \dot{m}_t) \qquad \textbf{(3-55)}$$

A first order discretization of Equation (3-55) gives:

$$p_p^{n+1} = p_p^n + K(\dot{m}_p - \dot{m}_t) \qquad \textbf{(3-56)}$$

where a value of 0.20 for K is used in this study. This value determines the natural frequency of the plenum chamber, and indirectly determines surge. The quantity $\dot{m}_t$ is an input parameter that represents the nominal mass flow rate and lets the compressor run at different operating conditions. All other quantities such as the density and the three components of velocity are extrapolated from the interior.

Solid walls: At the solid walls, a no slip boundary condition is used. This condition is applied to the hub, casing and blade surfaces. The velocity on the walls of the inlet and the diffuser is set to zero, while the velocity for grid points on the compressor blades and the shaft, that part which is moving, is set equal to $\vec{\Omega} \times \vec{r}$. The pressure, density and temperature values at the solid surfaces are found from the interior, using relationships such as $\partial p/\partial n = \partial T/\partial n = \partial \rho/\partial n = 0$, where n represents the direction normal to the solid

surface. Density, and pressure on the hub and shroud are all directly extrapolated from the interior. On impeller surfaces, because of the non-orthogonality of the cells around the blade surfaces, especially near the leading and trailing edges, a normal momentum equation, described by Pulliam et al.[85], is used in the normal direction to the blade surfaces.

Periodicity: Since simulation of the entire flow in a compressor requires significant computations and is very expensive, usually just a few of the blade passages are modeled. Therefore, it is assumed that the flow through first blade and the last blade passage are nearly identical and a periodic boundary condition is applied. At the blade-to-blade interface boundaries, the flow properties are computed by averaging the properties on either side of the periodic boundary. Figure 3.5 illustrates the periodic boundary conditions for blocks A and B.

Zonal Boundary: As shown in Figures 3.3 and 3.5, neighboring zones share grid lines on their boundaries. The flow properties at these boundaries are computed by taking the average of the properties on the neighboring points, as shown in Figure 3.5.

Bleed Boundary: In this study, both open-loop and closed-loop control methodologies using steady and unsteady bleeding were studied. In both control methods, bleed valves are implemented circumferentially downstream of rotor, located on the shroud. In the open-loop control, a fraction of the mass flow is removed through a valve at a fixed rate. A schematic of the open-loop control used in this study is shown in Figure 3.6. The numerical implementation of the bleed boundary condition into the flow

solver requires user-specification of the bleed valves location, bleed valve area, A_b, and bleed mass flow rate, $\dot{m}_b$. From this information, the normal velocity may be written as:

$$u_n = \frac{\dot{m}_b}{r_b A_b} \tag{3-57}$$

Density, pressure and the two tangential components of velocity are extrapolated from the interior, consistent with the subsonic flow at this boundary.

While simulating the closed-loop control, the mass flow rate through the bleed valve is linked to pressure upstream of the compressor face by a control unit. The mass flow rate through the bleed valve is controlled by the instantaneous amplitude of pressure fluctuations sensed by the "computational" probes, which in this work were located near 30% of the tip chord, upstream of the compressor face. The bleed valve was activated when the pressure sensors upstream of compressor face experienced high-pressure fluctuations, as discussed in Chapter VI. Figure 3.7 illustrates the schematic of the closed-loop control system used in this study. As in open-loop control, the density and the tangential velocities are extrapolated from the interior.

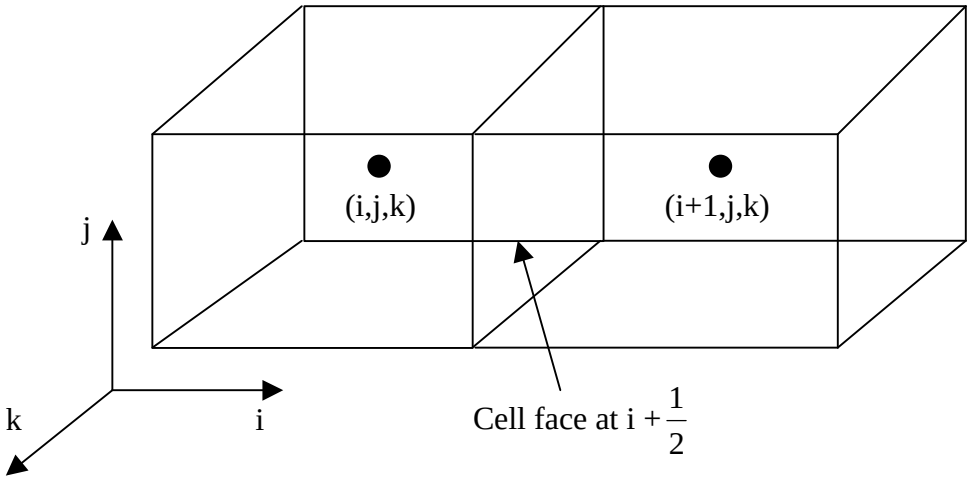

Figure 3.1 Control volume and cell-vertex grid points.

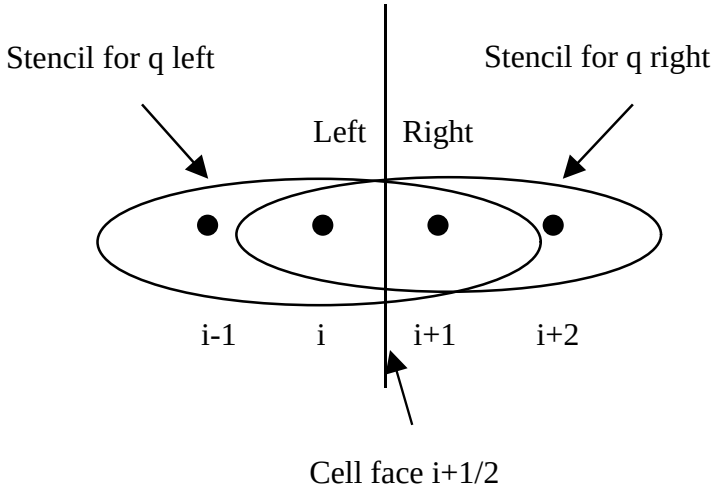

Figure 3.2 Computation of inviscid flux terms on a cell face.

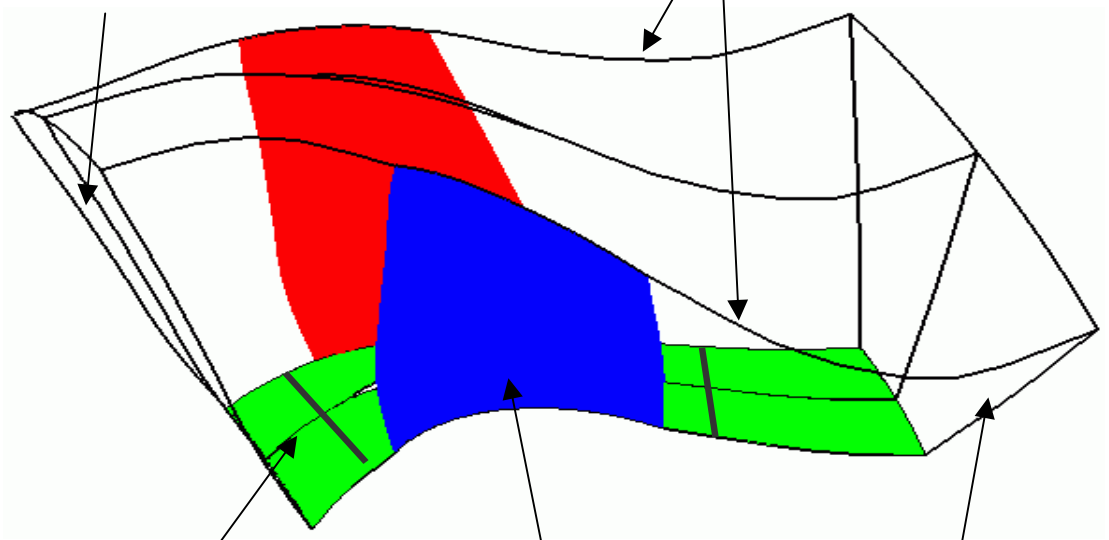

Figure 3.3 Boundary conditions used in the axial compressor analysis.

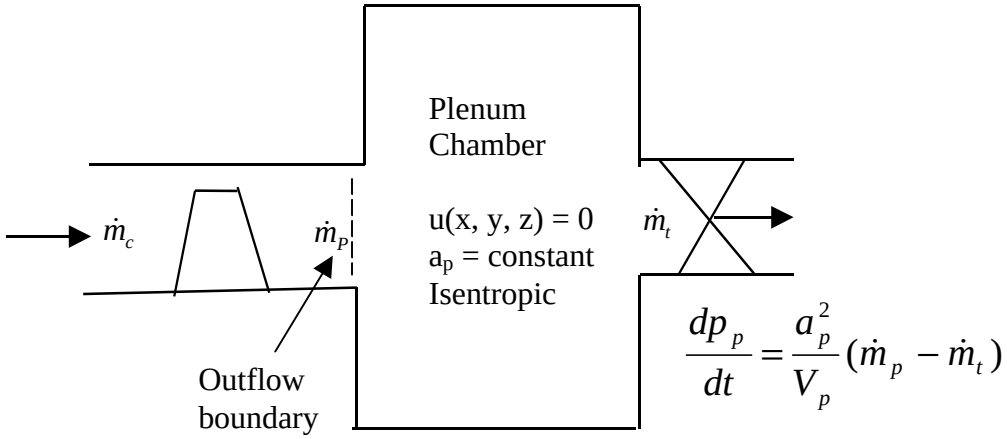

Figure 3.4 Compressor outflow boundary conditions.

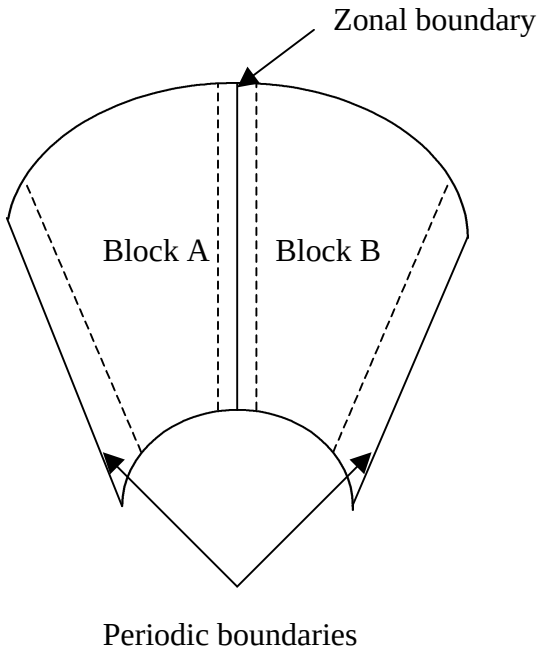

Figure 3.5 Periodic and zonal boundary conditions.

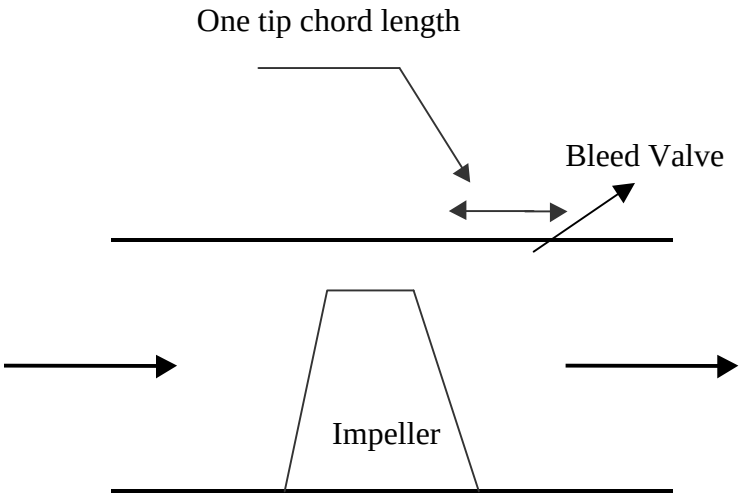

Figure 3.6 Implementation of bleeding as an open-loop active control.

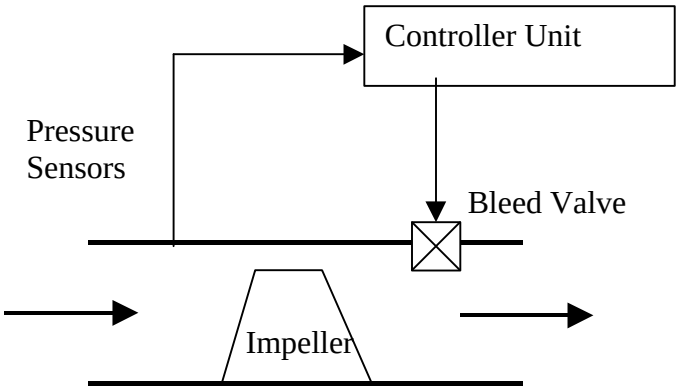

Figure 3.7 Implementation of bleeding as a closed-loop active control.

CHAPTER IV

CODE VALIDATION STUDIES

The numerical scheme and boundary procedures described in Chapter III were coded in a computational flow solver, called GT-TURBO3D. Results are presented in the following three chapters. The solver first reads a main input data file. This main input file controls the flow type (inviscid, laminar, turbulent), and the total number of time steps. It also specifies the computational grid size and the number of grid blocks, to perform the necessary initialization. It also reads nominal mass flow rate, $\dot{m}_t$. Next, the code reads the boundary condition setup data file to establish the appropriate boundary conditions described in Section 3.4 on the different faces of each of the blocks. The solver and the boundary conditions have been written in a general form so that most multi-block, patched grid analyses can be performed with this code.

Most calculations were carried out on a Silicon Graphics Origin 2000 system using two of the four available processors. Although the present implicit scheme can use large time steps, the CFL numbers was kept at or below 2 in order to resolve the unsteady flow in a time accurate manner. The calculations were generally run for several compressor revolutions, before a steady state or a limit cycle oscillation (indicative of separation and/or stall) was achieved. CPU time per time step was 3×10^{-5} sec per grid point. The

mass flow rate across several streamwise planes was monitored and used as a convergence criterion.

This chapter is organized as follows. The two axial compressor rotors used in this study are introduced in Section 4.1. In this section, geometry configurations and computational grids are described as well as their design operating characteristics. A brief literature survey of work done by other researchers on these two configurations is presented in Section 4.2. In Section 4.3, comparisons of the experimental data with the CFD results are given in the form of contour plots, graphs, and velocity vectors at the peak efficiency. Some grid sensitivity studies are also given.

4.1 DESCRIPTION OF THE CONFIGURATIONS STUDIED

Two different configurations have been chosen to study the compressor stall and passive/active control methodologies. These configurations are the NASA Rotor 67 and NASA Rotor 37 axial compressors. In this section, the configurations and the computational grids are presented.

4.1.1 NASA TRANSONIC AXIAL FAN ROTOR (ROTOR 67)

The first geometry chosen to validate the code and simulate compressor stall control was a transonic high-speed axial fan rotor, called NASA Rotor 67, shown in Figure 4.1.

This low aspect ratio rotor (σ=1.56) is the first stage rotor of a two stage transonic fan designed and tested with laser anemometer measurements at the NASA Glenn Research Center. The design pressure ratio is 1.63, at a mass flow rate of 33.25 kg/sec.

The rotor has 22 blades with tip radii of 25.7 cm and 24.25 cm at the leading and trailing edge, respectively. The hub/tip radius ratio is 0.375 at the leading edge and 0.478 at the trailing edge. The design rotational speed is 16043 RPM, and the tip leading edge speed is 429 m/sec with a tip relative Mach number 1.38. To determine the rotor mass flow rate, a calibrated orifice was used. A detailed description of blade and flow-path geometry, as well as measured data on total pressure, temperature, static pressure and flow angle data, may be found in Reference [82]. Figure 4.2 shows the locations where velocities were measured for this compressor. The hub consists of two stationary and one rotational segments. The rotor hub is in the region of $-3.533 \text{ cm} < x < 7.106 \text{ cm}$ and rotational wall conditions were applied to this region.

In order to model the rotating stall, multiple flow passage should be considered. For this purpose, a H-H-type grid, shown in Figure 4.3, with four compressor flow passages was generated using the "Gridgen" meshing package. The grid was generated by loading the geometry surface data from Reference [82] into the mesh package. In each flow passage, the grid, called the baseline grid, has 32 and 21 cells in the radial and circumferential directions, respectively. Sixty-six cells were placed in the streamwise direction, of which 33 were located over the blade chord. A hyperbolic tangent node point distribution near the surfaces was used to provide adequate resolution of the boundary layers. The clearance gap was spanned by three cells in the radial direction.

The grid at the mid-span and the grid normal to the streamwise direction are shown in Figures 4.4 and 4.5. Figure 4.6 shows the grids in the r-x plane, known as the

meridional plane. In this study, results in the form of vectors or contour plots are presented on one of these planes. This is because three-dimensional visualizations of flowfield in compressors are difficult due to configuration complexity, e.g. twisted blades. Grid sensitivity studies were also performed to ensure that the baseline grid has adequate resolution to resolve the leakage flow around the tip, the solid wall boundary layers and the shock system. Simulations were also done on another grid with twice the number of grid points in each of the three directions (4x131x63x41). Results for this configuration are discussed in Section 4.3 of this chapter and the next two chapters.

4.1.2 NASA TRANSONIC AXIAL FAN ROTOR (ROTOR 37)

The second configuration of interest was a high-speed axial flow compressor, called NASA Rotor 37. Rotor 37 is a NASA stage 37 rotor designed at the NASA Lewis Research Center as a test compressor for a high-pressure ratio (20:1) compressor core of an aircraft engine. The rotor design pressure ratio is 2.106 at a mass flow rate of 20.2 kg/sec. The rotor has a constant meanline diameter with a hub/tip radius ratio of 0.7. The design rotational speed is 17188 RPM, producing a speed of 454.19 m/sec at the inlet tip. The tip relative Mach number is 1.48. The clearance at the design is 0.36 mm. Details of this compressor may be found in references [83] and [84].

Figure 4.7 shows the Rotor 37 configuration. Figure 4.8 shows a meridional view of this rotor and the locations of laser anemometers at different stations. For this rotor, as for Rotor 67, some part of the hub is rotating. At the hub, stationary wall boundary

conditions were applied in the region x < -0.264 cm and x > 4.521 cm, while rotational boundary conditions were applied in the region –0.264 cm < x < 4.521 cm.

The grid for NASA Rotor 37 was generated with the same methodology that was used for NASA Rotor 67. The grid is a H-H-type with four flow passages, shown in Figure 4.9. It has 119x71x41 grid points in each flow passage in the streamwise, spanwise and pitchwise directions, respectively. Nine points were placed in the clearance gap. As in the case of NASA Rotor 67, the tip clearance gap was modeled and periodic boundary conditions were applied. Results for this configuration are given in Section 4.4.

4.2 PREVIOUSLY REPORTED STUDIES ON ROTOR 67 AND ROTOR 37 CONFIGURATIONS

Rotor 67 is an AGARD test case and is suitable for CFD validation purposes. Several researches have studied flowfields within this compressor. Studies conducted in the stable part of the design speed operating line for Rotor 67 may be found in References [85]-[92].

Effects of tip clearance gap on the flowfield have also been investigated by Adamczyk et al.[85] and Chima[86]. Chima obtained the results for two different tip clearance gap sizes, full and half, with an accurate modeling of the clearance gap. Effects of shock boundary layer interaction and wake development are reported by Hah et al[91]. End-wall and casing treatment for Rotor 67 may be found in Reference [92].

Rotor 37 was used to assess the prediction capabilities of turbomachinery CFD tools in a blind test organized by the 1994 ASME/IGTI workshop. In the CFD assessment, the

Rotor 37 was tested in isolation by Suder et al.[93]. Several researchers computed the complex flow field for this rotor for the stable branch of the performance map. These results may be found in References [90], [94] and [95]. Bright et al[96] have studied the dynamics for the Stage 37 during rotating stall.

4.3 PEAK EFFICIENCY RESULTS FOR ROTOR 67

The viscous flow solver, described earlier, has been validated for Rotor 67 and Rotor 37 compressor configurations. The flow solver had previously been used by this author to simulate the flowfield in a low speed centrifugal compressor, called the NASA Low Speed Centrifugal Compressor (LSCC, built and tested at NASA Glenn Research Center). The results for the centrifugal compressor, including the comparison of CFD predictions and experimental measurements such as blade pressure distributions, may be found in References [66]-[67]. High-speed centrifugal compressors have also been studied using this flow solver and computational-experimental comparison results can be found in References [68] and [70]. Because the predominant thrust of the present study is to model axial compressors, the LSCC validation results are not presented here.

In the present study, the flow solver was first applied to the simulation of flow through the NASA Rotor 67 compressor at peak efficiency conditions, for which experimental results may be found in Reference [82]. In this section, CFD results for both the baseline grid and the fine grid are presented and compared with the experimental data.

At the start of calculations, no restart solution files exist. Therefore, as pointed out in Section 3.4.1, the flow properties in the computational domain were assumed to be uniform and were set to their inlet freestream values. As the flowfield was advanced in time, the pressure at the inlet drops relative to the outflow. The drop in pressure depends on the compressor speed. Since NASA Rotor 67 is a high-speed compressor at its design speed, the pressure drop, especially in the blade suction side near the leading edge, is large and can produce non-physical pressure in that region. A start-up technique similar to that in a real compressor during acceleration was used to avoid this problem. The flow solver was applied to the rotor at three different speed levels: 30%, 50% and 100% of the design speed. The steady solution at each time level was used as a restart solution file for the next speed level. By this methodology, the pressure was allowed to drop in the suction side of the blades gradually and a steady state solution was achieved. A useful byproduct is performance data at off-design engine speeds.

At each time step, mass flow rates across the streamwise planes were calculated and averaged along the streamwise direction from the rotor leading edge to the rotor trailing edge. The averaged mass flow rate was considered as the mass flow rate through the rotor and was used as a convergence criterion. To calculate the total pressure ratio, the radial distributions of total stagnation pressure were mass averaged across the annulus. The formula used was:

$$\frac{\bar{p}_{02}}{\bar{p}_{01}} = \frac{\iint \frac{p_{02}}{p_{01}} \rho V dA}{\iint \rho V dA} \qquad \textbf{(4-1)}$$

Here, P_{02} and P_{01} are the stagnation pressure at station 2 and station 1, shown in Figure 4.2.

In this study 20 time steps per degree of revolution were used. Therefore, one rotor revolution required about 7000 computational time steps. For the baseline grid, the time required to perform one compressor revolution (where blades rotate 360°) was between 9 and 12 hours, using either one or two processors of the Origin 2000. In the fine grid, the running time was increased to 65 hours for one rotor revolution. Figures 4.10 and 4.11 show the fluctuations of mass flow rate and total pressure ratio. The computed mean mass flow rate was 34.23 kg/sec on the baseline grid, and the corresponding measurement data is 34.61 kg/sec (1.2% difference). The mass flow rate on the fine grid was identical to that on the baseline grid, up to 3 significant digits. These figures show that the mass flow and total pressure fluctuations at this operating condition are very small (less than 1%).

Figure 4.12 shows a comparison between the CFD predictions and the measured normalized axial velocity distribution at the inlet survey station 1 (Figure 4.2). The velocity is normalized by critical velocity at standard day conditions, V_{STD} =310.63 m/sec. CFD results are given for both fine and baseline grids. The computed axial velocity showed only a slight difference between the fine grid and the baseline grid.

Good agreement between the measurements and the predictions was obtained. It is also seen that the grids have enough resolution to capture the boundary layer profiles near the walls (hub and shroud).

The flow pattern inside a transonic fan like the NASA Rotor 67 is very complicated due to phenomena such as a 3-D shock system, shock-boundary layer interaction, clearance flow and three-dimensional separation. Figures 4.13 through 4.15 show comparisons between the computed and measured relative Mach number at two different span locations. Figure 4.13 shows the relative Mach number contours at the 30% span location, measured from the hub. The corresponding experimental contours were obtained from Reference [87]. There are several reasons the experimental data do not usually produce good quality contour maps. Background noise, problems associated with laser anemometer blade flash and data drop-out, non-uniform survey spacing, and inadequate measurement locations in viscous regions and the boundary layer and wake all produce poor quality plots. The experimental contours in Figure 4.13 were produced by Pierzga et al.[87], who smoothed and interpolated the measurements to fill the zero velocity data using information from the adjacent survey points in both the streamwise and pitchwise directions. The smoothing and interpolation procedures may be found in Reference [87]. The inlet mach number is 0.95 and the flow exits at a Mach number of about 0.60. As in experimental results, the CFD calculations showed that most of the flow at this span location is subsonic. However, small regions of supersonic flow, with relative Mach numbers about 1.05 were observed on the forward position of the suction

surface of the blades. The computed results in Figure 4.13 show shear layers over the blade and in the wake. These are not visible in the experimental contour plots. As mentioned earlier, this may be due to the lack of adequate measurement locations in the viscous regions.

Figures 4.14 and 4.15 show the measured and computed relative Mach number at 90% span at two different azimuthal locations. The horizontal axes were normalized by the chord at the corresponding span locations. Zero percent and 100% chord on these plots represent the blade leading and trailing edge, respectively. The comparisons generally agree well and a shock structure was observed. The computed relative Mach number showed a maximum difference of five percent between the baseline grid and fine grid.

The static pressure contours and the shock locations in the four flow passages at two different radial locations, 30% and 70% span, are illustrated in Figure 4.16. This figure demonstrates how the pressure through the compressor builds up. At both these radial locations, the pressure drops on the blades suction surfaces as a consequence of flow acceleration, in the same way an airfoil behaves. At 70% span, the pressure gradient is much higher than at 30% span, and a bow shock occurs. All of the four flow passages showed identical pressure distributions, indicating the flowfield is identical and well converged in all blade passages.

Figure 4.17 shows the relative velocity profile at mid-span on three blade passages, viewed from the top of the rotor. It is seen that the shock nearly covers the gap between

the blades, suggesting choke conditions are imminent. Velocity profiles are well behaved in the blade passages with no evidence of reversed flow. Flow properties and the velocity flowfield were almost identical from blade to blade. The relative velocity vectors on a plane normal to the rotor axial direction is given in Figure 4.18. This figure shows the cross flow and does not show any stall cells. Such a well-behaved flow is, of course, expected at the peak efficiency conditions.

To visualize the shock-boundary layer interaction, relative velocity vectors near the blade surfaces and inside the boundary layer are plotted in Figure 4.19 and 4.20. Near the suction side just after the shock, a very strong outward flow in the radial direction was observed, as shown in Figure 4.19. This outward flow pattern has also been reported in References [89] through [92]. The shock is very strong from the tip to 40% of the span and causes the boundary layer to separate immediately aft of the shock. Below 40% of span from the tip of the blade, as discussed by Hah[91], the outward flow is not directly due to the shock-boundary layer interaction, but is related to a conventional adverse pressure gradient. As pointed out by Chima[89], the flow is also strongly influenced by a vortex roll-up on the leading edge close to the blade root. Flow near the pressure side of the blades, shown in Figure 4.20, is more streamlined because no shock forms on this surface boundary layer. In these figures the results shown are on both fine and baseline grid. These figures and the preceding results showed that the baseline grid has enough resolution to capture all the important phenomena occurring in this compressor. Because of the large number of computations involved in surge and rotating

stall simulations, the baseline grid was used in simulations of off-design operating conditions, as well as in the passive and active bleed control calculations.

Figure 4.21 illustrates the meridional velocity profile at the peak efficiency at mid-passage. The overall flow field is well attached and behaved. Small regions of reversed flow between the blade tip and the shroud were observed in an enlarged view, shown in the same figure. This reversed flow and the leakage tip vortex play dominant roles in triggering surge and rotating stall, as discussed later.

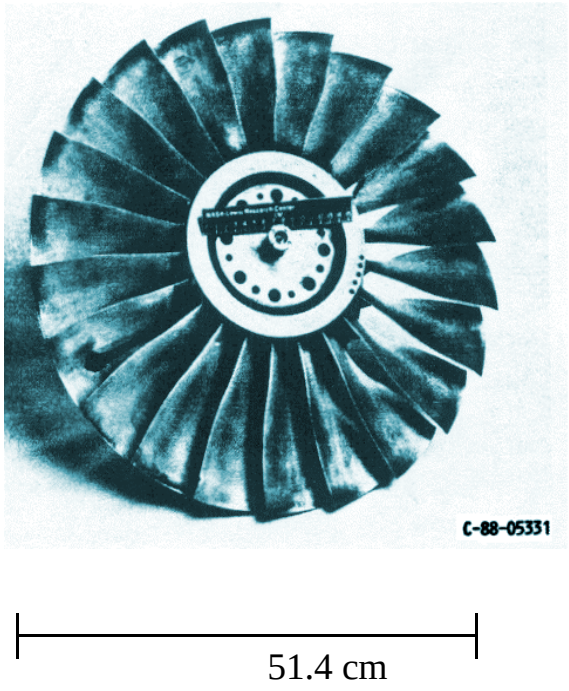

Figure 4.1 NASA Rotor 67 configuration, Reference [82].

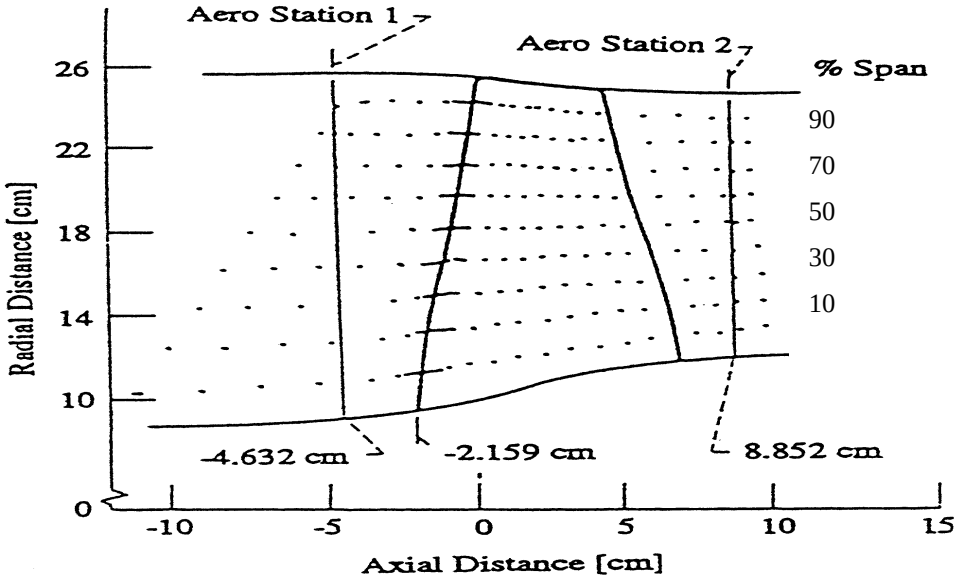

Figure 4.2 Laser anemometer and aerodynamic locations for Rotor 67, Reference [90].

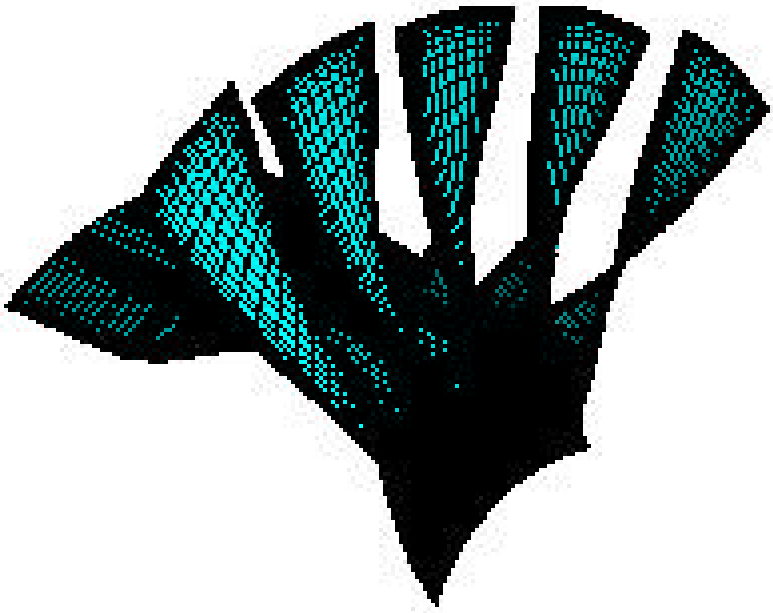

Figure 4.3 Computational grid for Rotor 67.

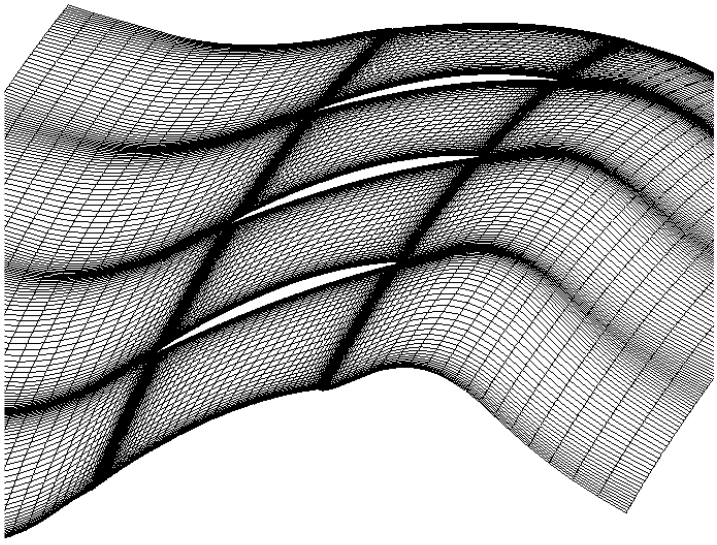

Figure 4.4 Streamwise computational grid at midspan for Rotor 67.

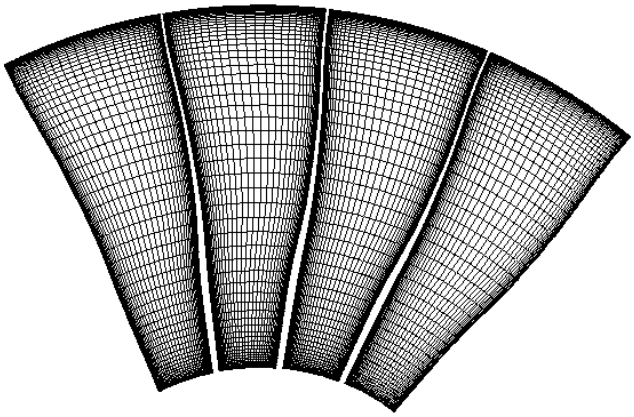

Figure 4.5 Pitchwise computational grid for Rotor 67.

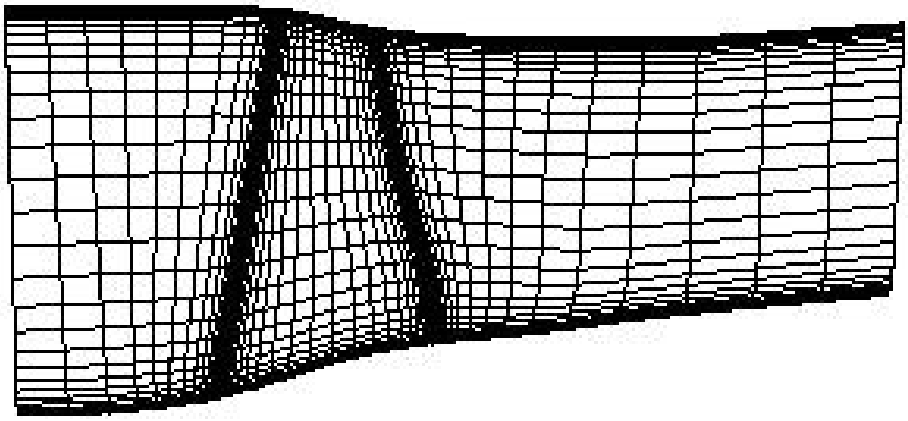

Figure 4.6 Computational grid in the meridional plane for Rotor 67.

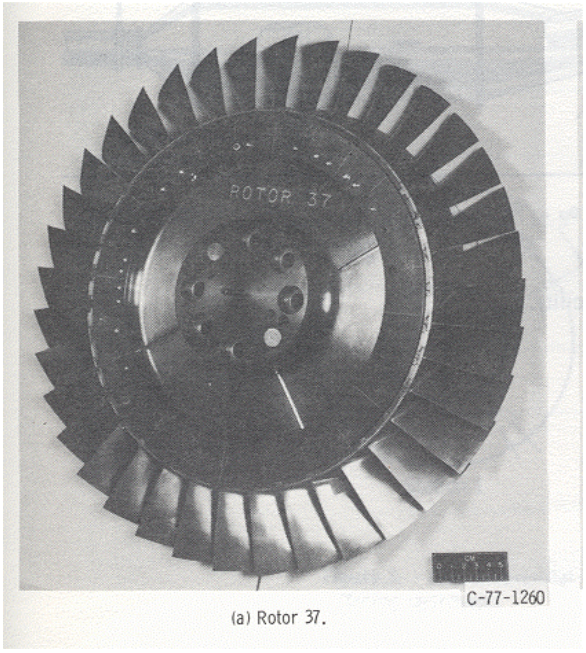

Figure 4.7 NASA Rotor 37 configuration, Reference [84].

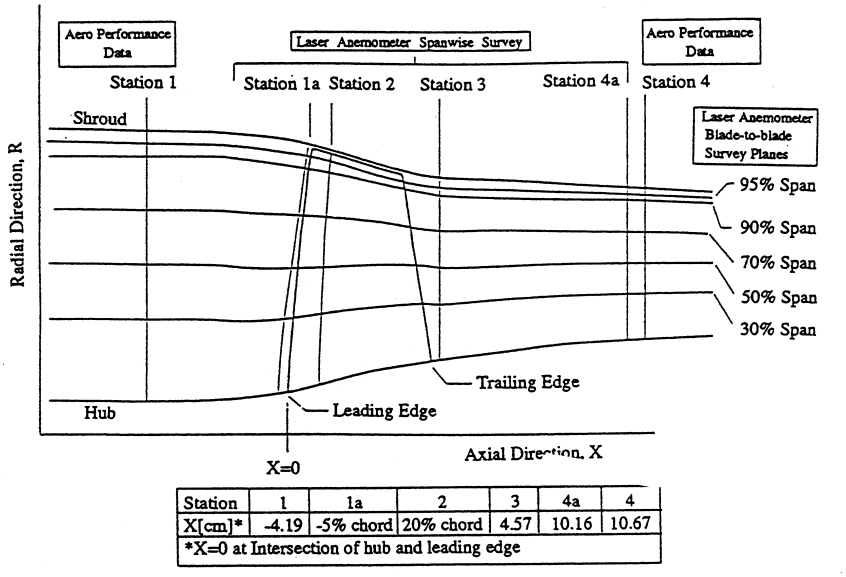

Station	1	1a	2	3	4a	4
X[cm]*	-4.19	-5% chord	20% chord	4.57	10.16	10.67
*X=0 at Intersection of hub and leading edge						

Figure 4.8 Laser anemometer and aerodynamic locations for Rotor 37, Reference [90].

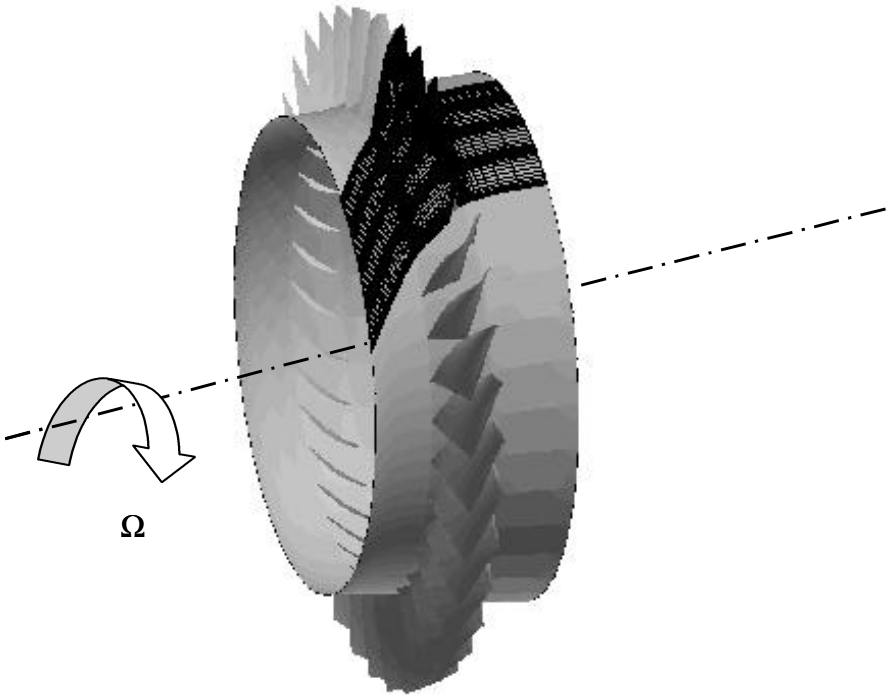

Figure 4.9 Computational grid for Rotor 37.

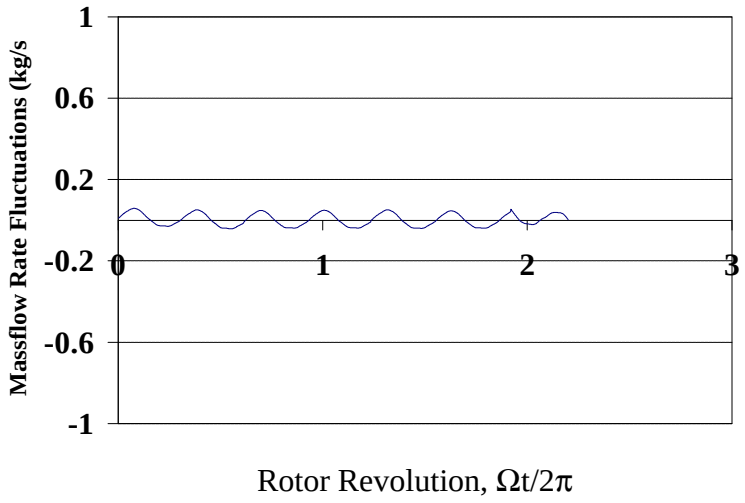

Figure 4.10 Time history of mass flow rate fluctuations about mean flow at peak efficiency conditions (Rotor 67).

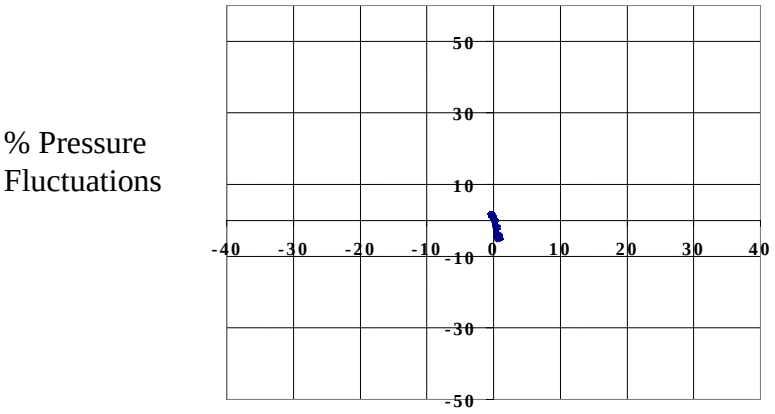

Figure 4.11 Pressure and mass flow rate fluctuations at peak efficiency conditions (Rotor 67).

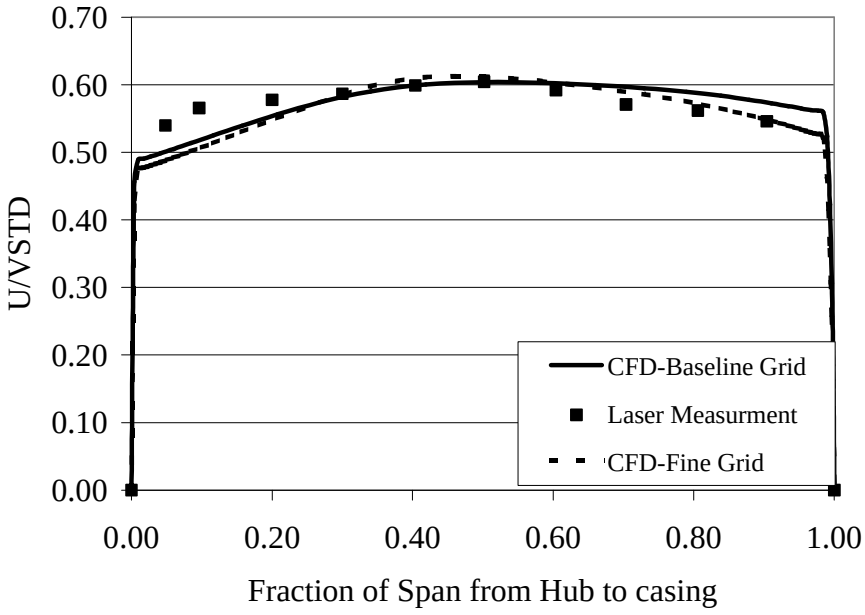

Figure 4.12 Comparison between experiments and present results of inlet axial velocity at peak efficiency conditions (Rotor 67).

Computed

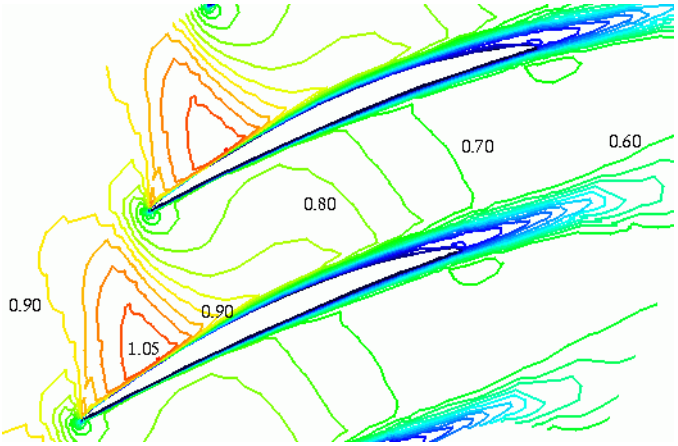

Measured
(Reference 87)

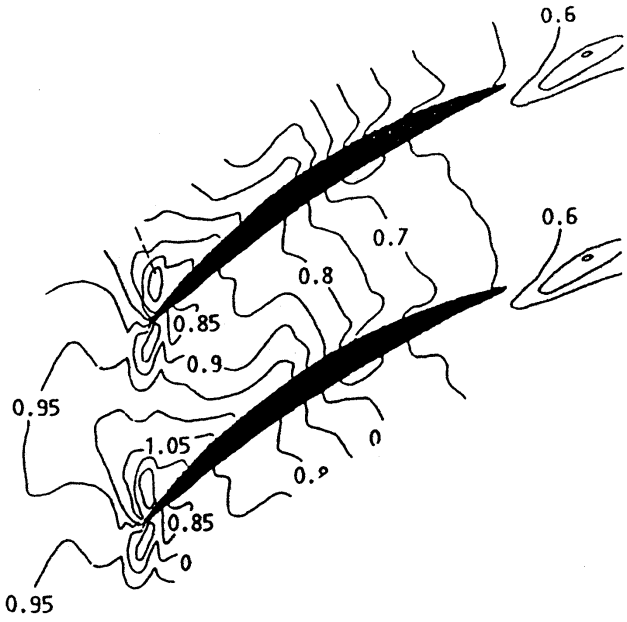

Figure 4.13 Comparison between experiments and present predictions of relative Mach number contours at 30% span at peak efficiency (Rotor 67).

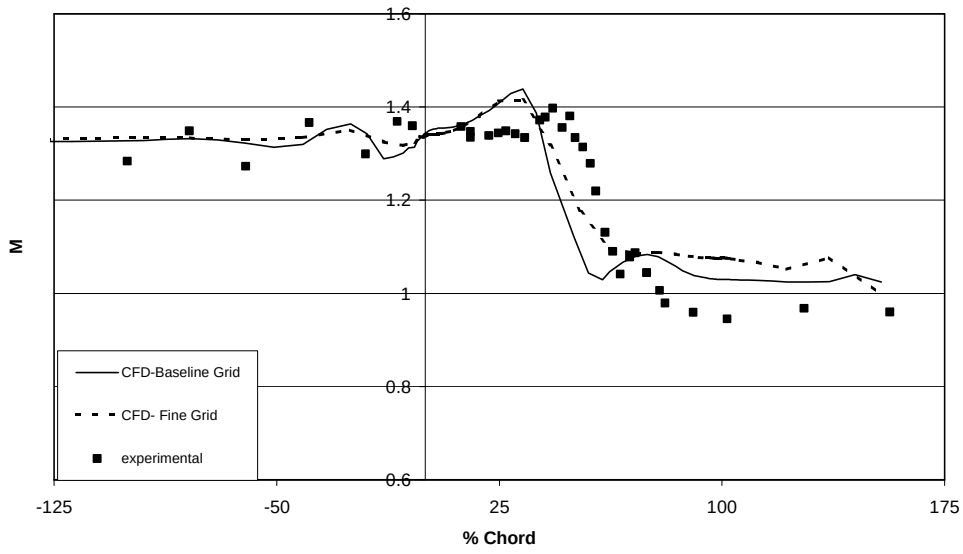

Figure 4.14 Comparison between experiments and present results of relative Mach number at 90% span and 30% pitch at peak efficiency (Rotor 67).

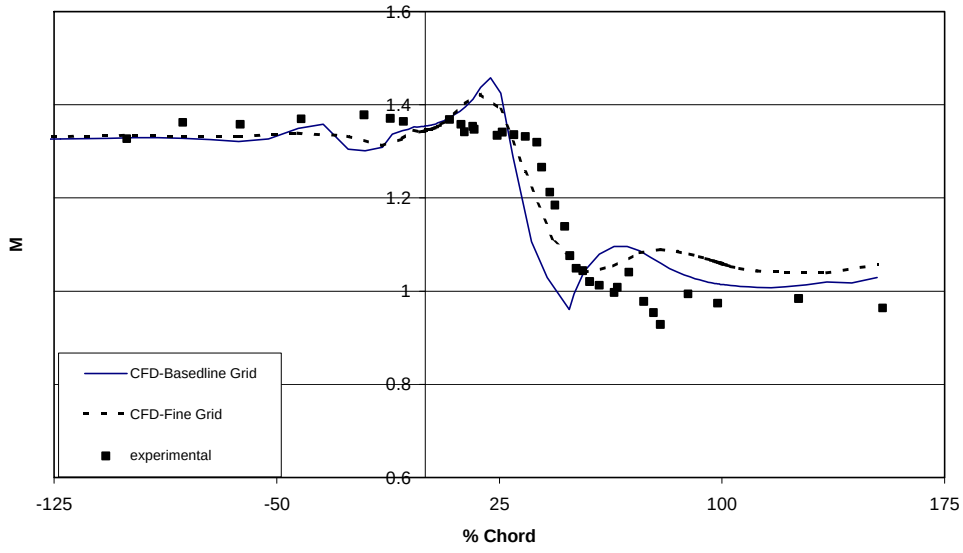

Figure 4.15 Comparison between experiments and present results of relative Mach number at 90% span and 50% pitch at peak efficiency (Rotor 67).

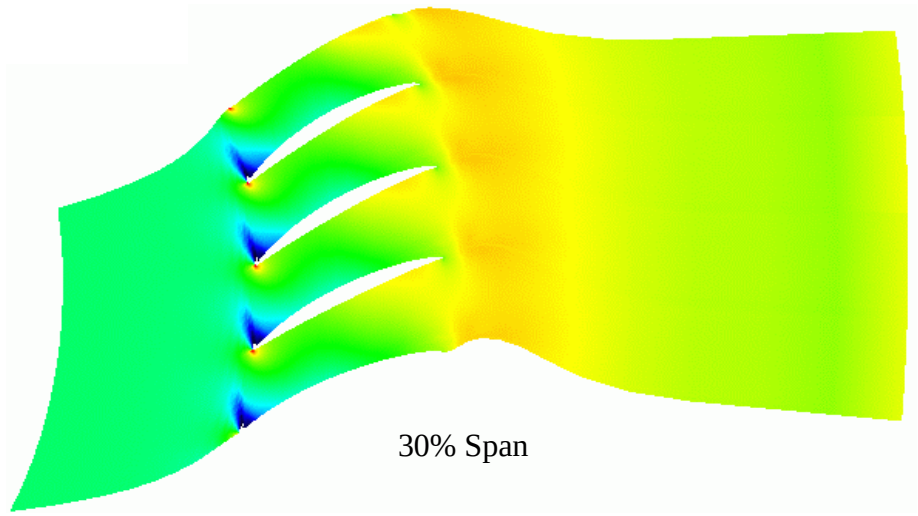

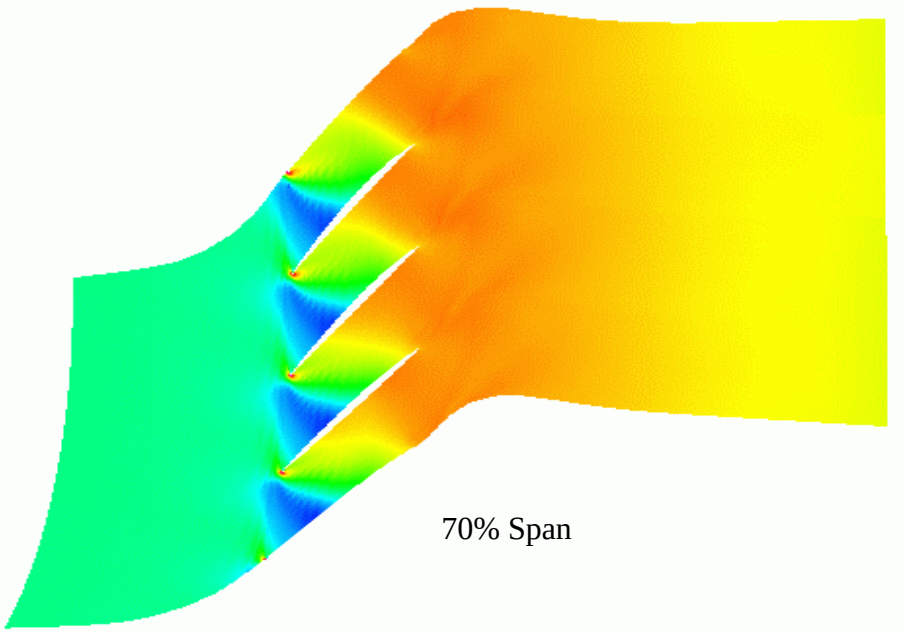

Figure 4.16 Static pressure contours at 30% and 70% span at peak efficiency (Rotor 67).

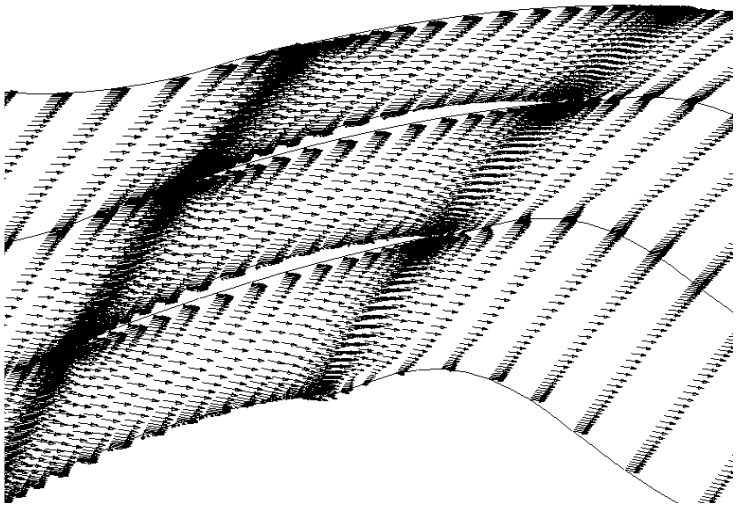

Figure 4.17 Relative velocity profile at mid-span at peak efficiency (Rotor 67).

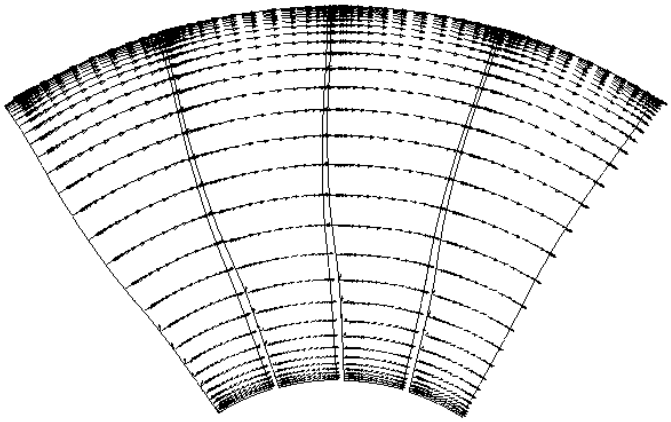

Figure 4.18 Secondary flow in the circumferential direction at peak efficiency (Rotor 67).

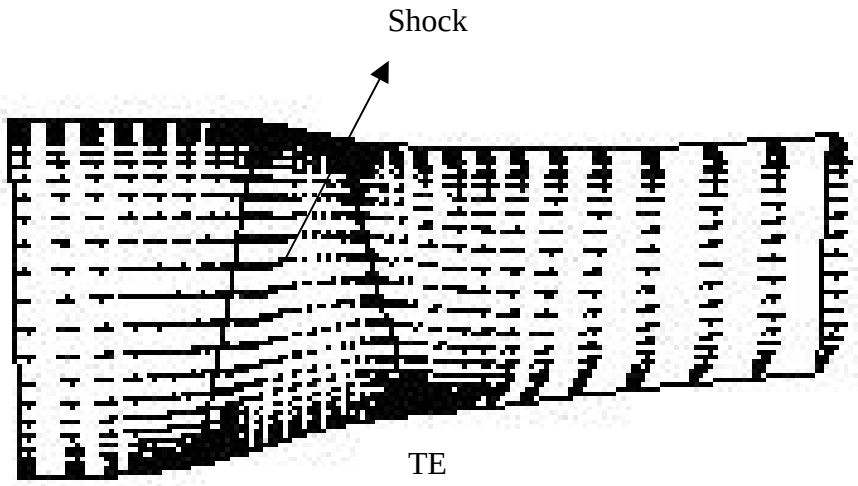

Baseline Grid

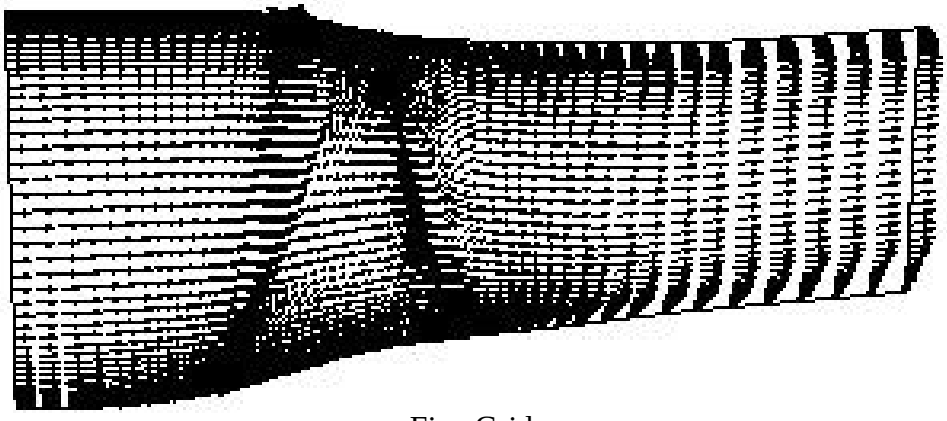

Fine Grid

Figure 4.19 Flow field near blade suction surface at peak efficiency (Rotor 67).

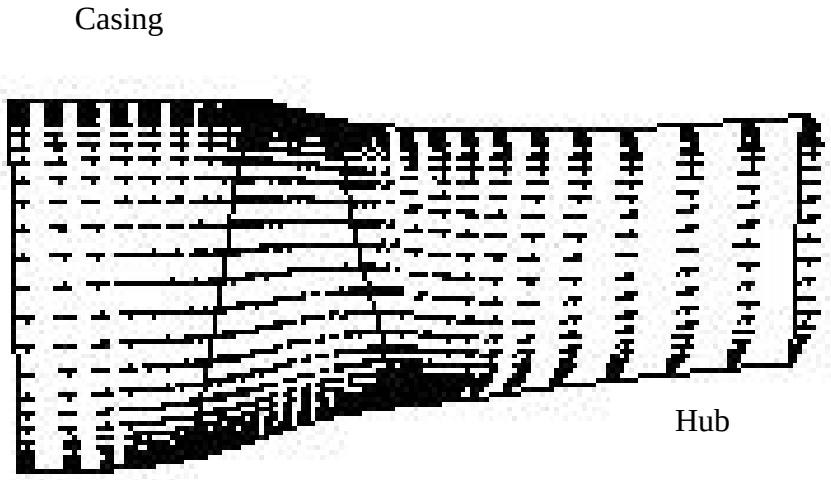

Baseline Grid

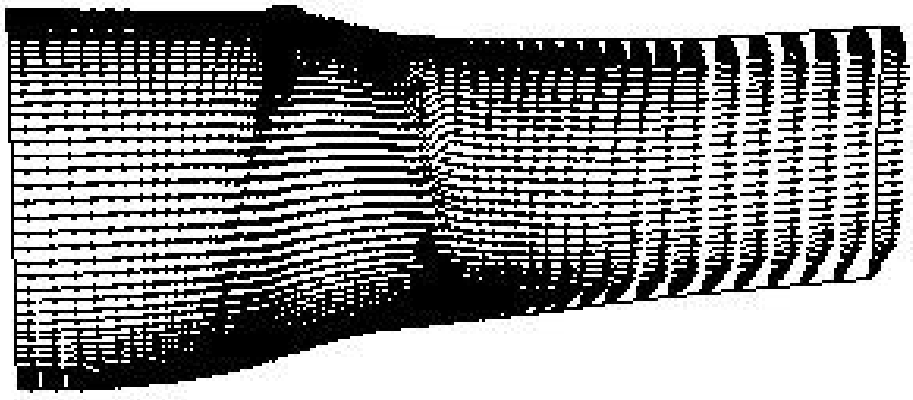

Fine Grid

Figure 4.20 Flow field near blade pressure surface at peak efficiency (Rotor 67).

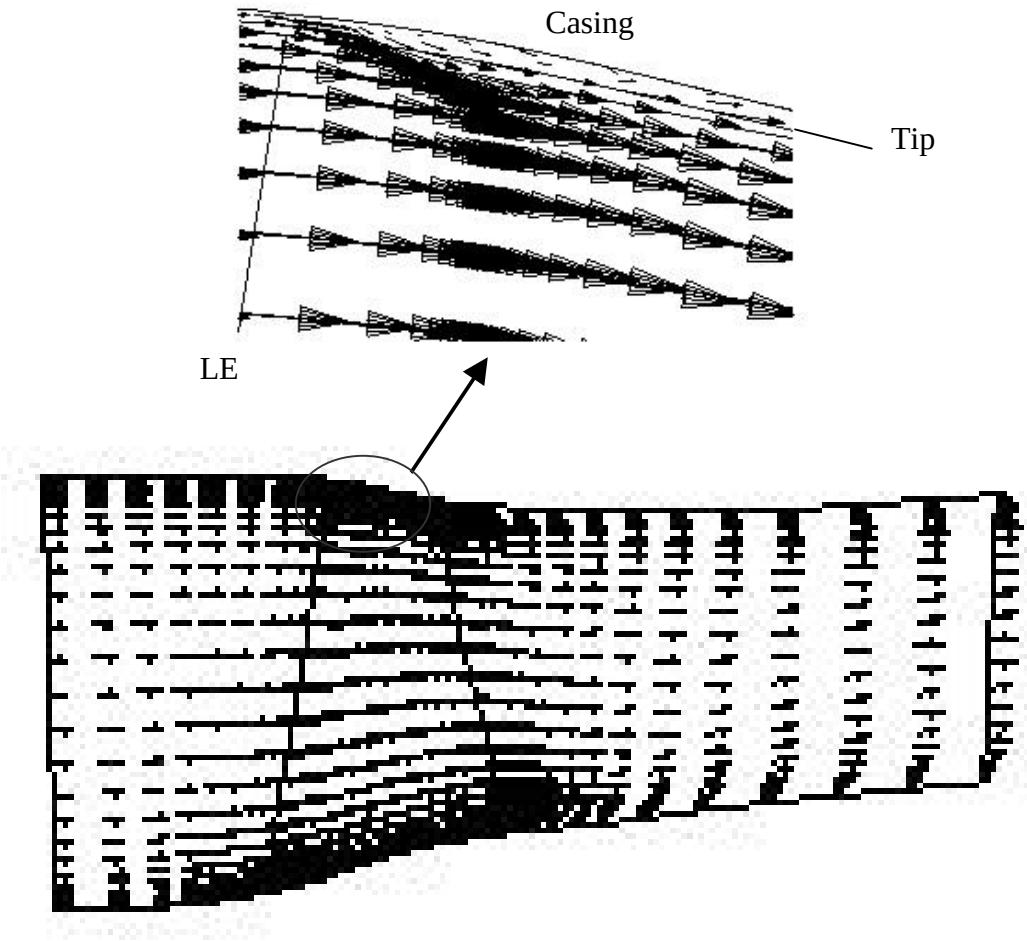

Figure 4.21 Flow field at mid-passage at peak efficiency (Rotor 67).

CHAPTER V

RESULTS AT OFF-DESIGN CONDITIONS

In the previous chapter, the stable operating, peak efficiency condition results for the compression system NASA Rotor 67 were discussed. It was shown that at this operating point, the mass flow and pressure fluctuations are very small. Furthermore, no azimuthal disturbances (stall cells) were observed and the flow was circumferentially uniform. However, as pointed out in Chapters I and II, as the mass flow rate through the compressor is decreased from this stable point to the surge line, disturbances grow and lead the system to unstable conditions. Investigation of the flowfield at off-design conditions is one of the goals of this study, and is documented in this chapter

In this chapter, the computational results for the two axial compressors introduced in Chapter IV, are presented at different operating conditions. Results include the characteristic performance maps, the time history of the flow at selected points on these curves, velocity vectors and pressure contour plots of the flowfield, and time traces of pressure upstream of the compressor face using computational probes located around the circumference of the compressor. Results for the Rotor 67 compressor are presented in Section 5.1. The calculations for the Rotor 37 are given in Section 5.2.

5.1 ROTOR 67 RESULTS

Results from CFD unsteady calculations for the compressor NASA Rotor 67 at two different operating conditions are discussed in this section. In Section 5.1.1, results at the onset of stall are presented. Stalled flow results are given in Section 5.1.2.

5.1.1 ONSET OF STALL

As mentioned earlier, the performance map of a compression system is the relation between the total to total pressure ratio and the compressor mass flow. In real life, the characteristic performance map of a compressor is obtained by changing the compressor mass flow rate using a throttle valve in the plenum.

In this study, the flow solver was applied to the NASA Rotor 67 for 10 different operating conditions to construct the overall rotor performance map. The backpressure is calculated from Equation (3-56) with a user specified mass flow rate at the plenum exit. From the pressure difference between the compressor inlet and diffuser exit, the mass flow rate through the compressor can be computed, and the operating point obtained. The radial distributions of total temperature and stagnation pressure are mass averaged across the annulus.

The calculated total pressure ratios at full speed are plotted against the normalized mass flow and compared to experimental data in Figure 5.1. Both calculated and experimental data are nondimensionalized by their corresponding choked mass flow rate. This kind of normalization removes uncertainties in the experimental mass flow rates. The reported choked mass flow rate for the NASA Rotor 67 is 34.96 kg/sec and the

calculated value is 34.72 kg/sec (0.7% difference). It is seen that the performance map agrees well with the experimental data. Three points, A, B and C, indicated on the performance map, are the operating points where the detailed flowfield was studied. Point A in Figure 5.1 is related to the peak efficiency condition, and its corresponding results were studied in the previous chapter. Here, the CFD calculations for the other two points, B and C, are discussed.

The adiabatic efficiency of a compressor is the ratio of the ideal input work needed to raise the total pressure of a working fluid from a pressure value P_{01} to a new value P_{02}, to the actual work needed to accomplish this task. The adiabatic efficiency of the compressor can be found by using:

$$h_{ad} = \frac{W_s}{W_a} \qquad \textbf{(5-1)}$$

where W_s and W_a are the isentropic and actual work done on the flow, respectively. These can be found as follows:

$$\begin{aligned} W_s &= \dot{m} c_p (\overline{T}_{02|_s} - \overline{T}_{01}) \\ W_a &= \dot{m} c_p (\overline{T}_{02} - \overline{T}_{01}) \end{aligned} \qquad \textbf{(5-2)}$$

Applying isentropic relationship for point 1 and 2:

$$\frac{\overline{T}_{02}}{\overline{T}_{01}}\Big|_s = \left(\frac{\overline{p}_{02}}{\overline{p}_{01}}\right)^{\frac{g-1}{g}} \tag{5-3}$$

and using Equations (5-1) to (5-3), we get :

$$h_{ad} = \frac{\left(\frac{\overline{p}_{02}}{\overline{p}_{01}}\right)^{\frac{g-1}{g}} - 1}{\frac{\overline{T}_{02}}{\overline{T}_{01}} - 1} \tag{5-4}$$

The radial distributions of total temperature and stagnation pressure are mass averaged across the annulus and are obtained from Equation (4-1) and the following equation:

$$\frac{\overline{T}_{02}}{\overline{T}_{01}} = \frac{\oiint \frac{T_{02}}{T_{01}} rVdA}{\oiint rVdA} \tag{5-5}$$

Figure 5.2 shows the comparison of measured and computed adiabatic efficiency for different operating conditions. The predicted peak efficiency occurs at a slightly higher mass flow rate as compared to the experimental results.

Stall inception in compressor experimental studies is normally detected by hot-wire probes placed in a stationary frame around the circumference of the compressor. In the present study, four "numerical" probes were circumferentially located in a stationary system 30% of the tip chord upstream of the rotor blade row, as shown in Figure 5.3. The probes were placed in the mid-pitch of each of the flow passages and at 90% of the span from the hub. At each computational time step the probes calculated the axial component of the flow velocity and the corresponding pressure.

Figures 5.4 shows the fluctuations of mass flow rate and total pressure ratio for operating point B on the compressor map in Figure 5.1. The computed mean mass flow rate was 31.6 kg/sec and the corresponding measurement data at the onset of stall is 92% of choked flow, or 32.1 kg/sec. (~1.6% difference). Compared to the mass flow and pressure fluctuations at point A in Figure 4.11, it can be seen that the fluctuations at this point increased by about 15%. The amplitude of the flow oscillations at point A was less than 1%.

The spatial average of static pressure from the probes upstream of the compressor face is shown in Figure 5.5. The averaged pressure fluctuated between 0.57 and 0.67 of the about value at the inlet face, 16% of its mean value. Figure 5.6 illustrates the deviations of the static pressure of each of the four probes from their azimuthally averaged values. For clarity, the time traces shown in Figure 5.6 are shifted vertically by a constant interval. All the probes showed same amount of deviation and are very close to zero, indicating the flow was periodic from blade to blade. In the other words, no

evidence of circumferential disturbances was observed, even though the amplitudes of the mass and total pressure fluctuations are about 15% and 10% of the mean values, respectively.

Figure 5.7 depicts the time traces of the spatial average of the axial velocity component upstream of the compressor face. The axial velocity fluctuations were small and there was no reversed flow for this operating condition.

5.1.2 ROTATING STALL AND MODIFIED SURGE SIMULATIONS

Decreasing the mass flow rate to 84.6% of the choked mass flow rate (29.4 kg/sec) causes the compressor to experience very large amplitude fluctuations of both mass flow rate and total pressure ratio. Figure 5.8 shows the time history of the mass flow rate for about 25 rotor revolutions. Limit cycle oscillations with a frequency of about $\frac{1}{70}$ blade passage frequency, equal to 84 Hz, was observed. The total pressure ratio fluctuation versus the mass flow fluctuation is illustrated in Figure 5.9. A comparison of Figures 5.9 and 5.4 indicates that as the mass flow rate through the compressor is decreased by six percent, from point B to point C in Figure 5.1, the amplitude of the total pressure ratio oscillation increases from 10% to 50%. Vector plots in meridional planes and pressure contour plots in circumferential planes were used to study the effects of these large flow fluctuations on the flowfield.

In Chapter IV, it was shown that at peak efficiency conditions, generally the flow was well aligned and just a small region of reversed flow in the clearance gap was

observed (see Figure 4.21). Figure 5.10 illustrates the growth of this reversed flow and flow separation at operating point C at three different time instances. These vector plots are shown in the meridional plane at the midpitch of one of the flow passages. The rapid growth of the tip leakage vortex over one and half rotor revolution causes some reversed flow in the inlet near the casing.

The static pressure contours in the circumferential plane upstream of the compressor face for operating conditions C are illustrated in Figure 5.11 at one instance in time. In this figure, darker regions represent low-pressure areas and the lightly shade regions correspond to high-pressure areas. It was observed that the low-pressure regions are moving in the opposite direction of the shaft rotation, in a rotating frame. The spatial averages of axial velocity and static pressure from the probes readings are shown in Figure 5.12. Three different levels of amplitude with high frequency fluctuations, indicated by sections I, II, and III, were observed in this figure. These levels can be called as recovery level, precursor level and stall level. The amplitude of fluctuations for both pressure and axial velocity in the recovery level, section I, were very small, about 3% of their average. After about one revolution, the amplitude of fluctuations increased to 20% (precursor level, section II), and lasted for approximately half of the rotor revolution. Finally the stall cycle leads to a very large fluctuations, 50%, in stall level (section III), for one compressor revolution.

A power spectral density analysis was performed to determine the dominant frequencies of the averaged static pressure fluctuations. The results are shown in Figure

5.13. This figure shows that the dominant frequency of these azimuthal disturbances is about 100 Hz, which is about 38% of the rotor frequency.

Figure 5.14 illustrates the deviation of axial velocity from the spatial averaged axial velocity (shown in Figure 5.12) for all of the four probes. As in Figure 5.6, the time traces shown in this figure are shifted vertically by a constant interval. It was observed that the probes experienced same axial velocity magnitude for about 1.5 rotor revolutions, followed by a different velocity magnitude in each probe for approximately another 1.5 revolutions. Figures 5.11 to 5.14 indicate that the flow is not symmetric from one blade passage to the next and a part span rotating stall occurs. From the above discussion, it is believed that the compressor at this operating condition, point C, is experiencing a three dimensional instability that is similar to a modified surge, which is a combination of rotating stall and surge.

5.2 ROTOR 37 SIMULATIONS

The second configuration, which was briefly studied, was the compressor NASA Rotor 37. As mentioned earlier, Bright et al.[96] at NASA Glenn Research Center have obtained surge and rotating stall data for this compressor. The experimental data are for the Stage 37, which includes Stator 37 and Rotor 37. In this study only Rotor 37 was simulated, and the effects of stator and rotor interaction were not evaluated. No one-to-one comparisons with the experimental measurements were attempted, due to date availability.

The flow solver was applied to the NASA Rotor 37 for seven different operating conditions. The same methodology used in Section 5.1.1 was applied to study compressor operation at 70% of design speed, which was about 12000 RPM. This RPM corresponds to the compressor RPM in the NASA test.

From these results, the compressor performance map was extracted and is shown in Figure 5.15. Good agreement between the computed results and measured data was observed.

The time history of the mass-flow rate and total pressure ratio at the selected points A, B and C, indicated on the performance map, are plotted in Figure 5.16. The mass flow rate for point A was 15.0 kg/sec, and at this operating point calculations showed very small fluctuations (~1%). At point B, the mass flow was 13.5 kg/sec and the mass flow fluctuations increased to 5% of the mean flow. The computed result for point C was about 12 kg/sec, with 15% fluctuations in the mass flow.

To investigate azimuthal disturbances, computational probes one tip chord upstream of the compressor face were used. Figure 5.17 shows the deviation of pressure magnitudes from the circumferentially averaged pressure. This figure indicates that the pressure disturbances were small compared to the 15% fluctuations in mass flow at this operating condition. Spectral power density for these azimuthal disturbances was plotted in Figure 5.18. This figure revealed that these disturbances had a very high content frequency (1-8 kHz) with small amplitudes. These high frequency small disturbances may be due to fine scale boundary layer phenomena. Figure 5.17 indicates that the

compressor experienced a one-dimensional disturbance, which may referred to as a mild surge. We call this a surge because the pressure fluctuations at all four probes are nearly identical, with no phase difference indicative of a rotating stall.

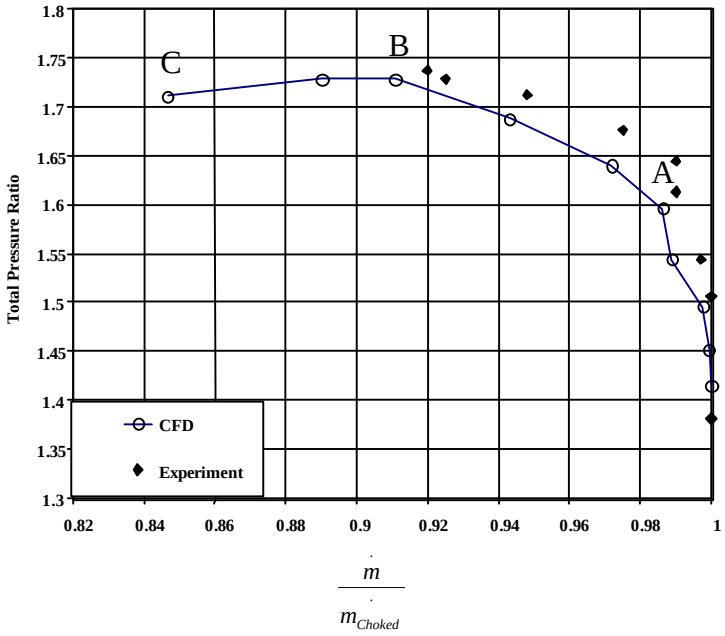

Figure 5.1 Comparison of measured and computed characteristic performance map (Rotor 67).

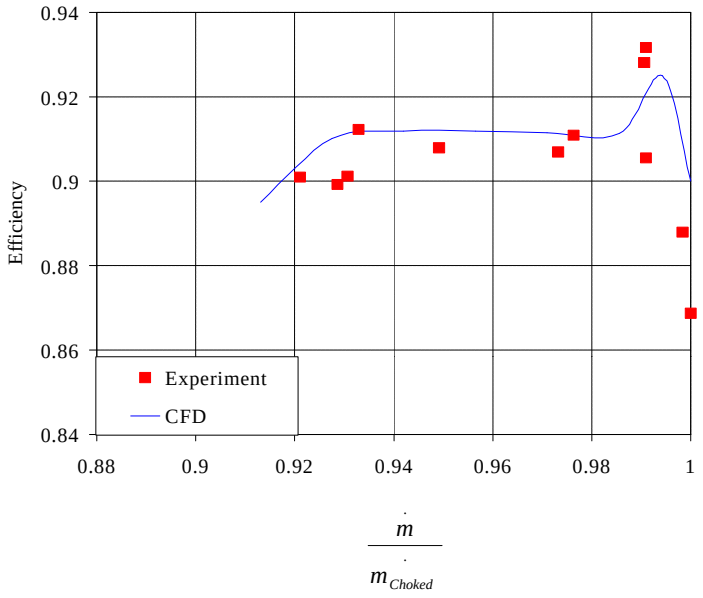

Figure 5.2 Comparison of measured and computed adiabatic efficiency (Rotor 67).

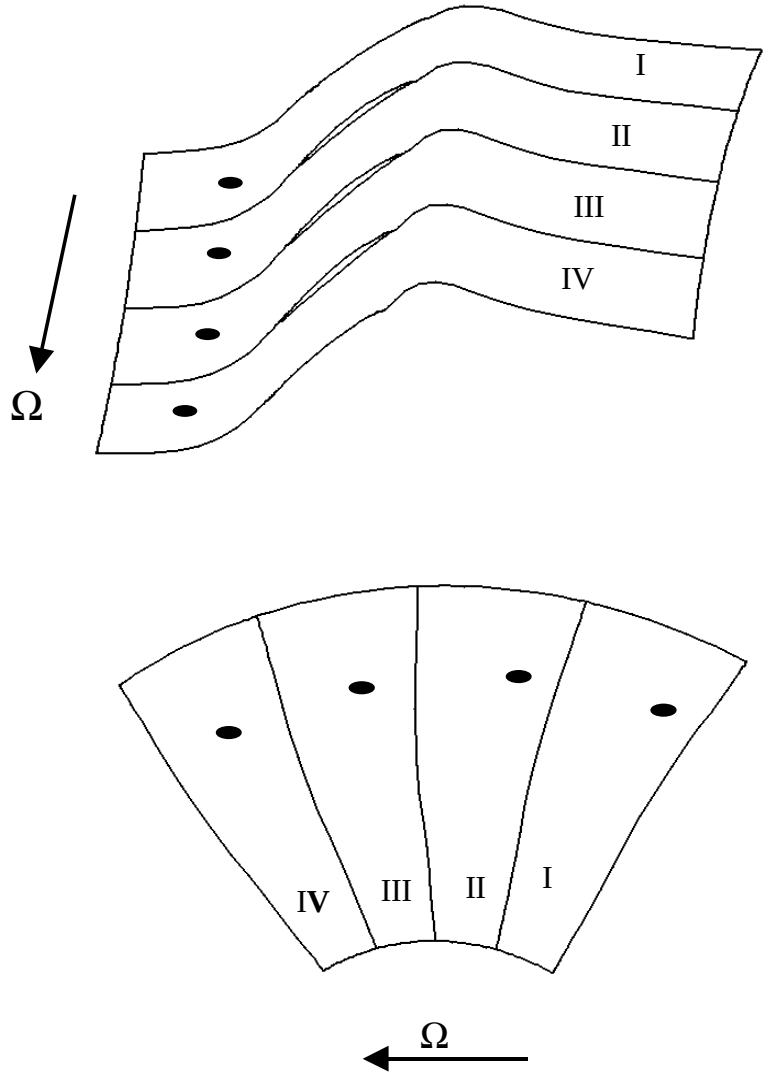

Figure 5.3 Locations of the computational probes (Rotor 67 and Rotor 37).

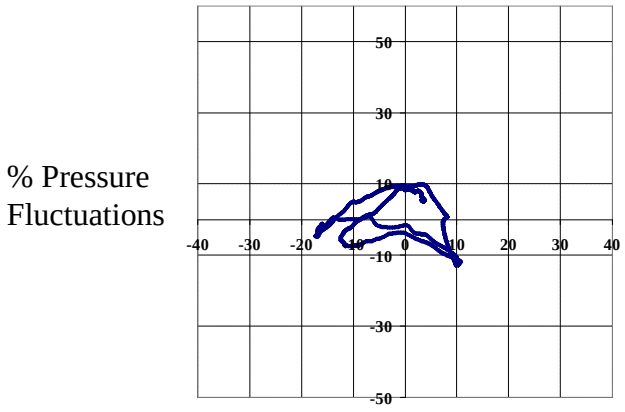

Figure 5.4 Pressure and mass flow rate fluctuations at the onset of stall, operating point B (Rotor 67).

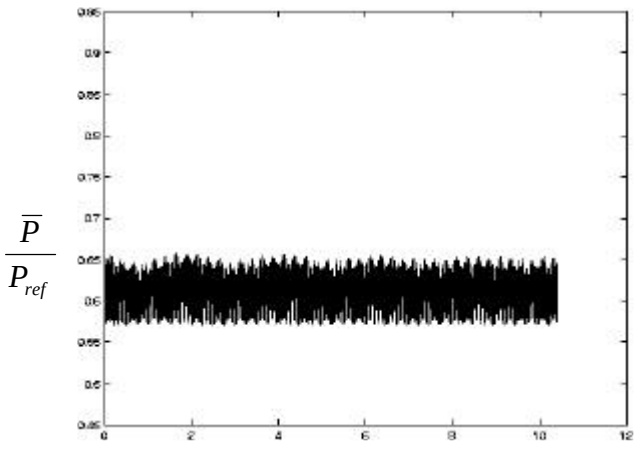

Figure 5.5 Time history of averaged pressure computed by probes upstream of the compressor face at operating point B (Rotor 67).

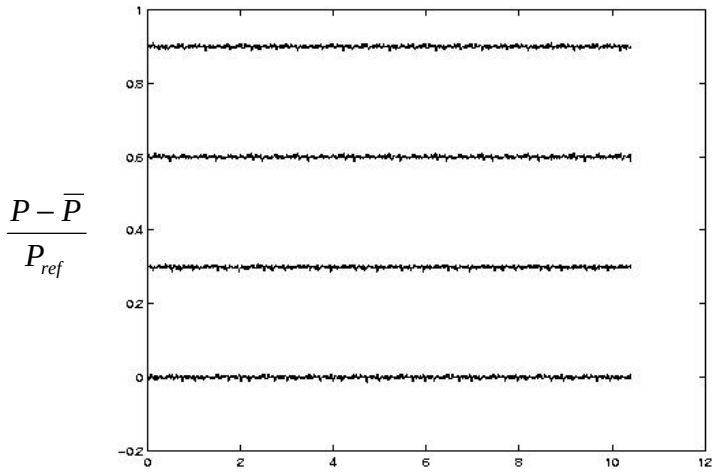

Figure 5.6 Time history of pressure deviation from its azimuthally averaged pressure upstream of the compressor face at operating point B (Rotor 67).

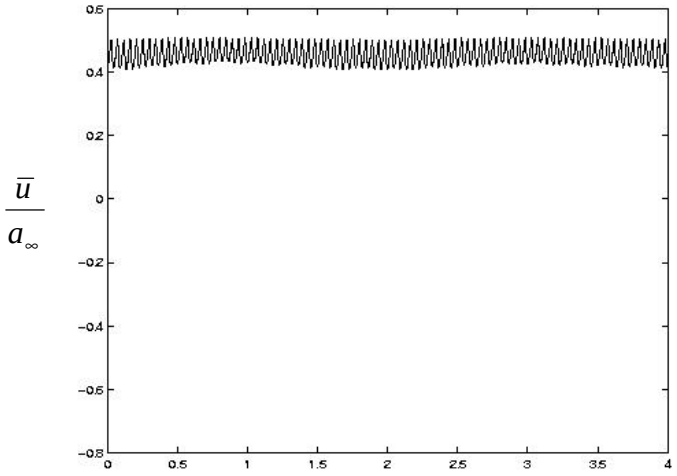

Figure 5.7 Time history of averaged axial velocity computed by probes upstream of the compressor face at operating point B (Rotor 67).

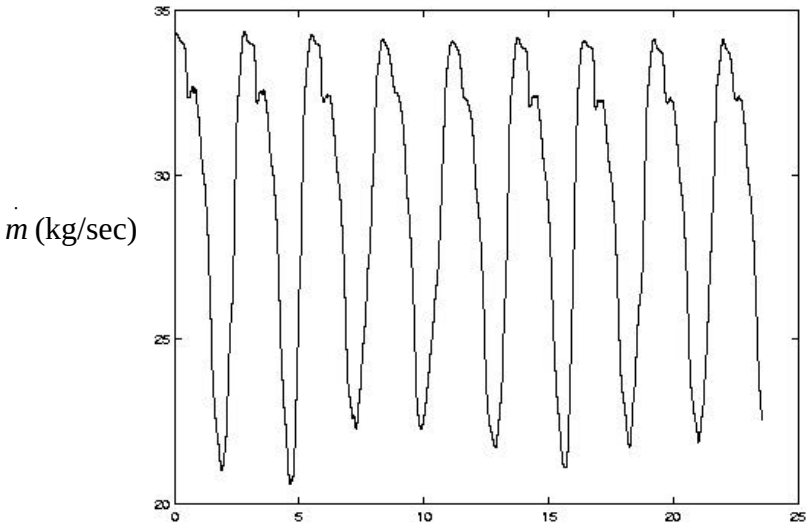

Figure 5.8 Time history of mass flow rate fluctuations at operating point C (Rotor 67).

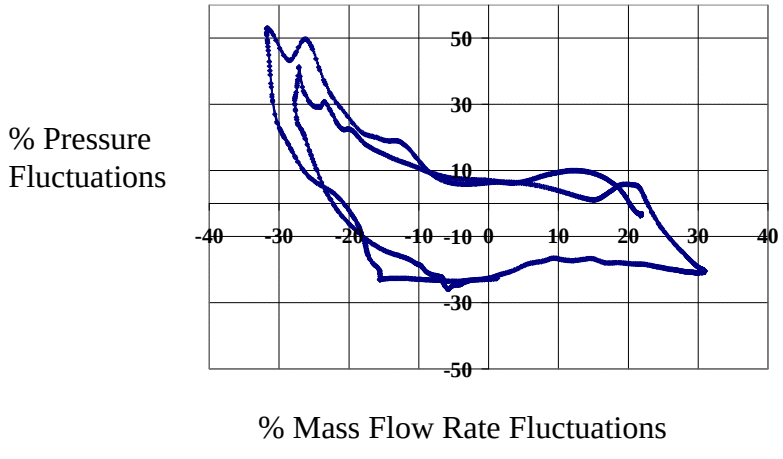

Figure 5.9 Pressure and mass flow rate fluctuations at operating point C (Rotor 67).

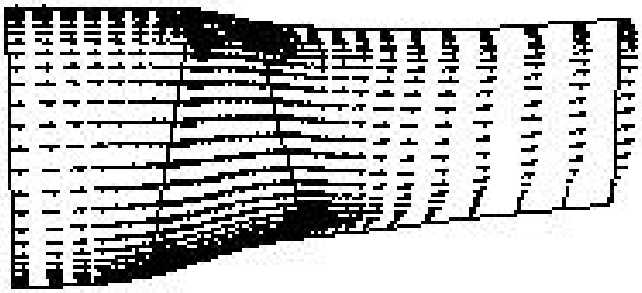

a) After ½ Rotor Cycle

b) After 1 Rotor Cycle

c) After 1.5 Rotor Cycle

Figure 5.10 Temporal growth of reversed flow at operating point C (Rotor 67).

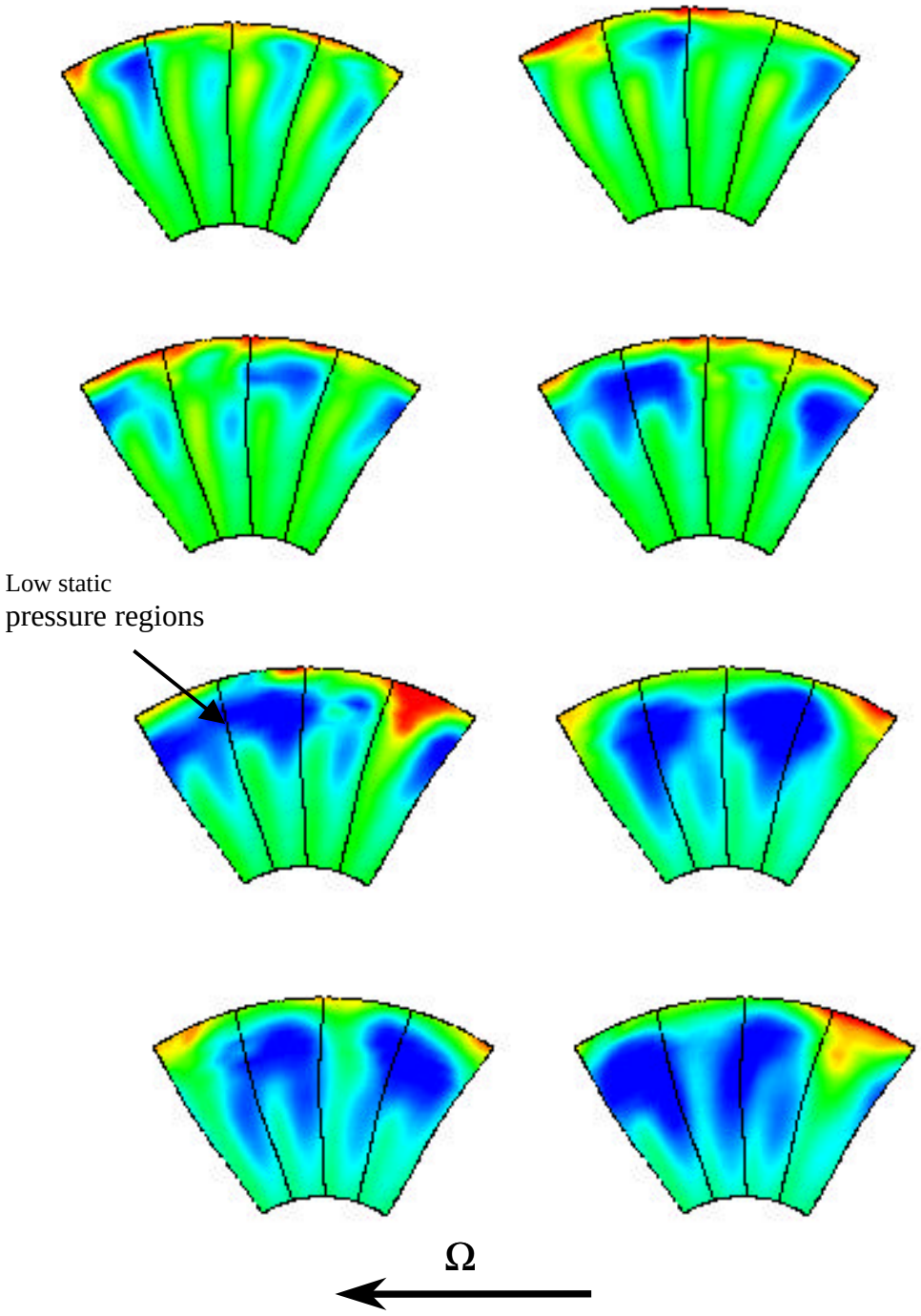

Figure 5.11 Instantaneous circumferential pressure fields at operating point C (Rotor 67).

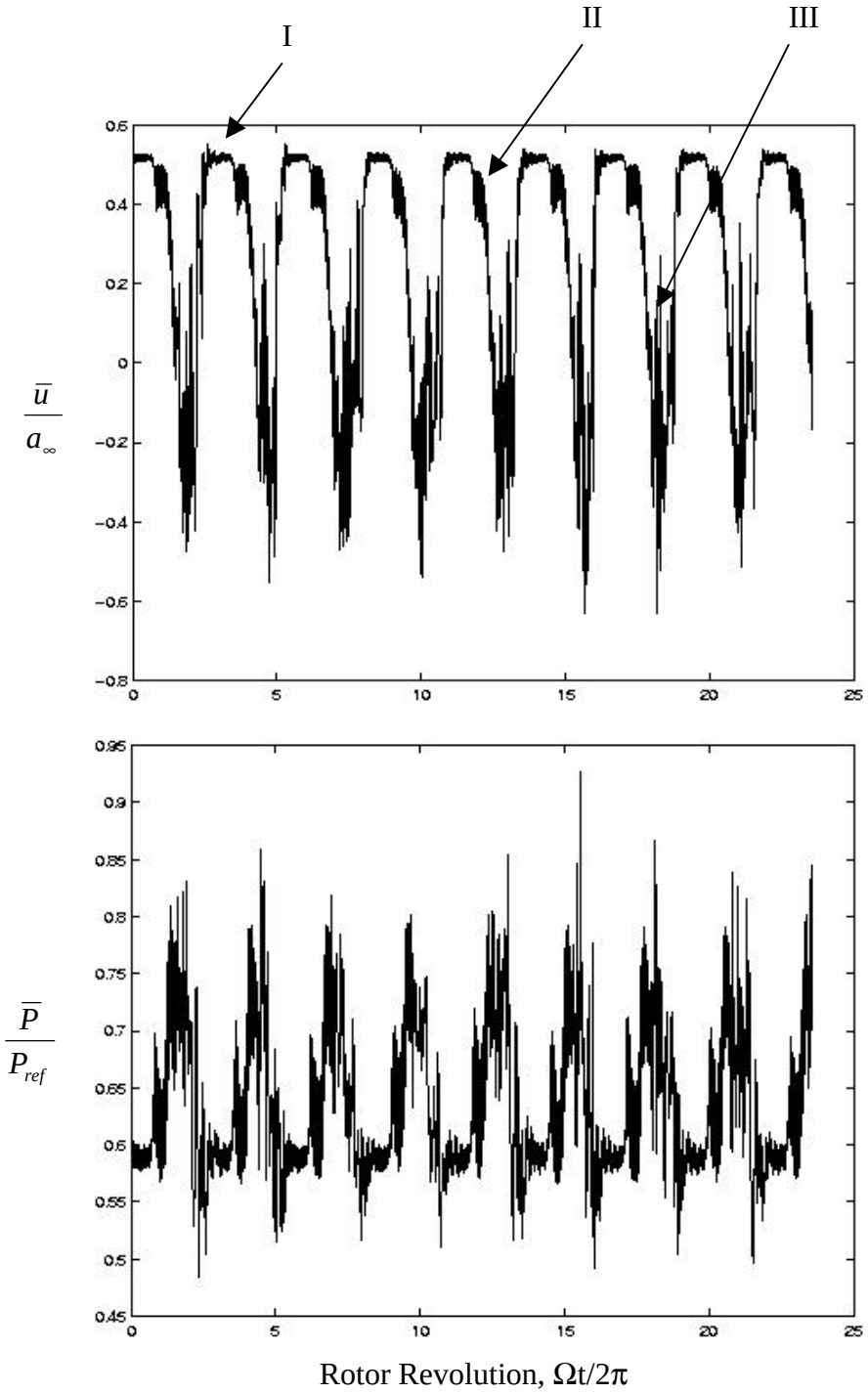

Figure 5.12 Time history of averaged axial velocity and pressure computed by probes upstream of the compressor face at operating point C (Rotor 67).

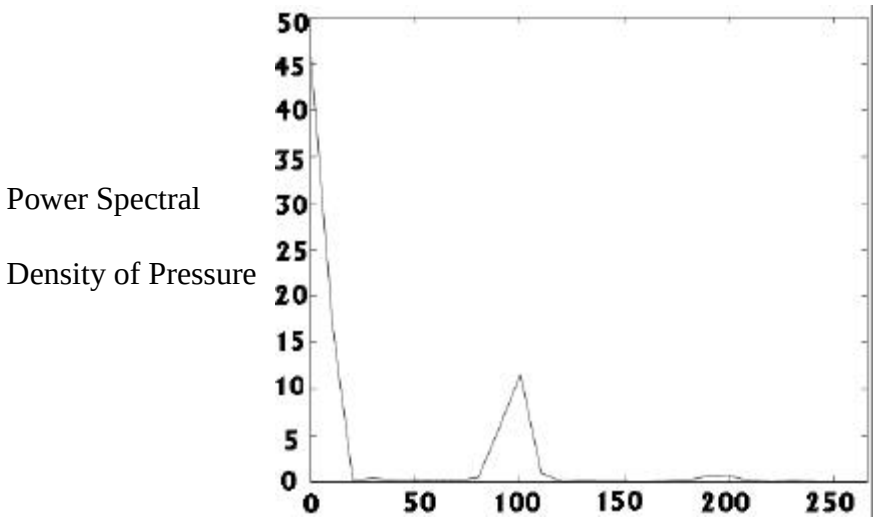

Figure 5.13 Power spectral density of the azimuthally averaged pressure fluctuations upstream of the compressor face at operating point C (Rotor 67).

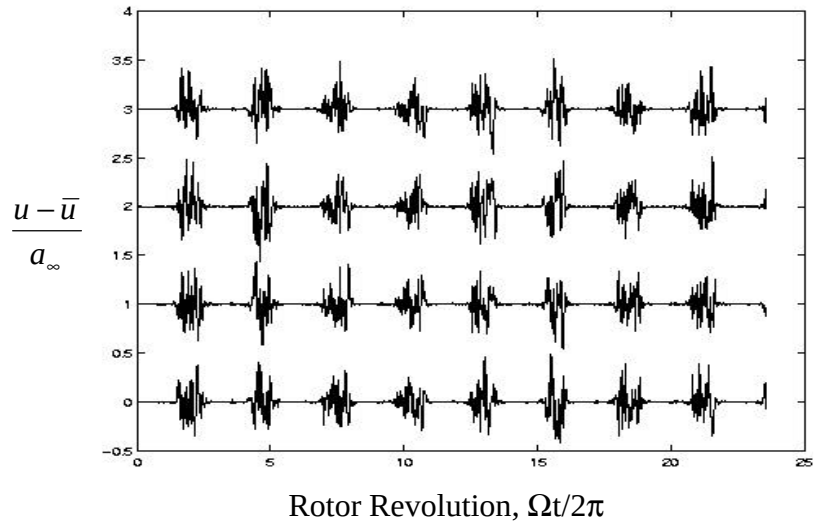

Figure 5.14 Time history of axial velocity deviation from its azimuthally averaged axial velocity upstream of the compressor face at operating point C (Rotor 67).

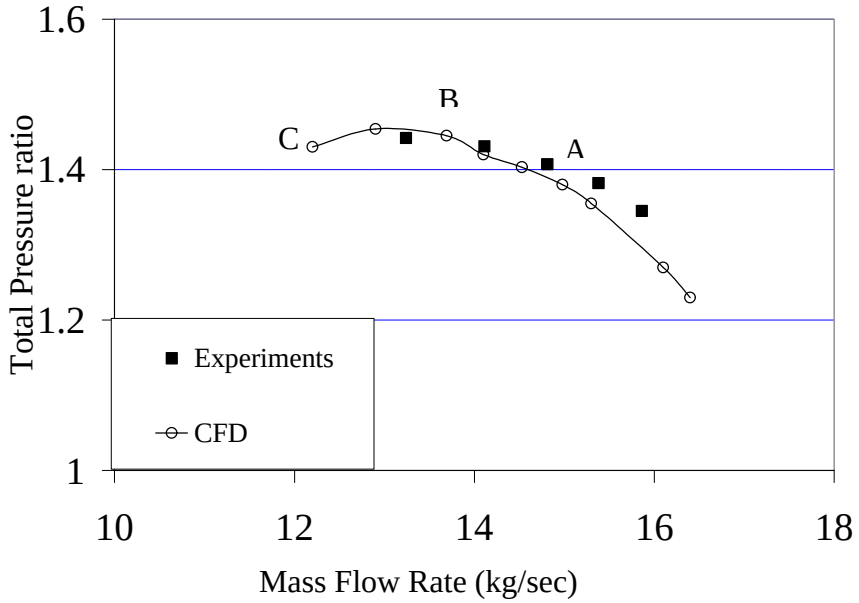

Figure 5.15 Computed and measured characteristic performance map at 70% design speed (Rotor 37).

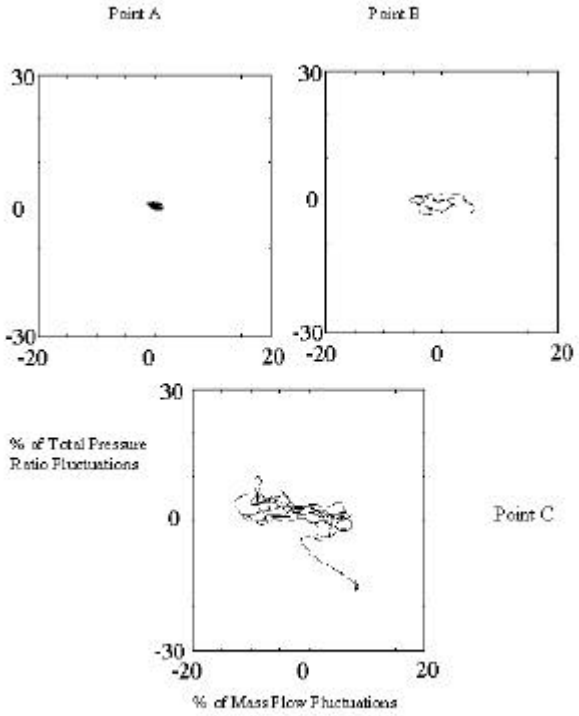

Figure 5.16 Fluctuations of total pressure ratio versus mass flow rate at different operating conditions (Rotor 37).

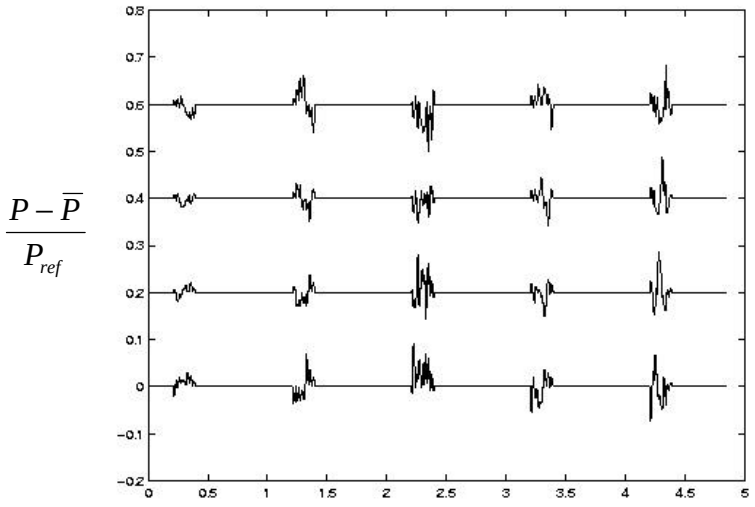

Figure 5.17 Time history of pressure deviation from its azimuthally averaged pressure upstream of the compressor face at operating point C (Rotor 37).

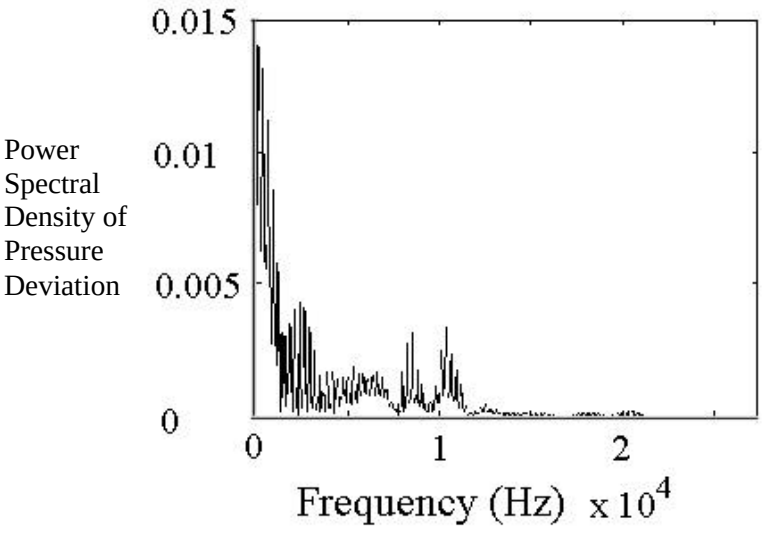

Figure 5.18 Power spectral density of pressure deviation from its azimuthally averaged pressure fluctuations upstream of the compressor face at operating point C (Rotor 37).

CHAPTER VI

ACTIVE CONTROL STUDIES OF ROTOR 67 CONFIGURATION

Axial compressors operate in regimes where both rotating stall and surge impose limits on low flow rate operability. The useful operating range can be as small as 10 percent of the design flow rate. For example, in the compressor Rotor 67 described in the previous chapters, the surge line occurs at 92% of the choked flow. In the other words, the stable operating range in this rotor is just 8% of the maximum delivery flow. Therefore, control methodologies are necessary for extending the stable operating range of compressors. Control strategies designed to enhance the operability of compressors must address rotating stall, surge, and their interaction. In recent years, there has been much work on improving operating range of compression systems using active and passive control methods. These methods were discussed in Section 2.3 and schematically shown in Figure 2.7.

Ever since the Moore-Greitzer[23-24] model became available, work on feedback stabilization methods for compressors has been extensive and a considerable number of papers have been published. One of the most common of these methods is bleeding. Since its application in early compressors more than 60 years ago, bleeding has been used for engine start-up purposes. Bleeding has also been used over the past two decades to shift the surge line to lower mass flow. Fisher[41] used a bleed valve in a centrifugal

compressor at various compressor shaft speeds. At the maximum speed, 78000 RPM, the surge line was decreased by 21% toward the low mass flow rate side. Between 50000 and 70000 RPM, this shift was 28% to 31%. In a series of experiments, Pinsley et al.[42] studied centrifugal surge control using throttle valves as actuators, and a 25% reduction of mass flow rate prior to onset of surge was achieved. The amount of bleeding has been reported ranges from 1 to 10 percent of the mean flow[40-43]. Eveker et al.[97] were one of the first groups to report successful experimental implementation of a bleed valve controller. In the series of papers published by Yeung and Murray [40], and Wang et al.[98], at Cal Tech, analysis of bleed valve rate requirements for suppressing rotating stall are presented. Yeung et al.[40]experimentally showed that the rate of bleeding may be reduced by injecting air downstream of the compressor face. They showed that by one to two percent air injection, the rate of bleeding could be reduced by 30%. Prasad et al.[99] at Georgia Tech used bleeding in the plenum to reject surge in axial and centrifugal compressors.

In this study, two types of bleeding were considered. The first one is a simple steady bleeding control, referred to as open-loop control. The second type is an unsteady bleeding linked to the pressure fluctuations upstream of the compressor face. This is referred to as closed-loop control. The bleed valves in both cases were located one tip-chord downstream of the rotor blades. This chapter discusses the CFD results for the two control methods applied to the NASA Rotor 67 compressor. In Section 6.1, results for

the open-loop control are presented. Section 6.2 deals with the results for the closed-loop control.

6.1 OPEN-LOOP CONTROL STUDIES

In open-loop control, a fraction of the mass flow rate is removed through a valve placed on the compressor casing. Such a steady bleeding is inefficient and must be turned off during design operations. A bleed valve will have its own throttle characteristic, which can be tailored to enhance the stable operation of the compressor. A schematic of the steady bleeding is shown in Figure 3.6.

In this study, to simulate the open-loop control, it was assumed that flow is removed at a constant rate in an azimuthally uniform rate. The fraction of mass flow rate and the locations of the bleed valves are specified by the user. As pointed out in Section 3.6, the normal velocity component is calculated from the amount of the bleed flow and the bleed area, as shown in Equation (3-57).

To see the effects of the open-loop control on the flow field, a 3.2% of the mean flow bleed was applied to the unstable operating condition at point C, shown in Figure 6.1. Figure 6.2 shows the velocity vectors at the azimuthal plane at midpitch with the passive bleed control after 1.5 rotor revolutions. It may be recalled that the compressor experienced modified stall at the unstable branch (B-C) of the compressor map. A comparison between Figures 6.2 and 5.10 (reproduced here for convenience) shows that the compressor casing is seen to restore attached flow over much of the whole compressor.

Figure 6.3 shows the fluctuations in mass flow rate and total pressure ratio for this steady bleed condition. The computed mean mass flow rate entering the plenum was 30.4 kg/sec, which is 87.5% of the choked flow rate, and the mean total pressure ratio was 1.65. This operating point is shown in the Figure 6.1, indicated by point D. In Figure 6.1, the horizontal axis is the mass flow rate through the compressor before bleeding, $\dot{m}_c$, and the vertical axis is the total pressure ratio for the whole system including the bleeding. As can be seen, a 3.2% bleed brings the compressor to a new operating point, D. This is because removing some high-pressure air from the compressor causes a reduction in the total pressure at the rotor exit, and reduces the total-to-total pressure ratio of the rotor. Also, a comparison between Figure 5.9 and Figure 6.3 (reproduced here for convenience) reveal that this open-loop bleeding reduces the amplitude of total pressure oscillations by 75%.

Referring back to the performance map with open-loop control shown in Figure 6.1, it is seen that the stable operation of the engine has been extended to 87.6% of the choked mass flow rate, giving effectively a 38.2% increase in the operating range of the compressor.

Another way to compare the controlled-operating point D in the performance map with the other operating conditions is given in Figure 6.4. In this figure, the vertical axis represents the non-dimensional pressure rise and the horizontal axis is the mass flow rate entering the plenum, $\dot{m}_p$, which is $\dot{m}_c - \dot{m}_b$, where $\dot{m}_b$ is the bleeding mass flow rate through the bleed valve. A 3.2% bleed from the operating point C brings the compressor

to a new operating condition D. The reason for choosing the horizontal axis to be $\dot{m}_p$ is to compare the throttle position for this point with the throttle positions for other points in the compressor performance map. Under steady state conditions $\dot{m}_p = \dot{m}_t$, where $\dot{m}_t$ is the throttle mass flow rate. From a knowledge of $\dot{m}_t$ and gage pressure Δp at throttle valve, the corresponding throttle characteristic K_t, was calculated as follows:

$$\dot{m}_t = K_t \sqrt{\Delta p} \qquad \textbf{(6-1)}$$

The throttle characteristic map was obtained by using the calculated K_t at point D and Equation (6-1) for different mass flow rates, and is plotted as a dashed line in Figure 6.4. In other words, the dashed line represents all the points having the same throttle position. A comparison between Figure 6.1 and Figure 6.4 shows that even though the bleeding was applied to point C, bringing the compressor to the operating point D, the operating point D has the same throttle characteristic as point F in the performance map. From this point of view, the branch B-D is a stable branch of the performance map. The useful mass flow rate, representing flow that goes into downstream components, is 29.43 kg/sec. This is a useful extension of the operating conditions. Without open-loop control the system will enter into modified surge at mass flow rates below 31.6 kg/sec (point B).

To understand why and how the bleed-air mechanism works, the flow field was examined. Figure 6.5 shows a comparison between the non-dimensional axial velocity at

point C, a stalled and unstable condition, after three different rotor cycles, and point D, a stable condition achieved with bleed valve control. The data was acquired near the leading edge at mid-passage of the compressor. It is seen that local reversed flow regions first originate near the blade leading edge. If left unchecked, this flow region grew temporally and spatially, leading the compressor to an uncontrolled growth of mass flow rate and pressure fluctuations. When 3.2% of the total flow rate entering the inlet was removed from the compressor, the reversed flow regions near the leading edge disappeared and a stable operating condition was restored

As in operating points B and C, four "numerical" velocity probes were implemented circumferentially at the upstream of the compressor face, shown in Figure 5.3, to trace the axial velocity component. The spatially averaged values of axial velocity and static pressure from the probes readings are shown in Figure 6.6 and 6.8. Compared with results for point C in the Figure 5.12 (reproduced as part of Figure 6.6), the probes showed only very small fluctuations and reversed flow was completely eliminated.

Figure 6.7 illustrates the deviation of axial velocity from the spatially averaged axial velocity for all of the four probes. The time traces shown in this figure are shifted vertically by a constant interval. It is observed that all of the probes are identical and no circumferential disturbances indicative of rotating stall were observed. A comparison between Figure 5.14 and Figure 6.7 (reproduced here for convenience) reveal that the open-loop control eliminates the stall cells. Figures 6.6 through 6.8 show that the compressor is in stable operation.

6.2 CLOSED-LOOP CONTROL STUDIES

In the previous section, the effects of open-loop control on the flowfield were discussed. As mentioned earlier, such a steady preset bleeding is inefficient and must be turned off when the compressor operates close to design conditions. Therefore, a closed-loop active control methodology was studied. The closed-loop control was applied to the NASA Rotor 67 configuration, and results are presented in this section.

In this approach, the bleed rate was linked to pressure amplitudes upstream of the compressor face, which monitored by a control unit. This control unit received the pressure signals from some probes located upstream of the compressor face, determined the amount of bleeding needed, and activated the bleed valve. The mass flow of the bleed valve is linked to the instantaneous amplitude of pressure fluctuations acquired by the "computational" probes. The bleed valve was activated whenever the pressure sensors in the upstream of compressor face experienced high-pressure fluctuations. The amount of air that is removed, $\dot{m}_b$, is related to the gage pressure Δp at the bleed location:

$$\dot{m}_b = K_b A_b \sqrt{\Delta p} \qquad \textbf{(6-2)}$$

In Equation (6-2), K_b is the bleed valve constant and is related to the valve geometry. Quantity A_b is the bleed valve area and

$$\Delta p = p_b - p_\infty \tag{6-3}$$

where p_b and p_∞ are the pressure at the bleed location and ambient pressure, respectively. The pressure, density, and the two components of tangential velocity were extrapolated from the interior. The normal velocity at the bleeding points was calculated using Equation (6-2):

$$u_n = \frac{k_b \sqrt{\Delta p}}{r_b} \tag{6-4}$$

Figure 3.7 illustrates the schematic of the closed-loop diffuser-bleed valve control used in this study.

The following parameters, which are user inputs, identify the active bleed configuration:

- Bleeding locations
- Pressure sensor locations
- Bleed characteristic constant
- Permitted upper and lower limits of pressure for the pressure sensors

In this study, the "numerical" probes were located at 30% tip chord upstream of the compressor face. The bleed valve was placed one tip chord downstream of the rotor. As in open-loop bleeding, the bleeding under feedback control was circumferentially uniform on each of the flow passages. At each time step, if the pressure values at the

probes were out of the permitted fluctuation limits, the bleed valve removed some air from the compressor.

The closed-loop control was applied to point C, in Figure 6.1. Figure 6.9 shows the circumferential averaged pressure fluctuation of the four probes at operating point C without bleed control. As pointed out earlier, three levels of amplitudes were observed. The bleed valve was not activated for the first two lower amplitude levels, the recovery and precursor levels. As shown in Figure 6.8, the upper permitted limit of the inlet pressure fluctuations was set to $0.67P_{\infty}$ and the lower one was chosen $0.54P_{\infty}$. The characteristic constant value K_b in Equation (6-2) was chosen to be 3.0. This value was chosen to ensure the rate of mass bleeding flow was less than 2% of the mean flow.

Figure 6.10 shows the fluctuations of total pressure ratio versus mass flow rate fluctuations. This operating condition is referred as point E in the performance map, Figure 6.1. A comparison with Figure 5.9 shows that the amplitude of fluctuations were reduced by 30% and 40% in total pressure ratio and mass flow rate, respectively, when closed-loop control was used. However, the reduction in the total pressure fluctuations was larger for open-loop control. As mentioned earlier, the horizontal axis in Figure 6.1 is the mass flow rate through the compressor before bleeding. Figure 6.1 shows that the closed-loop approach restores the stable operating condition at a higher pressure ratio.

Figure 6.11 shows the pressure rise across the compressor stage versus the mass flow rate entering the plenum. In this figure, a methodology similar to the one used in open-loop control was used to compute the throttle characteristic, K_t, and plot the throttle

characteristic map. From Figure 6.11, it can be seen that the controlled operating point E has the same throttle position as the unstable operating point G. It should be mentioned that the air bleeding rates for operating points D and E were different. At the operating point D (open-loop control) the mass flow rate $\dot{m}_p$ was 30.41 kg/sec, whereas at point E (closed-loop control), the mass flow rate was 30.03 kg/sec. The averaged bleed flow rate at operating point E was about 1.8 percent of the mean flow rate, where at point D, it was 3.2%. Also, from Figure 6.11, it can be concluded that the useful mass flow rate can be as low as 29.49 kg/sec without instabilities.

The spatial average of axial velocity from the probes' readings is shown in Figure 6.12. Compared to results for point C in the Figure 5.14, the amplitude of the axial fluctuations was reduced, and no reversed flow was observed. The fluctuations were large compare to the 3.2% steady bleeding case. Figure 6.13 illustrates the deviation of axial velocity from the spatially averaged axial velocity shown in Figure 6.12. The velocity time traces shown in this figure are shifted vertically by a constant interval. It is observed that the probes show small circumferential disturbances. The amplitude of these disturbances was only 20% of the disturbance amplitude for the unstable operating point C, shown in Figure 5.14. From Figures 6.10 and 6.13, it may be concluded that the compressor is in a stable operating condition at point E.

The table below summarizes the calculations reported in this study. It is clear that both open-loop and closed-loop controls provide a useful extension of the stall margin in the system.

Cases studied	$\dot{m}_c$ (kg/sec)	$\dot{m}_b$ (kg/sec)	$\dot{m}_p = \dot{m}_c - \dot{m}_b$ (kg/sec)	% o Extension of operability margin $\frac{\dot{m}_{Onset\ of\ Stall} - \dot{m}_c}{\dot{m}_{Choked} - \dot{m}_{Onset\ of\ Stall}} x100$
Stalled condition operating point C	29.4	____	29.4	Unstable
Open-loop control operating point D	30.41	0.973	29.437	38.2
Closed-loop control operating point E	30.03	0.541	29.49	50.3

Table 6.1 Summary of stall margin extension for the two control schemes studied.

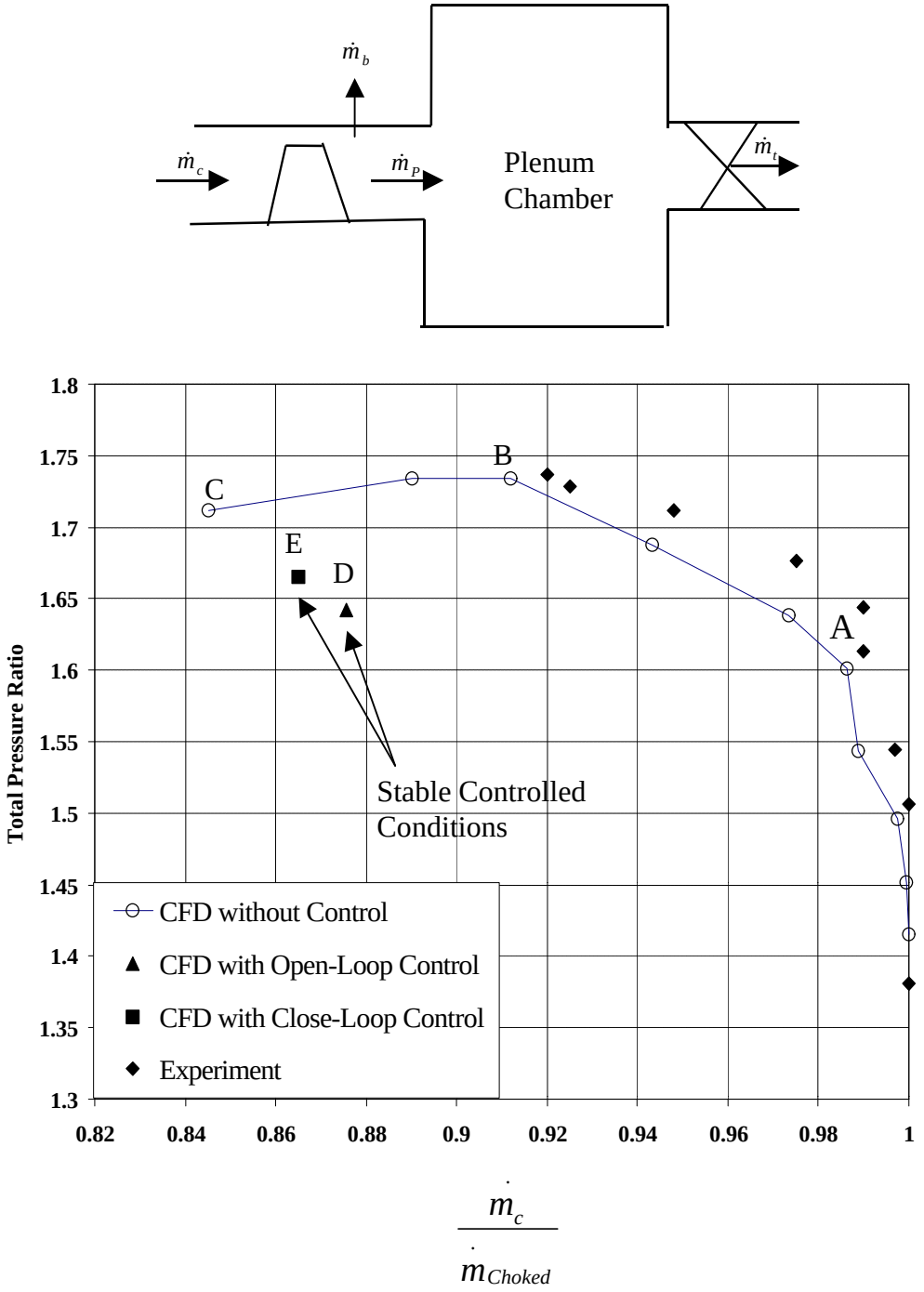

Figure 6.1 Characteristic performance map with bleed control (Rotor 67).

Without control, operating point C.

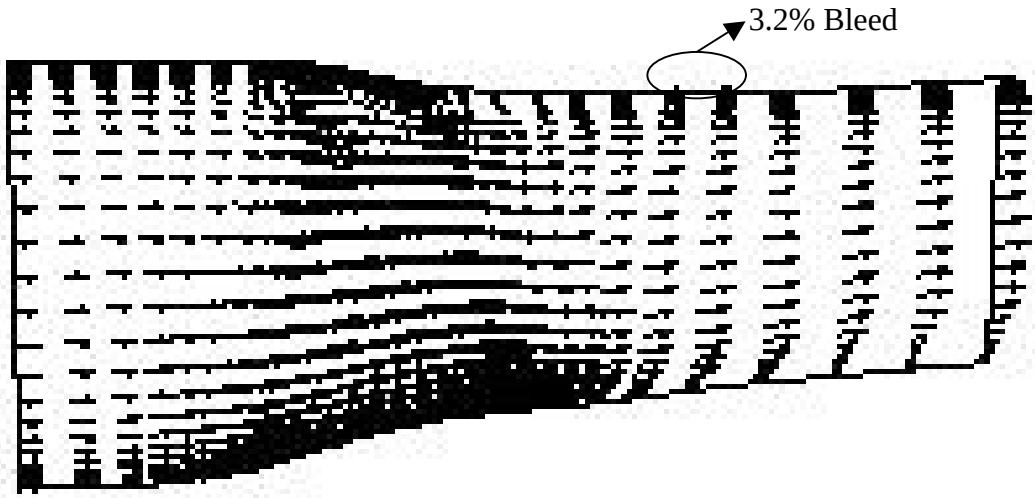

With open-loop control, operating point D.

Figure 6.2 Velocity profile with/without open-loop control (Rotor 67).

Without control, operating point C

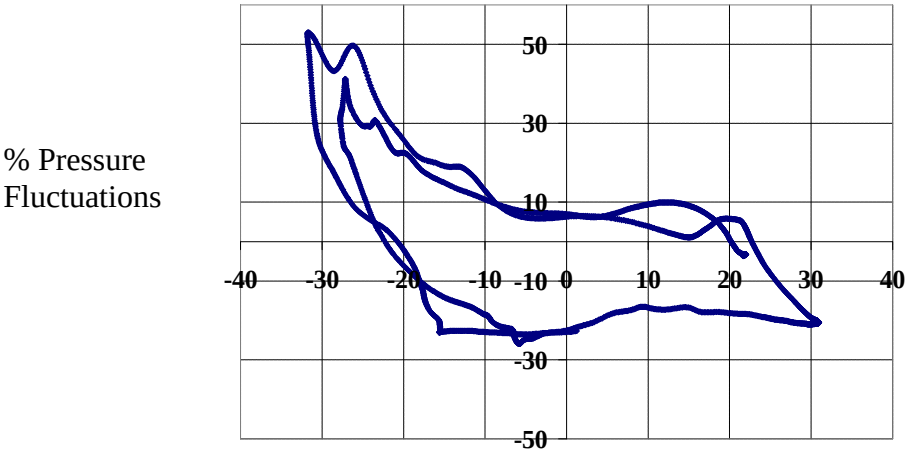

With open-loop control, operating point D

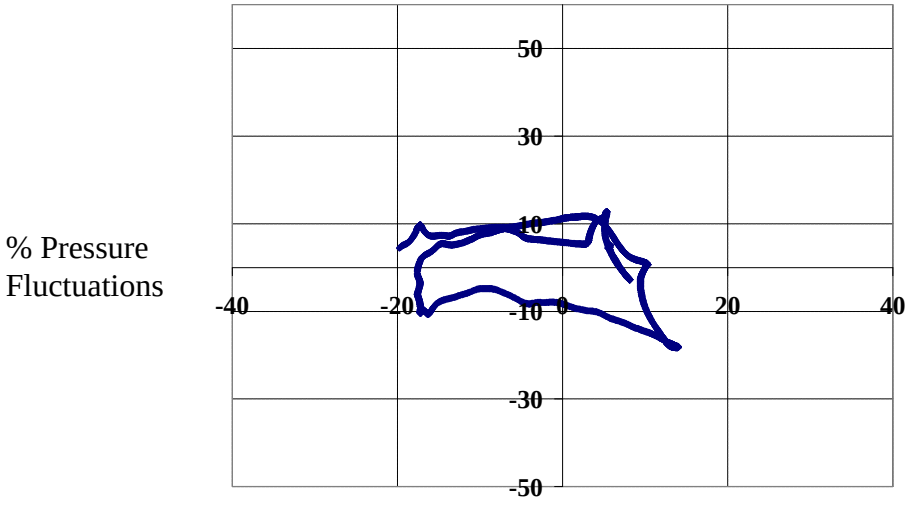

Figure 6.3 Total pressure ratio and mass flow rate fluctuations with/without open-loop control (Rotor 67).

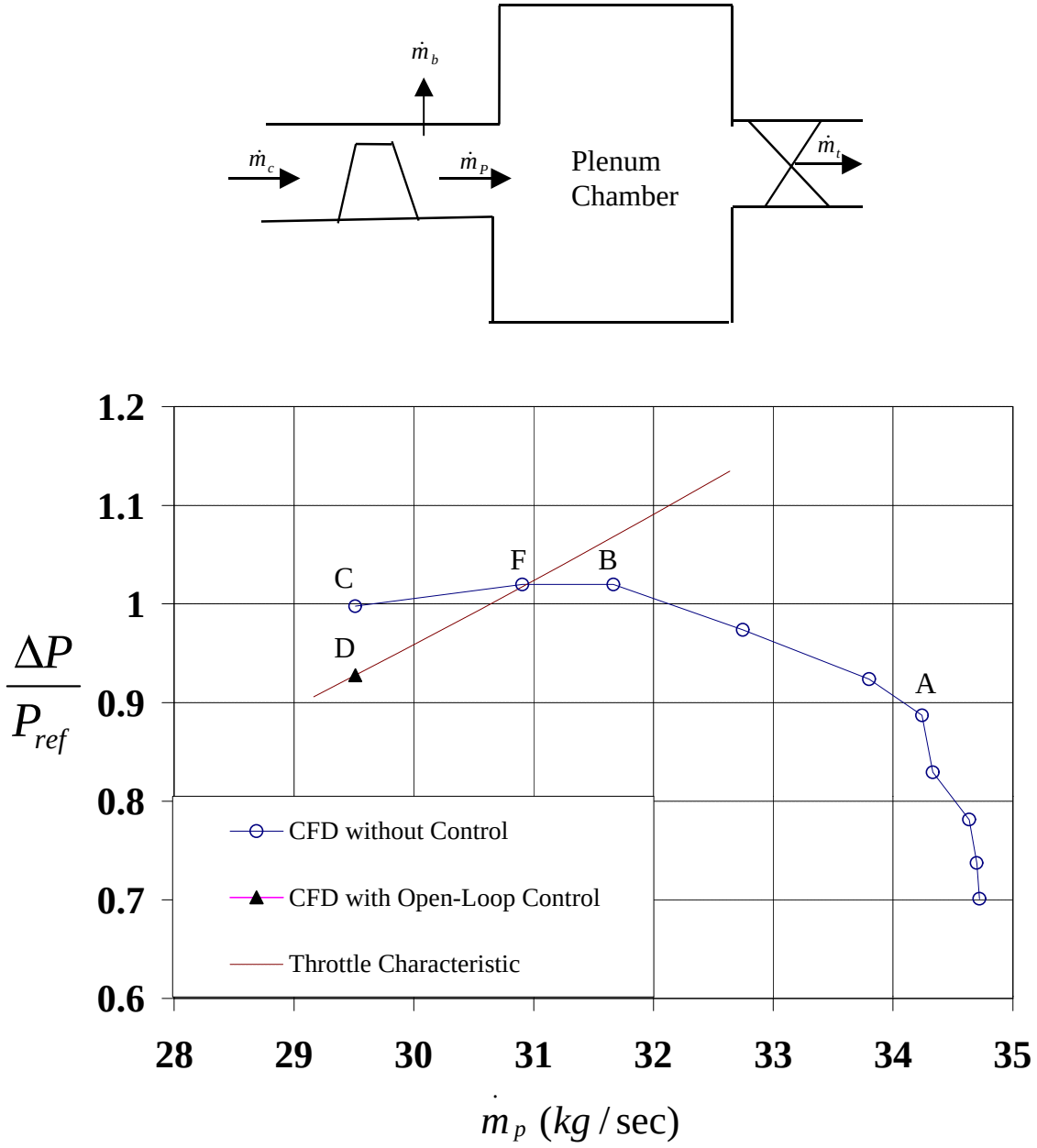

Figure 6.4 Characteristic performance map with throttle characteristic for open-loop control (Rotor 67).

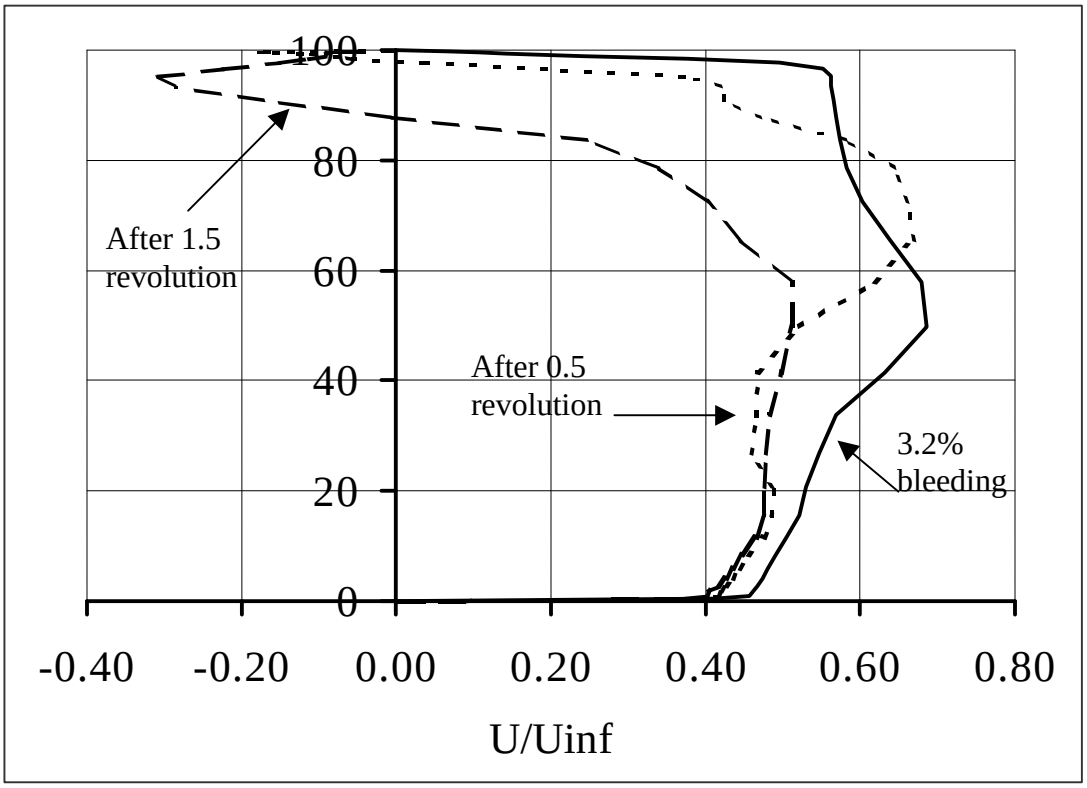

Figure 6.5 Spanwise distribution of axial velocity at mid-passage near the leading edge (Rotor 67).

Without control, operating point C

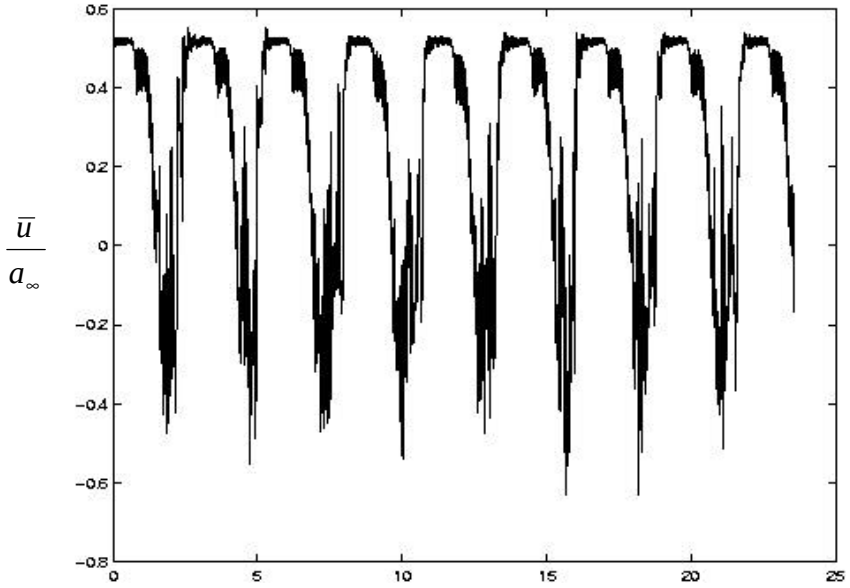

Rotor Revolution, Ωt/2π

With open-loop control, operating point D

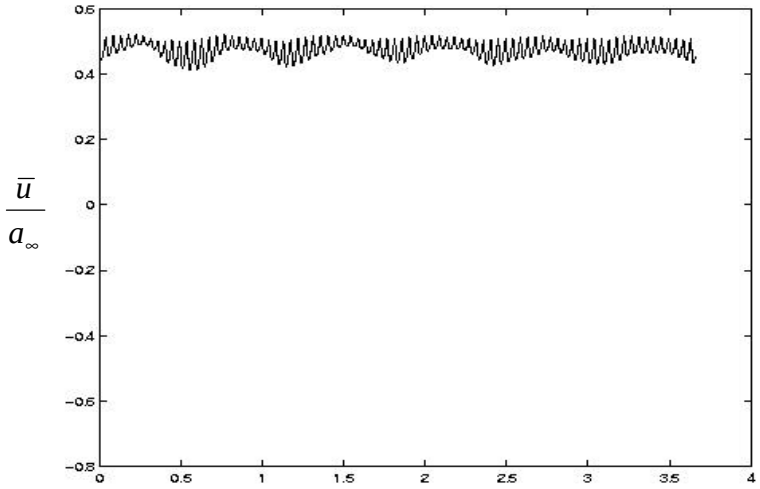

Rotor Revolution, Ωt/2π

Figure 6.6 Time history of axial velocity with/without open-loop control (Rotor 67).

Without control, operating point C

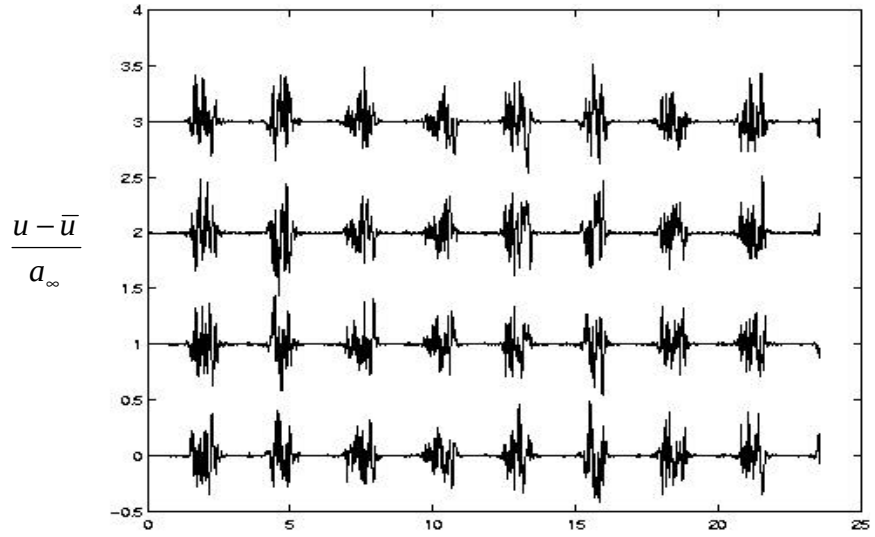

With open-loop control, operating point D

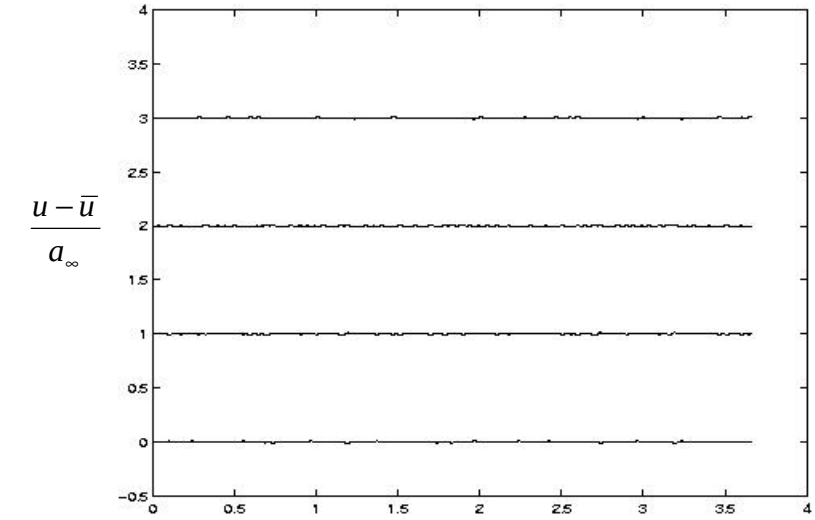

Figure 6.7 Time history of axial velocity deviation from its azimuthally averaged axial velocity with/without open-loop control (Rotor 67).

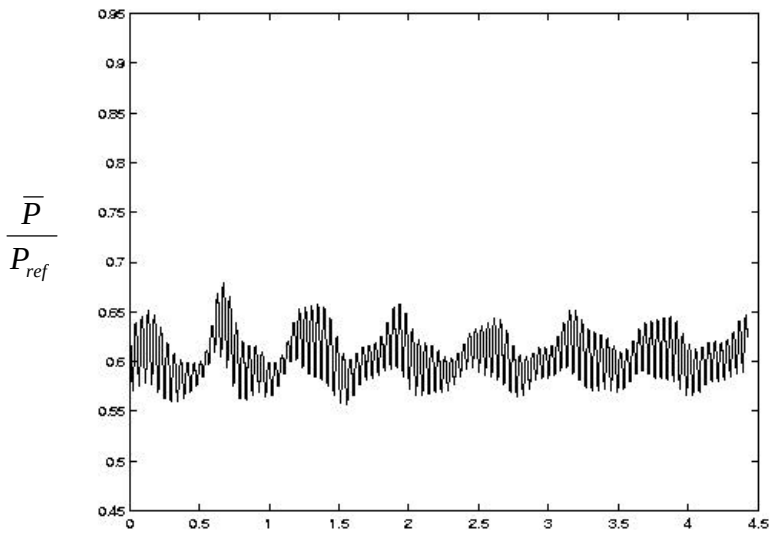

Figure 6.8 Time history of static pressure under open-loop control (Rotor 67).

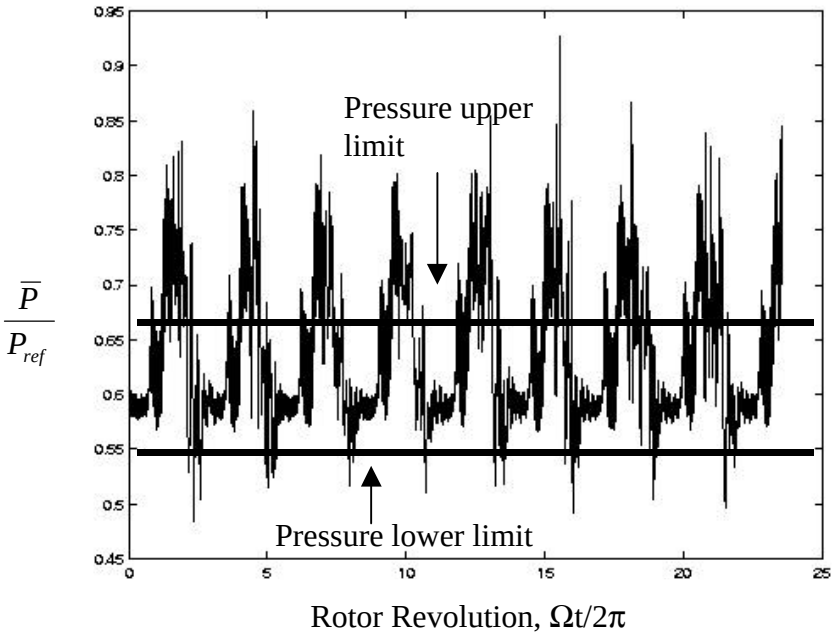

Figure 6.9 Upper and lower limit of pressures that trigger closed-loop control (Rotor 67).

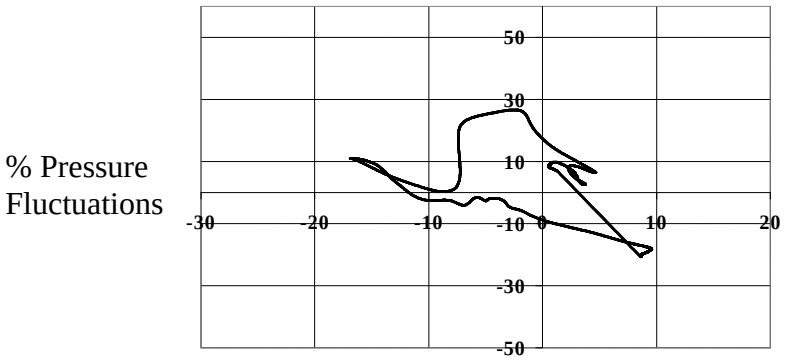

Figure 6.10 Total pressure ratio and mass flow rate fluctuations under closed-loop control (Rotor 67).

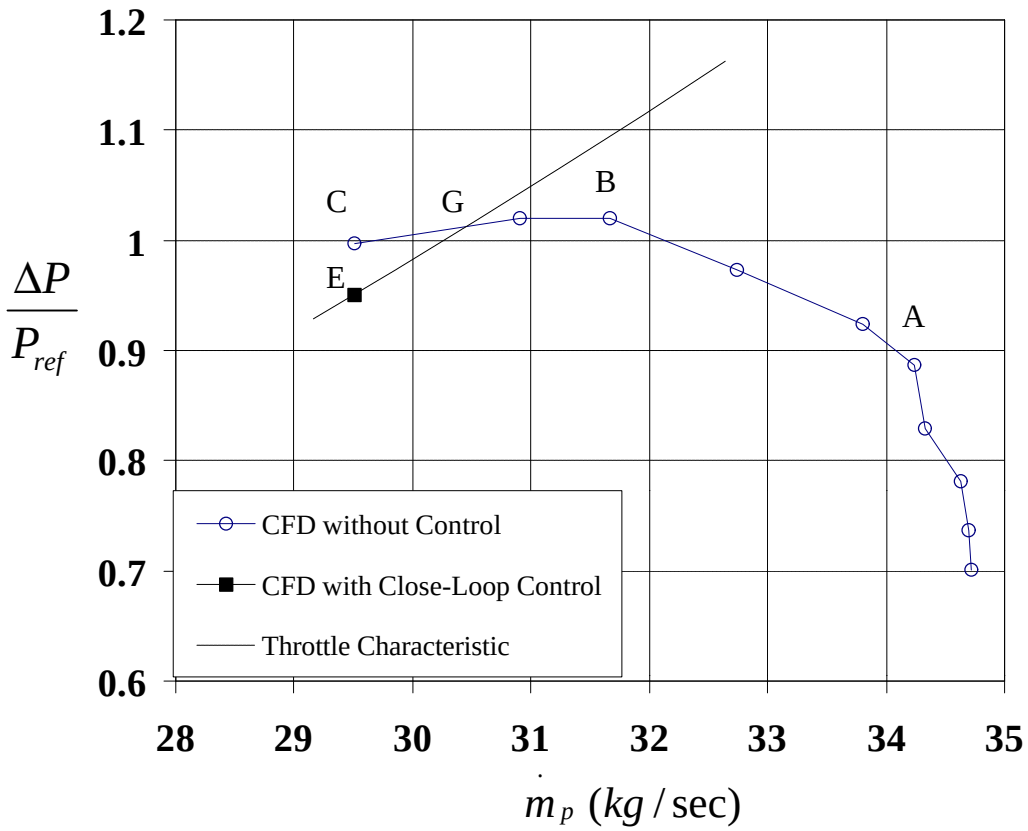

Figure 6.11 Characteristic performance map with throttle characteristic for closed-loop control (Rotor 67).

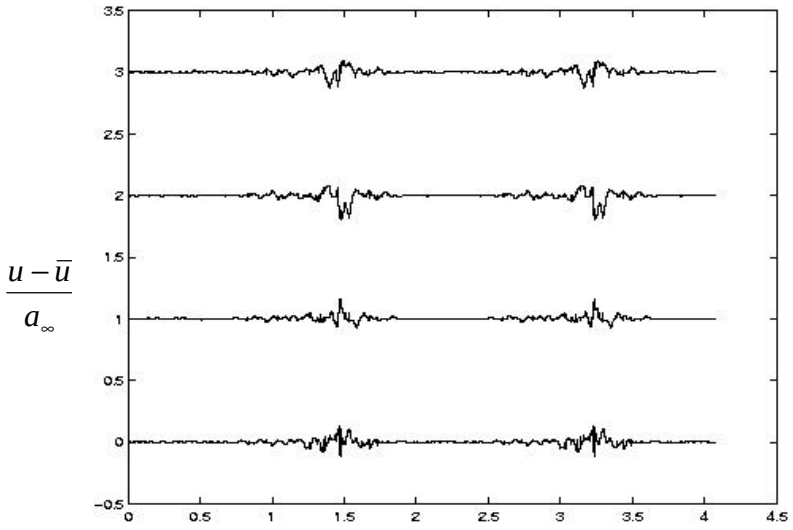

Figure 6.12 Time history of axial velocity under closed-loop control (Rotor 67).

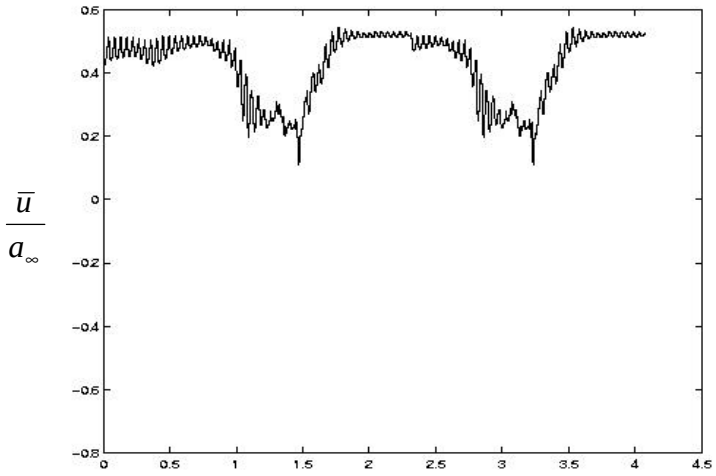

Figure 6.13 Time history of axial velocity deviation from its azimuthally averaged axial velocity upstream of the compressor face under closed-loop control (Rotor 67).

CHAPTER VII

CONCLUSIONS AND RECOMMENDATIONS

In the present work, a three-dimensional unsteady Navier-Stokes analysis capable of modeling multistage turbomachinery components has been developed. This method uses a cell-vertex finite volume scheme to solve the governing equations in a body-fitted rotating coordinate system. The scheme is third order accurate in space and first or second order in time. A one-equation Spalart-Allmaras turbulence model equation was implemented in the solver to account for the turbulence effects. The analysis can also use a previously stored solution file with the corresponding grid file, to restart the computations.

A number of code-validation studies have been done for centrifugal and axial configurations. Studies have also been done to understand some of the mechanisms behind rotating stall and surge. Open-loop bleed control and closed-loop control methods have been studied and are demonstrated to stabilize the system. To the author's knowledge, this is the first application of a fully 3-D unsteady viscous flow analysis for modeling axial compressor control in this fashion.

In this chapter, the conclusions of this research are presented in Section 7.1. The recommendations for further work in the future are given in Section 7.2.

7.1 CONCLUSIONS

The following items are concluded from the current work:

1- Three-dimensional unsteady flow solvers such as the one developed here are valuable tools for modeling and understanding rotating stall and surge. These methods are suitable for identifying "hot spots" in the flow field, for redesigning the system (e.g. casing treatment), and for developing flow control devices for the system.

2- The plenum-chamber downstream plays a critical role in surge development. The exchange of energy between the plenum chamber and the flow inside the blade passages is a major mechanism for surge. Therefore, devices and mechanisms that directly alter the pressure levels in the plenum chamber are an effective way of controlling surge. This observation has been numerically demonstrated in this work.

3- Inlet disturbances can trigger rotating stall. The stall cells in the present simulation appear to rotate at 38% of the rotor RPM, in the direction of the rotor rotation. This phenomenon is consistent with experimental observations. It should be possible to mitigate rotating stall through careful redesign of the inlet, through guide vanes, or through active control (e.g. jets).

4- Rotating stall and surge phenomena are often accompanied by temporally growing pressure and velocity fluctuations in the inlet upstream of the compressor face. These oscillations may roughly be divided into these

categories: precursor, stall, and recovery. It should therefore be possible to use these oscillations, in particular the precursors, to trigger open-loop or closed-loop control. While this has been known for some time, this is the first time precursor waves have been used in a numerical simulation to detect and automatically control rotating stall, surge, and modified surge.

5- It should be possible to establish simple rule-based control laws linking the inlet pressure fluctuations to the amount of actuation needed. A very simple law that triggers bleeding whenever the upstream pressures exceeded a preset level user was found to be effective. This law also accounted for the bleed valve characteristics.

7.2 RECOMMENDATIONS

The following items are suggested to extend the current work:

1- The outlet boundary conditions at off-design conditions play a dominant role in simulating the instability developments appropriately. In this work, a simple unsteady boundary condition was introduced, and a nominal fixed mass flow rate controlled the compressor operation. Another type of outlet boundary condition, that should be tested, is to let this nominal mass flow through the throttle also fluctuate with time. In this manner both backpressure and throttle mass flow vary at each time step. This boundary may be written as:

$$\frac{dp_p}{dt} = \frac{a_p^2}{V_p}(\dot{m}_c - \dot{m}_t) \quad \textbf{(7-1)}$$

$$\dot{m}_t = K_t A_t \sqrt{\Delta P} \quad \textbf{(7-2)}$$

where K_t is the throttle characteristic constant and is related to the throttle geometry, and A_t is the throttle valve area. Here, ΔP is the pressure difference between the plenum pressure or compressor backpressure and the components downstream, e.g. a second stage or a combustor. This may be done stage by stage, providing a weak 1-D coupling between the various components of the compression system and the combustor.

2- This work focused on the analysis of flowfield and the fluid dynamic phenomena in single stage compressors with multiple blade passages. The work should be extended to the simulation of multi stage compressors considering rotor-stator interactions. In rotor-stator interactions, the rotor grid block, similar to the present simulation of the rotors, will be moving in the pitchwise direction, while the stator grid block remains stationary. At the boundaries connecting the moving and stationary regions, an interpolation approach may be used to transfer the information from the stationary block to the rotating block.

3- In the present research, the open-loop bleeding control removed a fraction of high-pressurized air at a fixed rate from the compressor. The bleed rate can be

sinusoidally varied at the rotating stall frequency with an appropriate phase lag. The bleeding mass flow rate, $\dot{m}_b$, may be written as follows:

$$\dot{m}_b = \dot{m}_{b\,\mathrm{Mean}} + \dot{m}_f \sin(w_s t + j) \qquad \textbf{(7-3)}$$

Here, $\dot{m}_{b\,\mathrm{Mean}}$ is the mean mass flow removed from the compressor, $\dot{m}_f$ is the amplitude of the pulsed bleeding, ω_s is the rotating speed of the stalled cells, and j is the phase lag. The benefit of this methodology is that the controller removes the air only when a stalled cell passes by the bleed valve.

4- The present approach underestimates the total pressure rise across the compressor. The one-equation turbulence model may be a source of this discrepancy. Although a limited number of grid sensitivity studies have been done, an inadequate number of grid points may also have contributed to this error. These discrepancies must be systematically studied and eliminated. Thanks to the availability powerful high-performance computers, one near-term possibility is the use of LES methodology on sufficiently fine grids.

5- Different types of control devices, such as inlet guide vanes, casing treatment, and so on, may be simulated with this solver and their effects on the flowfield can be investigated. Recently, air injection control methodology has been computationally simulated[70]. Experimental evidence also exists that shows that air injection may

reduce the required rate of bleeding[40]. This work should be extended to a systematic study of these concepts.

In summary, a first principles-based methodology for modeling steady-state and off-design operation of axial compressors has been developed. This method has been validated and used to study stall and surge control concepts. It is hoped that this work will serve as a useful step for future investigations in the exciting area of non-linear flow control.

REFERENCES

1. Horlock, J. H., Axial Flow Compressors, Butterworths Scientific Publications, London, 1958.
2. Gostelow, J. P., Cascade Aerodynamics, Pergamon Press, New York, NY, 1984.
3. Sebghati, J. M., Monitoring Axial-Flow Compressor Rotating Stall and Surge, Master's Thesis, The University of Tennessee, Knoxville, May 1992.
4. Ferguson, T. B., The Centrifugal Compressor Stage, Butterworths, London, 1963.
5. Japikse, D. and Baines, N. C., Introduction to Turbomachinery, Concepts ETI, Inc. and Oxford University Press, 1994.
6. Cherkassky, V. M., Pumps, Fans, Compressors, Mir Publications, Moscow, 1980.
7. Cohen, H., Rogers, G. F. C. and Saravanamuttoo, H. I. H., Gas Turbine Theory, 4th ed., Longman, Essex, 1996.
8. Hill, P. G., and Peterson, C. R., Mechanics and Thermodynamics of Propulsion, 2nd ed., Addison Wesley Publication Co., 1992.
9. Ücer, A. S., Stow, P., and Hirsch, C., Thermodynamics and Fluid Mechanics of Turbomachinery, Vol. I and II, 1985.
10. Cumpsty, N. A., Compressor Aerodynamics, Longman Scientific and Technical, Essex, 1989.
11. Gravdahl, J. T. and Egeland, O., Compressor Surge and Rotating Stall Modeling and Control, Springer, Verlay London Limited, 1999.
12. Pampreen, R. C., Compressor Surge and Stall, Concepts ETI, Inc., Norwich, Vermont, 1993.

13. de Jager, B., “Rotating Stall and Surge Control,” Proceedings of the 34th Conference on Decision & Control, New Orleans, LA, Dec. 1995.

14. Badmus, O. O., Nonlinear Dynamic Analysis and Control of Surge and Rotating Stall in Axial Compression System, Ph.D. Dissertation, Georgia Institute of Technology, March 1994.

15. Stodola, A., Steam and Gas Turbine, McGraw-Hill Book Co., New York, 1927.

16. Kearton, W. J., Turbo-Blowers and Compressors, Sir Isaac Pitman and Sons Publishers, London, 1931.

17. Fischer, K. and Thoma, D., “Investigations of the Flow Conditions in a Centrifugal Pump,” Transactions of ASME, Vol. 54, pp. 141-155, Nov. 1932.

18. Emmons, H. W., Pearson, C. E. and Grant, H. P., “Compressor Surge and Stall Propagation,” Transactions of ASME, Vol. 77, pp. 455-469, 1955.

19. Greitzer, E. M., “Surge and Rotating Stall in Axial Flow Compressor: Part 1, Theoretical Compression System Model, and Part 2, Experimental Results and Comparison with Theory,” ASME Journal of Engineering for Power Transactions of ASME, Vol. 98, pp. 190-217, April 1976.

20. Moore, F. K., “A Theory of Rotating Stall in Multistage Compressor, Parts I-III,” ASME Journal of Engineering for Power, No. 106, pp. 313-336, 1984.

21. Moore, F. K., “Stall Transient of Axial Compression Systems with Inlet Distortion,” Journal of Propulsion and Power, Vol. 2, No. 6, pp. 552-561, Nov.-Dec. 1986.

22. Hynes, T. P. and Greitzer, E. M., “A Method for Assessing the Effects of Circumferential Flow Distortion on Compressor Stability,” Journal of Turbomachinery, No. 109, pp. 371-380, July 1987.

23. Moore, F. K. and Greitzer, E. M., " A Theory of Post-Stall Transients in Axial Compression Systems Part I-Development of Equations," Journal of Engineering for Gas Turbines and Power, Vol. 108, pp. 68-76, Jan. 1986.

24. Greitzer, E. M and Moore, F. K., " A Theory of Post-Stall Transients in Axial Compression Systems Part II-Application," Journal of Engineering for Gas Turbines and Power, Vol. 108, pp. 231-239, April 1986.

25. Davis, M. W. and O'Brien, W. F., "Stage-by Stage Post Stall Compression System Modeling Technique," Journal of Propulsion and Power, No. 7, pp. 997-1005, 1991.

26. Eveker, K. M., Model Development for Active Control of Stall Phenomena in Aircraft Gas Turbine Engines, Ph.D. Dissertation, Georgia Institute of Technology, 1993.

27. Bonnaure, L. P. Modeling High Speed Multistage Compressor Stability, Master's Thesis, Massachusetts Institute of Technology, 1991.

28. McCaughan, F. E., "Application of Bifurcation Theory to Axial Flow Compressor Instability," Journal of Turbomachinery, No. 111, pp. 426-433, Oct. 1989.

29. McCaughan, F. E., "Numerical Results for Axial Flow Compressor Instability," Journal of Turbomachinery, No. 111, pp. 434-441, Oct. 1989.

30. Leonessa, A., Haddad, W. M. and Li, H., "Global Stabilization of Centrifugal Compressors via Stability-Based Switching Controller," Proceedings of the IEEE International Conference Control Applications (CCA) and IEEE International Symposium on Computer Aided Control System Design (CACSD), Vol. 2, pp. 1383-1388, Aug. 1999.

31. Botros, K. K. and Henderson, J. F., "Developments in Centrifugal Compressor Surge Control-A Technology Assessment," Journal of Turbomachinery, No. 116, pp. 240-249, 1994.

32. Bailey, E. E. and Voit, C. H., “Some Observations of Effects of Porous Casing on Operating Range of a Single Axial-Flow Compressor Rotor,” NASA TM X 2120, 1970.

33. Holman, F. F. and Kidwell, J. R., “Effects of Casing Treatment on a Small Transonic Axial-Flow Compressor,” ASME Paper 75-WA/GT-5, 1975.

34. Lee, N. K. W. and Greitzer, E. M., “Effects of Endwall Suction and Blowing on Compressor Stability Enhancement,” Journal of Turbomachinery, Vol. 112, pp. 133-144, 1990.

35. Khalid, S., “A Practical Compressor Casing Treatment,” ASME Paper 97-GT-375, April 1997.

36. Whitfield, A. Wallace, F. J. and Atkey, R. C., “The Effect of Variable Geometry on the Operating Range and Surge Margin of a Centrifugal Compressor,” ASME Paper 76-GT-98, Jan. 1976.

37. Jones, B. A., “Single Stage Experimental Evaluation of Variable Geometry Inlet Guide Vanes and Stator Blading. Part VI Final Report,” NASA CR-54559, 1970.

38. Pampreen, R. C., “The Use of Variable Inlet Guide Vanes for Automotive Gas Turbine Engine Augmentation and Load Control,” SAE Paper 760285, 1976.

39. Sheridan, D. C., Nordenson, G. E. and Amann, C. A., “Variable Compressor Geometry in the Single-Shaft Automotive Turbine Engine,” SAE Preprint 740166, 1974.

40. Yeung, S. and Murray, R. M., “Reduction of Bleed Valve Requirements for Control of Rotating Stall Using Continues Air Injection,” Proceedings of the 1997 IEEE International Conference on Control Application, Hartford, CT, pp. 683-690, Oct. 1997.

41. Fisher, F. B., “Application of Map Width Enhancement Devices to Turbocharger Compressor Stages,” SAE Paper 880794, April 1988.

42. Pinsley, J. E., Guenette, G. R., Epstein, A. H., and Greitzer, E. M., "Active Stabilization of Centrifugal Compressor Surge," Journal of Turbomachinery, No. 113, pp. 723-732, 1991.

43. Epstein, A. H., Ffows Williams, J. E. and Greitzer, E. M, "Active Suppression of Aerodynamic Instabilities in Turbomachinery," Journal of Propulsion and Power, No. 5, pp. 204-211, 1989.

44. Iura, T., and Rannie, W. D., "Experimental Investigations of Propagating Stall in Axial Compressors," Transactions of the ASME, Vol. 116, pp. 463-471, 1954.

45. Longley, J. P., "A Review of Nonlinear Flow Models for Compressor Stability," ASME Journal of Turbomachinery, pp. 202-215, 1994.

46. Paduano, J. D., "Active Control of Rotating Stall in Axial Compressors," Ph.D. Dissertation, Massachusetts Institute of Technology, 1991.

47. Gysling, D. L., Dugundji, J., Greitzer, E. M. and Epstein, A. H., "Dynamic Control of Centrifugal Compressors Using Tailored Structures," ASME Paper 90-GT-122, June 1990.

48. Lawless, P., and Fleeter, S., "Active Unsteady Aerodynamic Suppression of Rotating Stall in an Incompressible Flow Centrifugal Compressor with Vaned Diffuser," AIAA/SAE/ASME/ASEE Joint Propulsion Conference, AIAA Paper 91-1898, 1991.

49. Toyama, K., Runstadler, P. W., and Dean, R. C., "An Experimental Study of Surge in Centrifugal Compressors," Journal of Fluids Engineering Transaction of ASME, Vol. 99, pp. 115-131, 1977.

50. Takata, H., and Nagano, S., "Nonlinear Analysis of Rotating Stall," Journal of Engineering for Power Transactions of ASME, pp. 279-293, 1972.

51. Davis, R. L., Hobbs, D. E., and Weingold, H. D., “Prediction of Compressor Cascade Performance Using a Navier-Stokes Technique,” ASME Paper 88-GT-96, June 1986.

52. Chevrin, P. A., and Vuillez, C., “Viscous Flow Computations in Turbomachine Cascades,” ASME Paper 90-GT-76, June 1990.

53. Cambier, L., Escande, B., and Veuillot, J. P., “Computation of Internal Flows at High Reynolds Number by Numerical Solution of the Navier-Stokes Equations,” Rech. Aerosp., No. 1986-6, pp. 27-44, 1986.

54. Boyle, R. J., “Navier-Stokes Analysis of Turbine Blade Heat Transfer,” ASME Paper 90-GT-42, June 1990.

55. Srivastava, R., and Sankar, Lakshmi N., “Efficient Hybrid Scheme for the Analysis of Counter-Rotating Propellers,” Journal of Propulsion and Power, Vol. 9, No. 3, pp. 382-388, May-Jun 1993.

56. Dawes, W. N., “ Numerical Study of the 3D Flowfield in a Transonic Compressor Rotor with a Modeling of the Tip Clearance Flow,” AGARD Conference Proceedings, No. 401, Neuilly Sur Seine, March 1987.

57. Hah, C., and Wennerstrom, A. J., “Three-Dimensional Flowfields Inside a Transonic Compressor with Swept Blades,” Journal of Turbomachinery, Vol. 113, pp. 241-251, 1991.

58. Adamczyk, J. J., Mulac, R. A., and Celestina, M. L., “ A Model for Closing the Inviscid Form of the Average Passage Equations,” ASME Paper 86-GT-227, June 1986.

59. Hall, E. J., “Aerodynamic Modeling of Multistage Compressor Flowfields - Part 1: Analysis of Rotor/Stator/Rotor Aerodynamic Interaction,” ASME Paper 97-GT-344, 1997.

60. Hathaway, M. D., and Wood, J. R., “Application of a Multi-Block CFD Code to Investigate the Impact of Geometry Modeling on Centrifugal Compressor Flow Field Predictions, ” Journal of Turbomachinery, Vol. 119, pp. 820-830, Oct. 1997.

61. Wood, J. R., Adam, P. W., and Buggele, A. E., “NASA Low Speed Centrifugal Compressor for Fundamental Research,” NASA TM 83398, 1983.

62. Chima, R. V., and Yokota, J. W., “Numerical Analysis of Three-Dimensional Viscous Internal Flow,” AIAA Journal, Vol. 28, No. 5, pp. 798-806, May 1990.

63. Rivera, C. J., “Numerical Simulation of Dynamic Stall Phenomena in Axial Flow Compressor Blade Rows,” Ph.D. Dissertation, Georgia Institute of Technology, 1998.

64. Escuret, J. F., and Garnier, V., “Numerical Simulations of Surge and Rotating-Stall in Multi-Stage Axial-Flow Compressors,” AIAA Paper 94-3202, 1994.

65. He, L., “Computational Study of Rotating Stall Inception in Axial Compressor,” Journal of Propulsion and Power, Vol. 13, No. 1, pp. 31-38, Jan.-Feb. 1997.

66. Niazi, S., Stein, A., and Sankar, L. N., “Development and Application of a CFD Solver to the Simulation of Centrifugal Compressors,” AIAA Paper 98-0934, Jan. 1998.

67. Stein, A., Niazi, S., and Sankar, L. N., “Computational Analysis of Stall and Separation Control in Centrifugal Compressors,” Journal of Propulsion and Power, Vol. 16, No. 1, pp. 65-71, Jan. 2000,

68. Stein, A., Niazi, S. and Sankar, L. N., “Numerical Analysis of Stall and Surge in a High-Speed Centrifugal Compressor,” AIAA Paper 2000-0226, Jan. 2000.

69. Niazi, S., Stein, A., and Sankar, L. N., “ Numerical Study of Surge and Stall Alleviation in a High-Speed Transonic Fan Rotor,” AIAA Paper 2000-0225, Jan. 2000.

70. Stein, A., Computational Analysis of Stall and Separation Control in Centrifugal Compressors, Ph.D. Dissertation, Georgia Institute of Technology, Aerospace Engineering, May 2000.

71. Anderson, D. A., Tannehill, J. C., and Pletcher, R. H., Computational Fluid Mechanics and Heat Transfer, 2nd ed., McGraw-Hill, New York, 1984.

72. Hirsch, C., Numerical Computation of Internal and External Flows, Vol. I and II, 1st ed., Wiley, New York, 1988.

73. Roe, P. L., "Approximate Reimann Solvers, Parameter Vectors and Difference Schemes," Journal of Computational Physics, Vol. 135, pp. 250-258, 1981.

74. Roe, P. L. and Pike, J., "Efficient Construction and Utilization of Approximate Riemann Solutions," Computing Methods in Applied Sciences and Engineering, Vol. 6, Elsevier Science Publishers, INRIA, pp. 499-518, 1984.

75. Roe, P. L., "Discrete Models for the Numerical Analysis of Time-Dependent Multidimensional Gas Dynamics," NASA Contract Report CR-172574, Mar. 1985.

76. Roe, P. L., "Some Contributions to the Modeling of Discontinuous Flows," Lectures in Applied Mathematics, Vol. 22, pp. 163-193, 1985.

77. Roe, P. L., "Characteristic-Based Schemes for the Euler Equations," Annual Review of Fluid Mechanics, Vol. 18, pp. 337-365, 1986.

78. Roe, P. L., "Some Contributions to the Modeling of Discontinuous Flows," Large-Scale Computations in Fluid Mechanics, Edited by Engquist, B. E., Osher S. and Somerville, R. C. J., Vol. 22, Part. 2, Lectures in Applied Mathematics, ASME, Providence, RI, pp. 163-193, 1985.

79. Liu, Y. and Vinokur, M., "Upwind Algorithms for General Thermo-Chemical Nonequilibrium Flows," AIAA Paper 89-0201, Jan. 1989.

80. Pulliam, H. P. and Steger, J. L., “Implicit Finite-Difference Simulations of Three-Dimensional Compressible Flow,” AIAA Journal, Vol. 18, pp. 159-167, Feb. 1980.

81. Spalart, P. R., and Allmaras, S. R., “A One-Equation Turbulence Model for Aerodynamic Flows,” AIAA Paper 92-0439, 1992.

82. Strazisar, A. J., Wood, J. R., Hathaway, M. D., Suder, K. L., “Laser Anemometer Measurements in a Transonic Axial Flow Fan Rotor,” NASA TP-2879, Nov. 1989.

83. Moore, R. D. and Reid, L., “Performance of Single-Stage Axial-Flow Transonic Compressor with Rotor and Stator Aspect Ratios of 1.19 and 1.26 Respectively, and with Design Pressure Ratio of 2.05,” NASA Paper TM-1659, 1980.

84. Reid, L. and Moore, R. D., “Design and Overall Performance of Four Highly Loaded, High-Speed Inlet Stages for an Advanced High-Pressure-Ratio Core Compressor,” NASA Paper TM-1337, 1978.

85. Adamczyk, J. J., Celestina, M. L., and Grietzer, E. M., “The Role of Tip Clearance in High-Speed Fan Stall,” Transactions of the ASME, Vol. 115, January 1993.

86. Chima, R. V., “Calculation of Tip Clearance Effects in a Transonic Compressor Rotor,” NASA TM 107216, May 1996.

87. Pierzga, M. J. and Wood, J. R., “Investigation of the Three-Dimensional Flow Field Within a Transonic Fan Rotor: Experiment and Analysis,” Transactions of the ASME, Vol. 107, pp. 436-449, April 1985.

88. Arnone, A., “Viscous Analysis of Three-Dimensional Rotor Flow Using A Multigrid Method,” ASME 93-GT-19, Sep. 1993.

89. Chima, R. V., “Viscous Three-Dimensional Calculations of Transonic Fan Performance,” AGARD 77th Symposium on CFD Techniques for Propulsion Applications, Paper No. 21, 1991.

90. Arima, T. Sonoda, T., Shirotori, M., Tamura, A., and Kikuchi, K., “A Numerical Investigation of Transonic Axial Compressor Rotor Flow Using a Low Reynolds Number k-ε Turbulence Model,” Transactions of the ASME, Paper 97-GT-82, 1997.

91. Hah, C., and Reid, L., “A Viscous Flow Study of Shock-Boundary Layer Interaction, Radial Transport, and Wake Development in a Transonic Compressor,” Transactions of the ASME, Vol. 114, July 1992.

92. Crook, A. J., Greitzer, E. M., Tan, C. S., and Adamczyk J. J., “ Numerical Simulation of Compressor Endwall and Casing Treatment Flow Phenomena,” Journal of Turbomachinery, Vol. 115, pp. 501-511, July 1993.

93. Suder, K, L., and Celesttina, M. L., “Experimental and Computational Investigation of the Tip Clearance Flow in a Transonic Axial Compressor,” ASME Paper 94-GT-365, June 1994.

94. Shabir, A., Zhu, J., and Celestina, M., “Assessment of Three Turbulence Models in a Compressor Rotor,” ASME 96-GT-198, 1996.

95. Dalbert, P., and Wiss, D. H., “Numerical Transonic Flow Field Predictions for NASA Compressor Rotor 37,” ASME Paper 95-GT-326, June 1995.

96. Bright, B. M., Qammar, H. K., and Hartley, T. T., “Dimension Determination of Precursive Stall Events in a Single Stage High Speed Compressor,” NASA TM 107268, 1996.

97. Eveker, K. M., and Nett, C. N., “Model Development of Active Surge Control Rotating Stall Avoidance in Aircraft Gas Turbine Engines,” Proceedings of the American Control Conference, pp. 3166-3172, 1991.

98. Wang, Y. and Murray, R. M., “Effects of the Shapes of Compressor Characteristics on Actuator Requirements for Rotating Stall Control,” Proceedings of the 1998 American Control Conference, 1998.

99. Prasad, J. V., Neumeier, Y., and Krichene, A., “Active Control of Compressor Surge Using a Real Time Observer,” Proceedings of the NATO Applied Vehicle Technology Conference, Braunschweig, May 2000.

VITA

Saeid Niazi was born in Sepidan, Iran on May 17, 1961. He graduated from the Shiraz University, Iran, with a Bachelor of Science (B.Sc.) degree in Mechanical Engineering in September 1986. In August 1991, he graduated form the Shiraz University in Iran with a Master of Science (M.Sc.) degree in Fluid Mechanic and Heat Transfer Engineering. From September 1989 to August 1995, he taught at the Hormozgan University in the city of Bandar Abbas, Persian Gulf, Iran. He was the Dean of the central library of the Hormozgan University during the period 1992-1995. He commenced his graduate work at Georgia Institute of Technology in September 1996. He earned the degree of Doctor of Philosophy (Ph.D.) in Aerospace Engineering in July 2000. He is a member of the American Institute of Aeronautics and Astronautics.